Numerical Modelling of Directional Solidification in Metal Alloys

---

A thesis submitted to the
Department of Mechanical & Manufacturing Engineering
Trinity College Dublin, the University of Dublin
in partial fulfilment of the requirements for the degree of

Doctor of Philosophy

by

Sara Battaglioli

Supervisors:
Dr. Shaun McFadden
Dr. Anthony J. Robinson

August, 2018

Declaration of Authorship

I, Sara Battaglioli, declare that this thesis titled "Numerical Modelling of Directional Solidification in Metal Alloys" has not been submitted as an exercise for a degree at this or any other university and it is entirely my own work.

I agree to deposit this thesis in the University's open access institutional repository or allow the library to do so on my behalf, subject to Irish Copyright Legislation and Trinity College Library conditions of use and acknowledgement.

Signed:

_____

To Giovanni

Abstract

Manufacturing routes for metal alloy components often involve solidification processes. In order to obtain a product that meets given requirements in terms of mechanical properties, the ability to predict the grain structure development during solidification is crucial. In particular, grains with two different morphologies can form, i.e. columnar or equiaxed grains. When both types of grain structures develop during the process, the final product exhibits a columnar to equiaxed transition (CET), which is usually to be avoided since it introduces abrupt changes in the mechanical properties. In order to investigate the influence of process parameters on grain structure evolution, directional solidification processes such as Bridgman and power-down solidification are widely used in research, since they allow to control nominal temperature gradients and cooling rates in the solidifying samples. The overarching objective of this thesis is to provide a methodology for the numerical investigation of directional solidification in metal alloys. In particular, this study is carried on in the framework of ESA's GRADECET (Gravity Dependence of CET in Peritectic TiAl Alloys) project, with the aim to investigate the influence of process parameters and gravity conditions (micro, terrestrial, hyper-gravity) on grain structure evolution and CET. In order to achieve this goal, three ever more advanced models are presented. Firstly, a 2D axisymmetric enthalpy method is developed. This model allows to predict the transient evolution of temperature and solid fraction during Bridgman solidification in absence of convection. Secondly, the model is improved by the inclusion of a front tracking algorithm. Such improvement allows to model the growth of the columnar grain region by the means of a series of markers connected by linear segments, representing the envelope of the columnar grain tips. Furthermore, the front tracking model does not assume equilibrium solidification, therefore it allows to identify a region of undercooled liquid ahead of the front. This is a fully liquid region below the alloy's liquidus temperature, where equiaxed grains might nucleate and grow. Hence, these features allow to predict the development of columnar grains with different orientation (axial columnar and radial columnar). Furthermore, the analysis of the thermal conditions in the undercooled liquid region during the solidification process enables to evaluate the likelihood of CET occurrence. Finally, the front tracking model is further expanded by including the treatment of thermal convection arising under terrestrial and hypergravity conditions. Throughout the thesis, the three models are used for simulating different experimental scenarios, and to perform several parametric studies. These simulations corroborate the ability of the models in reproducing realistic results. Furthermore, they enable to gain information on hard to observe phenomena, such as transient evolution of temperature and fluid flow in the bulk of the samples, or transient growth of different grain morphologies, providing a significant contribution to the analysis and understanding of the directional solidification process.

Publications and Conferences

Journal publications

- S. Battaglioli, S. McFadden, A.J. Robinson, *Numerical Simulation of Bridgman Solidification of Binary Alloys*, International Journal of Heat and Mass Transfer, Vol. 104, pp 199-211, 2017.
- M. Seredyński, S. Battaglioli, R.P. Mooney, A.J. Robinson, J. Banaszek, S. McFadden, *Code-to-code Verification of an Axisymmetric Model of the Bridgman Solidification Process for Alloys*, International Journal of Numerical Methods for Heat and Fluid Flow, Vol. 27, Issue 5, 2017.
- S. Battaglioli, A.J. Robinson, S. McFadden, *Axisymmetric Front Tracking Model for the Investigation of Grain Stucture Evolution during Transient Directional Solidification in a Bridgman Furnace*, International Journal of Heat and Mass Transfer, Vol. 115, pp 592-605, 2017.
- S. Battaglioli, S. McFadden, A.J. Robinson, *Influence of Natural and Forced Gravity Conditions during Directional Columnar Solidification*, International Journal of Heat and Mass Transfer, Vol. 126, pp 66-80, 2018.

Conference papers

- S. Battaglioli, R.P. Mooney, M. Seredyński, A.J. Robinson, S. McFadden, *Computer Modelling of Manufacturing Processes: The Development of a 2D Axisymmetric Model of the Bridgman Casting Process*, 32nd International Manufacturing Conference (IMC32), Queens University Belfast, Belfast, UK, 2015.
- M. Seredyński, S. Battaglioli, R.P. Mooney, A.J. Robinson, J. Banaszek, S. McFadden, *Verification of a 2D Axisymmetric Model of the Bridgman Solidification Process for Metallic Alloys*, Numerical Heat Transfer 2015, Eurotherm Seminar No 109, Gliwice-Warsaw, Poland, Conference Proceedings pp 295–303, 2015.

- S. Battaglioli, A.J. Robinson, S. McFadden, *2D Axisymmetric Front Tracking Model for Bridgman Solidification of γ-TiAl Alloys*, 6th Decennial International Conference on Solidification Processing (SP17), Old Windsor, UK, Conference Proceedings pp 368-371, 2017.
- S. Battaglioli, A.J. Robinson, S. McFadden, *Numerical Investigation of Directional Solidification of TiAl Alloys under Hypergravity Conditions*, 35th International Manufacturing Conference (IMC35), Dublin Institute of Technology, Dublin, Ireland, 2018.

Posters and other presentations

- S. Battaglioli, R.P. Mooney, A.J. Robinson, S. McFadden, *Macroscale Modelling of Bridgman Furnace Solidification for the Prediction of Texture Evolution and Columnar to Equiaxed Transition*, poster presented at the 8th International Conference on Multiscale Materials Modelling (MMM2016), Dijon, France, 2016.
- S. Battaglioli, A.J. Robinson, S. McFadden, *Axisymmetric Front Tracking Model for the Investigation of Grain Structure Evolution durinf Directional Solidification of γ-TiAl Alloys*, poster presented at the 20th Sir Bernard Crossland Symposium, Dublin Institute of Technology, Dublin, Ireland, 2017.
- S. Battaglioli, R.P. Mooney, A.J. Robinson, S. McFadden, *Transient Computational Model for the Prediction of Grain Structure Evolution during Bridgman Solidification of γ-TiAl Alloys*, presented at the TMS 2018 147th Annual Meeting and Exhibition, Phoenix, Arizona, 2018.

Acknowledgements

I would like to express my sincere gratitude to my supervisors, Dr. Shaun McFadden and Dr. Anthony Robinson, for their precious guidance and support throughout this work. I would also like to thank Dr. Robin Mooney for sharing his knowledge with me and offering valuable technical discussions during these years.

My gratitude goes to all my colleagues in the Department of Mechanical and Manufacturing Engineering, and to all the academic and technical staff in the Parsons Building.

Particular thanks go to Eleonora and Alessia for their true friendship.

Thank you to my family for their invaluable support and encouragement during these years.

Finally, my deepest gratitude goes to Giovanni, who has always been by my side with his constant love and support, sustaining me through this challenging experience.

This work was carried out as part of the GRADECET (Gravity Dependence of Columnar to Equiaxed Transition in Ti-Al alloys) research project, with the financial support of the European Space Agency PRODEX Programme (contract C4000110385) under the management of the Irish delegation to ESA within Enterprise Ireland.

Contents

Declaration of Authorship **iii**

Abstract **vii**

Publications and Conferences **ix**

Acknowledgements **xi**

1 Introduction **1**
1.1 Context for this research 1
1.2 The GRADECET project 3
1.2.1 Why considering different gravity conditions? 4
1.2.2 Directional solidification experiments 5
1.2.3 Role of this thesis within GRADECET 7
1.3 Thesis objectives and contribution 8
1.4 Numerical modelling of alloys solidification 9
1.4.1 Front tracking method studies 11
1.4.2 General methodology adopted in the thesis 13
1.5 Thesis structure 15

2 Numerical Simulation of Bridgman Solidification of Binary Alloys **21**
2.1 Introduction 21
2.2 Methodology 25
2.2.1 Model 25
2.2.2 Non-dimensional formulation 29
2.2.3 Numerical model 30
2.2.4 Conditions for comparison with experimental data 32
2.2.5 Conditions for the parametric study 33
2.3 Results and discussion 35
2.3.1 Comparison with experimental data 36
2.3.2 Influence of varying Pe and Bi on Bridgman solidification 38
2.4 Conclusions 47
2.5 Addendum 48
2.5.1 Code-to-code verification 48

3 Axisymmetric Front Tracking Model for the Investigation of Grain Structure Evolution During Directional Solidification 57
3.1 Introduction . . . 58
3.2 Methodology . . . 61
3.2.1 Thermal model . . . 61
3.2.2 Solidification model . . . 64
3.2.3 CET prediction . . . 66
3.2.4 Boundary conditions . . . 67
3.2.5 Input data . . . 69
3.2.6 Simulation setups . . . 70
Stationary solidification . . . 70
Combined Bridgman and power-down simulation . . . 71
3.3 Results and discussion . . . 72
3.3.1 Stationary solidification . . . 72
3.3.2 Bridgman and power down solidification . . . 73
CET prediction . . . 79
Comparison with experiments . . . 86
3.4 Conclusions . . . 88
3.5 Addendum . . . 88
3.5.1 Indirect evaluation of CET position . . . 88

4 Influence of Natural and Forced Gravity Conditions during Directional Columnar Solidification 97
4.1 Introduction . . . 98
4.2 General methodology . . . 101
4.2.1 Governing equations . . . 101
4.2.2 Solidification model . . . 103
4.2.3 Solution algorithm . . . 104
4.3 Solidification in microgravity . . . 107
4.3.1 Results and discussion . . . 109
4.4 Solidification under terrestrial gravity conditions . . . 112
4.4.1 Results and discussion . . . 112
4.5 Solidification on centrifuge . . . 116
4.5.1 Non-dimensional analysis . . . 118
4.5.2 Results and discussion . . . 120
4.6 Conclusions . . . 125
4.7 Addendum . . . 126
4.7.1 Effect of sample misalignment during centrifugal casting . . . 126

5 Conclusions 135

A FORTRAN Solver Description **139**

List of Figures

1.1 Titanium aluminides properties and applications. 1
1.2 Different types of grain structures. 2
1.3 The GRADECET project. 3
1.4 Schematic of a centrifugal casting process. 5
1.5 Bridgman and power down directional solidification processes for the study of CET. 6
1.6 Outcomes of different GRADECET experiments. 7
1.7 Models and case studies addressed the thesis. 9
1.8 Different models for alloys solidification in relation to phenomena length-scale and computational cost. 10
1.9 Enthalpy method versus front tracking method control volume types and calculation of solid fraction. 14

2.1 Schematic of a Bridgman furnace. 23
2.2 Computational domain for simulations. 27
2.3 Domain discretization. 31
2.4 Measured and computed cooling curves at steady state, normalised to the time where the temperature equals the solidus temperature of the alloy in thermal equilibrium (627.5°C). 36
2.5 Axial temperature gradient taken from the temperature difference measured by two thermocouples and temperature gradient from simulations; time is normalised to the beginning of the pulling stage. 37
2.6 Simulation S0: temperature distribution on the axis of the sample, obtained with and without advection. 39
2.7 Simulation S0: solid fraction and temperature distribution in an axial section of the sample. Resting stage $Pe = 0$ (left), and pulling stage $Pe > 0$ (right).The white highlights the position of the liquidus isotherm, which represents the envelope of the mushy zone on the liquid side. 40
2.8 Curvature of the liquidus isotherm ($T = 618$°C) at steady state in the pulling stages; note that both axes are dimensionless. 41
2.9 Simulations S1 (left) and S2 (right) showing solid fraction (top) and temperature distribution (bottom) in an axial section of the samples during the pulling stage ($Pe > 0$). 42

2.10 Simulations S3 (left) and S4 (right) showing solid fraction (top) and temperature distribution (bottom) in an axial section of the samples during the pulling stage ($Pe > 0$). 43
2.11 Simulations S3 (left) and S4 (right) showing the advective sensible heat term $-Pe\partial T^*/\partial x^*$ (top), the advective latent heat term $Pe/Ste \cdot \partial g_s/\partial x^*$ (middle), and the comparison of the two terms at $r = 0$; note that these terms are dimensionless. 45
2.12 Simulations S5 (left) and S6 (right) showing the solid fraction, temperature distribution, and radial temperature gradient in an axial section of the samples during the pulling stage ($Pe > 0$). 46
2.13 Temperature histories at several axial location in response to the velocity jump regime (left) and the velocity ramp regime (right). Axial location shown are: x=63 mm (top), 67 mm, 71 mm, 75 mm, 79 mm, 83 mm, and 87 mm (bottom). 51

3.1 Computational domain for simulations in grey. a) Beginning of pulling stage. b) End of pulling stage. 62
3.2 Discretization grid of computational domain. 63
3.3 Front tracking model. 64
3.4 Solid fraction to temperature relationship for Ti-44.5Al-4.5Nb-0.2C-0.2B estimated using Thermocalc via the "Modified Scheil Module" [15]. 66
3.5 Thermal contact resistance between sample and crucible 68
3.6 Comparison of experimental and simulated temperature profiles at the sample axial position. 72
3.7 Temperature (top half of images) and solid fraction (bottom half of images) distributions at the beginning (a) and at the end (b) of the pulling stage. . . 74
3.8 PD1: temperature, solid fraction and front evolution during the power down solidification process. t_{PD} is the time since the beginning of the cooling stage. (a) t_{PD}=200 s. (b) Radial heat flux reversal time. (c) 100 s after radial heat flux reversal. (d) 150 s after radial heat flux reversal. 76
3.9 PD2: temperature, solid fraction and front evolution during the power down solidification process. t_{PD} is the time since the beginning of the cooling stage. (a) t_{PD}=200 s. (b) Radial heat flux reversal time. (c) 100 s after radial heat flux reversal. (d) 150 s after radial heat flux reversal. 76
3.10 PD3: temperature, solid fraction and front evolution during the power down solidification process. t_{PD} is the time since the beginning of the cooling stage. (a) t_{PD}=200 s. (b) Radial heat flux reversal time. (c) 100 s after radial heat flux reversal. (d) 150 s after radial heat flux reversal. 77
3.11 PD4: temperature, solid fraction and front evolution during the power down solidification process. t_{PD} is the time since the beginning of the cooling stage. (a) t_{PD}=200 s. (b) Radial heat flux reversal time. (c) 100 s after radial heat flux reversal. (d) Time at which all the liquid is enveloped by columnar mush. 77

3.12 Marker trajectories during the power down solidification process. 79
3.13 Equiaxed index for PD1, PD2, PD3 and PD4. 80
3.14 Level of undercooling at the time corresponding to the maximum of I_{eq}. . . . 82
3.15 Hunt plot showing the advancement velocity of the axial marker versus the axial temperature gradient at its location. 83
3.16 Hunt plot showing the advancement velocity of the radial marker at x=120 mm versus the radial temperature gradient at its location. 85
3.17 Images of samples showing different grain regions: U = unmelted, C = axial columnar, R = radial columnar, E = equiaxed [16]. 87
3.18 Qualitative evaluation of CET position for different values of nucleation undercooling ΔT_{nucl} 90
3.19 Qualitative evaluation of CET position for different values of nuclei density N_0 91

4.1 Solid fraction to temperature relationship for Ti-48Al-2Cr-2Nb estimated using Thermocalc via the "Modified Scheil Module". 103
4.2 Flowchart of general solution algorithm. 104
4.3 Staggered grid. 105
4.4 Solution for front tracking marker velocity oscillations arising from the use of large time steps in the presence of high temperature gradients. 107
4.5 Computational domain. 107
4.6 Temperature at the circumference of the sample (r=r_{samp}) at different times during the solidification process: comparison of experimental and simulated results. 110
4.7 Columnar front position and temperature distribution in the sample at different times during the solidification process. Isotherms are drawn at intervals of 2°C. 111
4.8 Streamlines in the sample at different times during the solidification process. Green streamlines correspond to counter-clockwise rotating flow, while blue stramlines correspond to clockwise rotating flow. Streamlines are drawn at intervals of 0.15 mm^2/s. 115
4.9 Maximum and mean value of the Peclét number registered in the sample during the solidification process. 116
4.10 Schematic of the directional solidification process on a centrifuge and 2D planar computational domain used in the simulations. 117
4.11 Columnar front position, temperature distribution, and streamlines in the sample at different times during the solidification process. Isotherms are drawn at intervals of 2°C, while streamlines are drawn at intervals of 0.15 mm^2/s. . . . 121
4.12 Effect of gravity level changes on the flow. Green streamlines correspond to counter-clockwise rotating flow, while blue stramlines correspond to clockwise rotating flow. Streamlines are drawn at intervals of 0.2 mm^2/s. 122

4.13 Effect of R_C changes on the flow. Green streamlines correspond to counter-clockwise rotating flow, while blue stramlines correspond to clockwise rotating flow. Streamlines are drawn at intervals of 0.2 mm^2/s. 124
4.14 Horizontal sections of Ti-46Al-8Nb samples obtained by directional solidification on ESA's Large Diameter Centrifuge during GRADECET LDC campaign I. 127
4.15 Experimental setup used during GRADECET LDC campaign I, showing the furnace misalignment with respect to the centrifuge arm. 128
4.16 Simulation results for a sample positioned with 115 mm misalignment with respect to the centrifuge arm. 129

A.1 Flowchart of general solution algorithm. 139
A.2 Some examples of possible configurations of the captured volumes. 141
A.3 Flowchart of SIMPLER algorithm for the calculation of pressure and velocity. 143
A.4 Flowchart of internal loop for the calculation of temperature and solid fraction. 144

List of Tables

1.1 General mixture conservation equations. 13

2.1 Setup for comparison with experimental data from Zimmermann et al. [18]. . 33
2.2 Dimensional input values for parametric simulations. 34
2.3 Dimensionless input values for parametric simulations. 34
2.4 Thermophysical properties of Al-1.3wt%Cu and Al-7wt%Si used in simulations. 35
2.5 Input values for code-to-code verification. 49
2.6 Pulling velocity input data. 50

3.1 Thermophysical properties of Ti-45.5Al-4.7Nb-0.2C-0.2B and Y_2O_3 used in the simulations. 69
3.2 Geometrical data used in the simulations. 70
3.3 Input data for stationary simulations. 71
3.4 Input data for combined Brigman and power down simulations. 71
3.5 Time and axial marker position corresponding to the radial heat flux reversal and to the transition to a fully radial columnar growth. 78
3.6 Time and axial marker position corresponding to the maximum of I_{eq}. 81
3.7 Time and position of the axial marker corresponding to CET as predicted by Hunt model for different nuclei densities and equiaxed nucleation undercooling values. 84
3.8 Time corresponding to CET in the radial columnar zone (x=120 mm) as predicted by Hunt model for different nuclei densities and equiaxed nucleation undercooling values. 86

4.1 Geometrical data used in the simulations. 108
4.2 Input data for the heaters during different stages of the process. 108
4.3 Thermophysical properties of Ti-48Al-2Cr-2Nb used in the simulations. . . . 109
4.4 Input values of the angular velocity and centrifuge arm used in the parametric analysis. The bottom line shows the corresponding magnitude of centrifugal acceleration with respect to terrestrial gravity: $N_g \approx \omega^2 R_c/g$. 117
4.5 Simulation results compared to predictions from the non-dimensional analysis. 123

Nomenclature

A	area, [m^2]
b	undercooling exponent, [-]
C	dendrite growth coefficient, [$°C^{-b}$ m/s)]
c_p	specific heat capacity, [J/(°C kg)]
g	Earth's gravitational acceleration, [m/s^2]
G	temperature gradient, [°C/m]
g_E	solid fraction at eutectic temperature, [-]
g_s	solid fraction of the mush, [-]
G_s	total solid fraction in a CV, [-]
h	heat transfer coefficient, [W/(°C m^2)]
H	enthalpy, [J]
I_{eq}	equiaxed index, [°C m^3]
k	thermal conductivity, [W/(°C m)]
k_{part}	partition coefficient, [-]
l	general length, [m]
L	latent heat of fusion, [J/kg]
N_0	nucleation seeds density, [m^{-3}]
N_g	gravity level, [-]
P	general thermophysical property
q	heat flux, [W/m^2]
r	radial coordinate, [m]
R_C	centrifuge arm, [m]
R_{int}	thermal contact resistance, [°C m^2/W]
t	time, [s]
T	temperature, [°C]
T_E	eutectic temperature, [°C]
T_L	liquidus temperature, [°C]
T_M	melting temperature, [°C]
T_S	solidus temperature, [°C]
u	velocity, [m/s]
V	volume, [m^3]
v_t	dendrite tip growth rate, [m/s]
x	axial coordinate, [m]
α	thermal diffusivity, [m^2/s]
β	thermal expansion coefficient, [$°C^{-1}$]
μ	dynamic viscosity, [Pa s]
ν	kinematic viscosity, [m^2/s]
ρ	density, [kg/m^3]
ϕ	general variable
ω	centrifuge angular velocity, [rad/s]

Subscripts

cr	crucible
CV	control volume
dom	domain
l	liquid
m	mush
nb	neighbouring CVs
$nucl$	nucleation
ref	reference value
s	solid
$samp$	sample

Dimensionless numbers

$Bi = {hl_{ref}}/{k}$	Biot number
$Gr = {\omega^2 R_C \beta \Delta T_{ref} l_{ref}^3}/{\nu^2}$	Grashof number
$Pe = {ul_{ref}}/{\alpha}$	Péclet number
$Re = {u_{ref} l_{ref}}/{\nu}$	Reynolds number
$Ro = {u_{ref}}/{(2\omega l_{ref})}$	Rossby number
$Ste = {c_p \Delta T_{ref}}/{L}$	Stefan number
$Ta = {4\omega^2 l_{ref}^4}/{\nu^2}$	Taylor number

Acronyms

CET	columnar to equiaxed transition
FTM	front tracking model
LCD	large diameter centrifuge

Chapter 1

Introduction

1.1 Context for this research

In the past 20 years, much attention has been paid to the study of γ titanium aluminides, due to the ever-increasing requirement for high performance materials to be used in advanced engineering applications. Excellent properties such as low density, high specific strength, and good oxidation and creep resistance at high temperatures make γ TiAl alloys the perfect candidate for the production of light-weight components such as low pressure turbine blades for aero engines or turbocharger wheels and exhaust valves [1–3] (figure 1.1). In particular, when compared with nickel-based superalloys, titanium aluminides display comparable values of specific strength, but about half of the density. Therefore, the substitution of nickel superalloy components with γ-TiAl ones would allow considerable weight reduction of gas turbine engines and consequentially significantly lower fuel consumption and CO2 emissions [4].

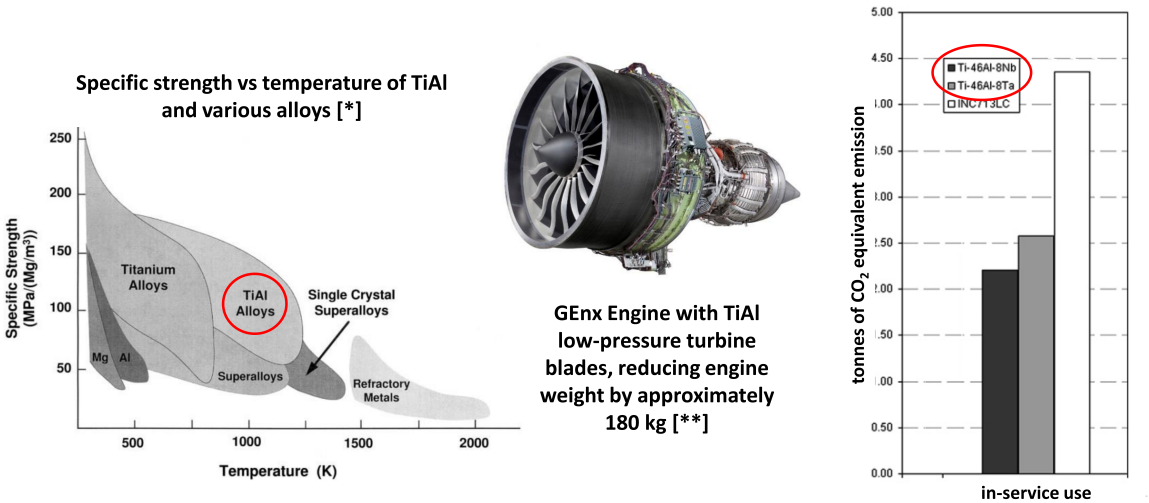

[*] D. M. Dimiduk, *Materials Science and Engineering: A,* vol. 263, no. 2, pp. 281–288, 1999.
[**] www.geaviation.com/commercial/engines/genx-engine
[***] N. Lavery et al., *Intermetallics,* vol. 19, no. 6, pp. 787-792, 2011.

FIGURE 1.1: Titanium aluminides properties and applications.

Because of titanium aluminides low room temperature ductility and fracture toughness,

which limit their machinability at room temperature [5,6], investment casting is acknowledged as a potentially feasible and cost effective processing route for manufacturing near-net shape γ-TiAl components [7–9]. Nevertheless, the efficacy of this method of production strictly depends on the ability to control the quality of the final product in terms of grain structure, porosity level, homogeneity of composition (macrosegregation) *etc.*...

In general, alloys solidify with dendritic structures (*i.e.*, treelike structures, from the Greek $\delta\acute{\epsilon}\nu\delta\rho o\nu$, déndron, "tree"). Depending on the thermal conditions in the casting, the dendrites can either nucleate at the mould wall and grow directionally under an imposed thermal gradient, or can nucleate and grow radially at multiple locations in an undercooled melt (alloy in molten phase below its equilibrium liquidus temperature T_L). Therefore, two different grain morphologies can develop, *i.e.*, columnar grains or equiaxed grains (figure 1.2). Depending on the required mechanical properties for the product, either one or the other structure is desired. For example, fine equiaxed grains provide uniform and isotropic properties, while aligned columnar grains can improve strength and creep resistance in a given direction. On the other hand, in some cases mixed structures could develop in a casting, such as in the case of columnar to equiaxed transition (CET). In particular, CET occurs when equiaxed grains nucleate and grow ahead of an advancing columnar growth front. This topic is of critical concern for the production of structural components, since this transition introduces abrupt, undesired variation of the mechanical properties.

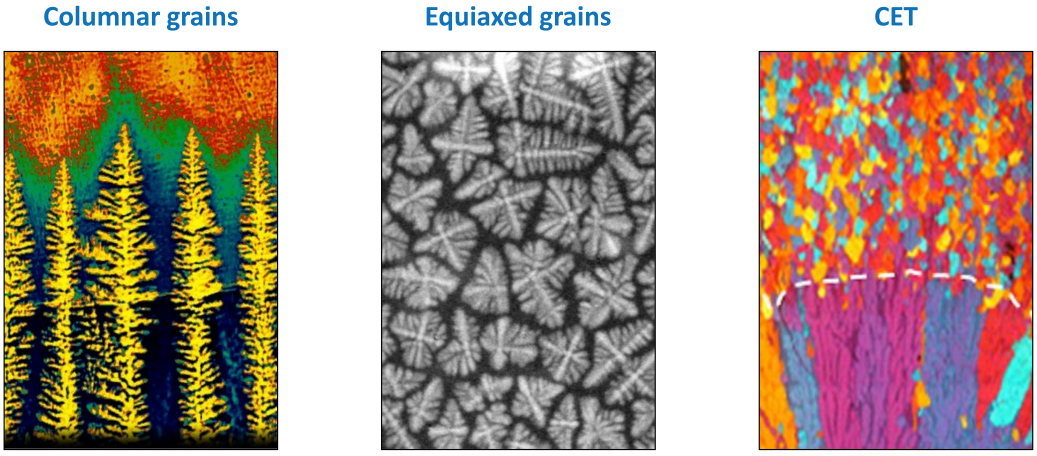

FIGURE 1.2: Different types of grain structures.

Therefore, a deep understanding of the influence of process parameters on the solidification process is crucial in order to ensure the achievement of targeted mechanical properties.

With this in mind, two pan-European research projects, led by ESA, have been established: IMPRESS (Intermetallic Materials Processing in Relation to Earth and Space Solidification) [10, 11], and GRADECET (Gravity Dependence of CET in Peritectic TiAl Alloys).

Whithin the first project, started in 2004 and concluded in 2009, an extensive campaign of research activities, involving ternary Ti-Al-Nb alloys, was carried out. These included several solidification experiments and modelling activities, both in terrestrial and microgravity conditions, which allowed the elaboration of reliable thermodynamic and kinetic databases, precise thermophysical properties measurement, and material structure characterization [12–14]. In addition, experimental and numerical studies were performed with the aim of investigating different casting processes for the manufacturing of TiAl components, such as centrifugal, tilt, and counter gravity casting [15–17]. The second project, started in 2010, aims to develop and integrate the research initiated within IMPRESS, by investigating additional solidification scenarios under terrestrial, micro, and hyper-gravity conditions.

1.2 The GRADECET project

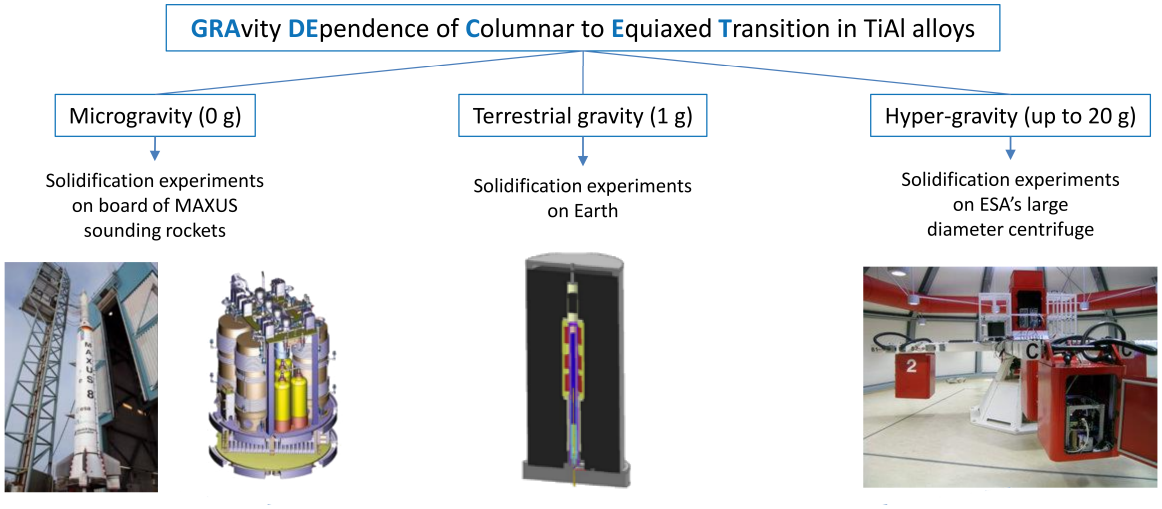

FIGURE 1.3: The GRADECET project.

The present work is carried out within the framework of ESA's GRADECET project (figure 1.3). Specifically, this project aims to investigate gravity dependence of microstructure formation and segregation in peritectic TiAl-based alloys, with special attention to mechanisms responsible for columnar to equiaxed transition (CET). The occurrence of CET depends on the combination of several factors, such as thermodynamic and thermophysical properties of the alloy, solidification parameters, temperature conditions and flow patterns in the melt. Understanding the effect of each of these mechanisms is therefore indispensable, and requires the employment of carefully designed experiments and numerical models. In order to accomplish this overarching objective, several tasks were identified and carried out by different partners of the GRADECET project:

- to perform directional solidification experiments on ground under terrestrial gravity conditions;
- to perform directional solidification experiments under microgravity conditions on board of MAXUS sounding rockets;
- to perform directional solidification experiments under hypergravity conditions on ESA's large diameter centrifuge LDC (Noordwijk, NL)[1];
- to perform 2D/3D multi-scale modelling of solidification scenarios under different gravity conditions.

1.2.1 Why considering different gravity conditions?

The conduction of solidification experiments under different gravity conditions is due to several reasons.

Firstly, the importance of considering terrestrial gravity conditions appears obvious, since they are the ones found during any solidification process taking place on Earth. In general, during a solidification process, density inhomogeneities arise because of thermal expansion and composition variation in the material, hence in the presence of gravity natural convection in the melt occurs. In turn, convective motion can affect the quality of the final product, inducing phenomena such as macrosegregation, grains buoyancy or sedimentation, or dendrites fragmentation. From an experimental point of view, tests under terrestrial gravity conditions can be conveniently repeated, and experimental setup can be easily adjusted. In the framework of GRADECET, this would allow for example to identify the range of process parameters leading to CET, and to establish guidelines for the setup of experiments to be performed in microgravity and hypergravity conditions.

Secondly, microgravity experiments are relevant because they offer an opportunity to eliminate natural convection during the solidification process. In fact, in a microgravity environment, transport phenomena are essentially diffusive and buoyancy forces are suppressed. Therefore, by comparing identical experiments on ground and in space it is possible to discern the effect of process parameters, such as imposed temperatures and cooling rates, from the effect of gravity and phenomena such as thermal and solutal convection.

Thirdly, hypergravity experiments in the LDC, besides contributing to a better understanding of gravity dependence of CET, are particularly relevant in consideration of the importance of the centrifugal casting process, sketched in figure 1.4, as a manufacturing route for titanium aluminide near-net shape components. In fact, centrifugal casting is particularly fitting when dealing with lightweight and highly reactive materials such as TiAl. Usually, in

[1] https://www.esa.int/Education/Spin_Your_Thesis/The_Large_Diameter_Centrifuge2

a normal gravity casting system, the feeding of the mould relies on the weight of the molten metal, however for low-density materials an assistant force, such as the centrifugal one, may be needed to avoid shrinkage defects. In addition, highly reactive alloys react with refractory materials in the melting crucible, suffering from contamination during melting. This can be prevented by employing specific processes, such as induction skull melting, where the alloy is melted in a water-cooled copper crucible. However, this process implies melting at a low superheat, that can be easily lost during pouring. Therefore, the centrifugal force can be exploited in order to fill the moulds as quickly as possible and avoid defects such as incomplete filling or gaps.

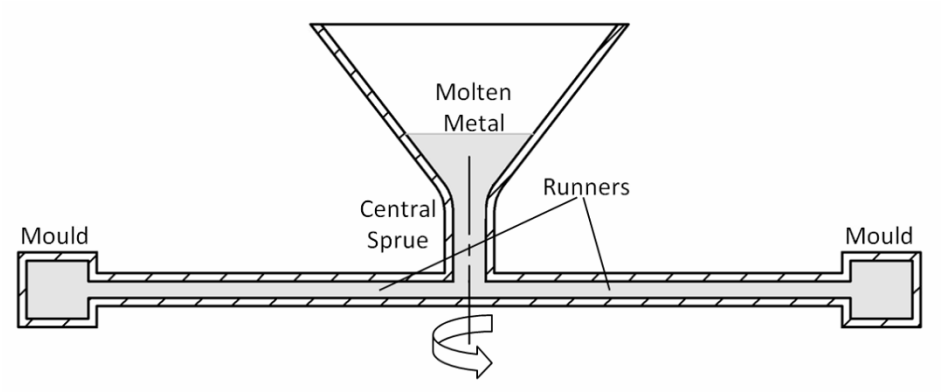

FIGURE 1.4: Schematic of a centrifugal casting process.

1.2.2 Directional solidification experiments

In research, a way to investigate columnar grain growth and CET is to perform transient directional solidification experiments such as the ones shown in figure 1.5. Cylindrical samples are held in a furnace where a series of heaters at different temperatures is used to impose a chosen temperature gradient. Initially, a steady state condition is considered, where the columnar front in the sample is at equilibrium at the liquidus temperature. At this point, CET can be triggered operating the furnace in two possible modes, *i.e.*, either in Bridgman mode or in power down mode.

In Bridgman mode, the sample is pulled towards the coldest region of the furnace, which results in applying a cooling rate. During the pulling stage, columnar growth in general does not occur at equilibrium, instead a region of undercooled liquid develops ahead of it. In this region, depending on the thermal conditions, equiaxed grains can nucleate and grow, eventually leading to CET.

The power down process is analogous to the Bridgman one, however in this case the sample is held stationary, and the cooling rate is achieved by lowering the temperature of the heaters. Again, columnar growth does not keep pace with the applied cooling rate, leading

to the formation of an undercooled liquid region and the potential for CET occurrence.

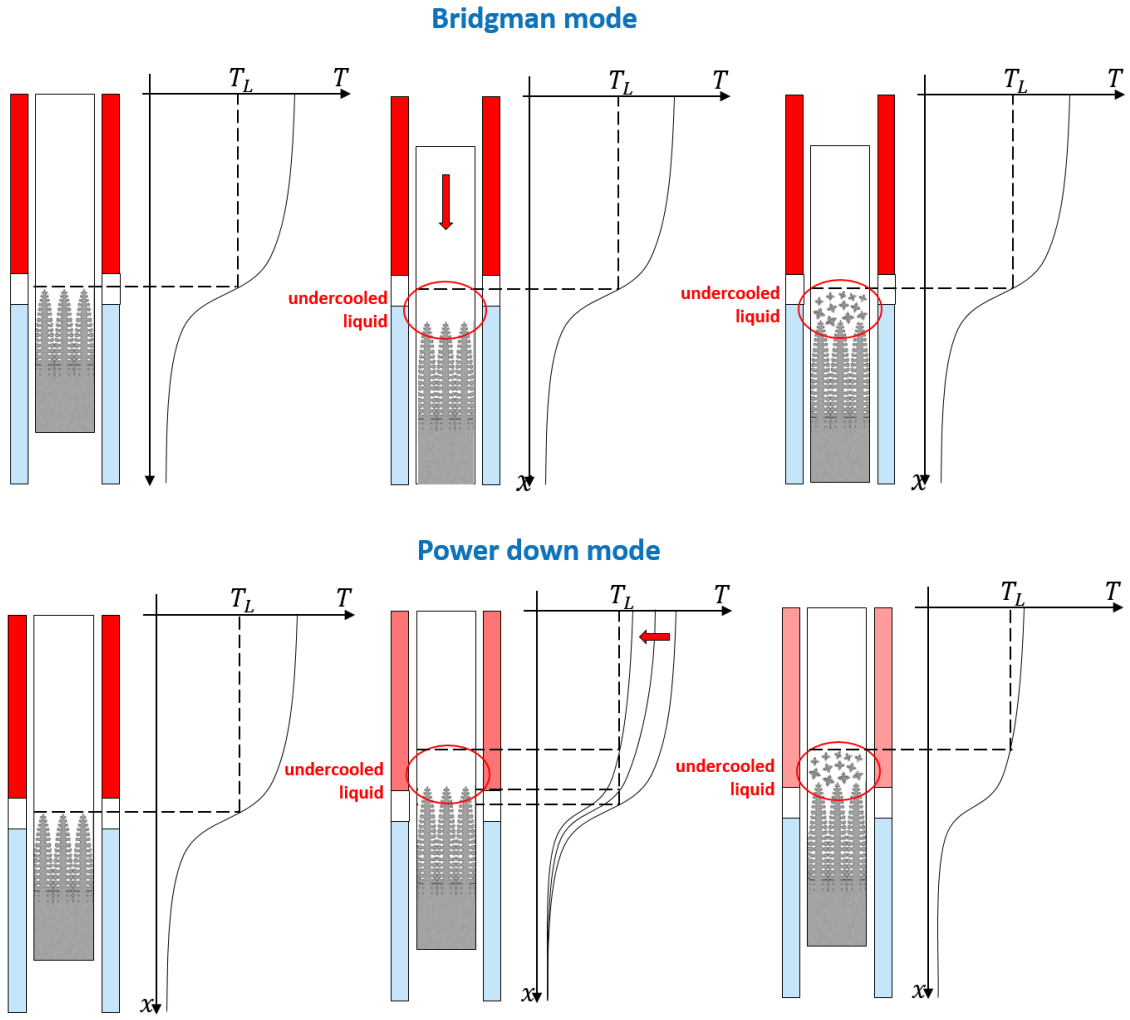

FIGURE 1.5: Bridgman and power down directional solidification processes for the study of CET.

Within the framework of GRADECET, experiments which combined Bridgman and power down solidification were performed with the aim to obtain samples showing clear CET. Nonetheless, as figure 1.6 shows, during some of the experiments different, unexpected results were obtained, such as the growth of radial columnar grain regions during power down solidification, or skew columnar grains and CET during experiments in the LDC. Therefore, the observation of these results has raised the following research questions:

- which conditions lead to the development of CET during directional solidification?
- How do process parameters such as applied pulling or cooling rates influence the development of radial columnar growth?
- How does natural/forced convection influence the solidification process?

In order to answer these questions, both experimental and numerical investigations are required to understand the transient phenomena that take place during the solidification process.

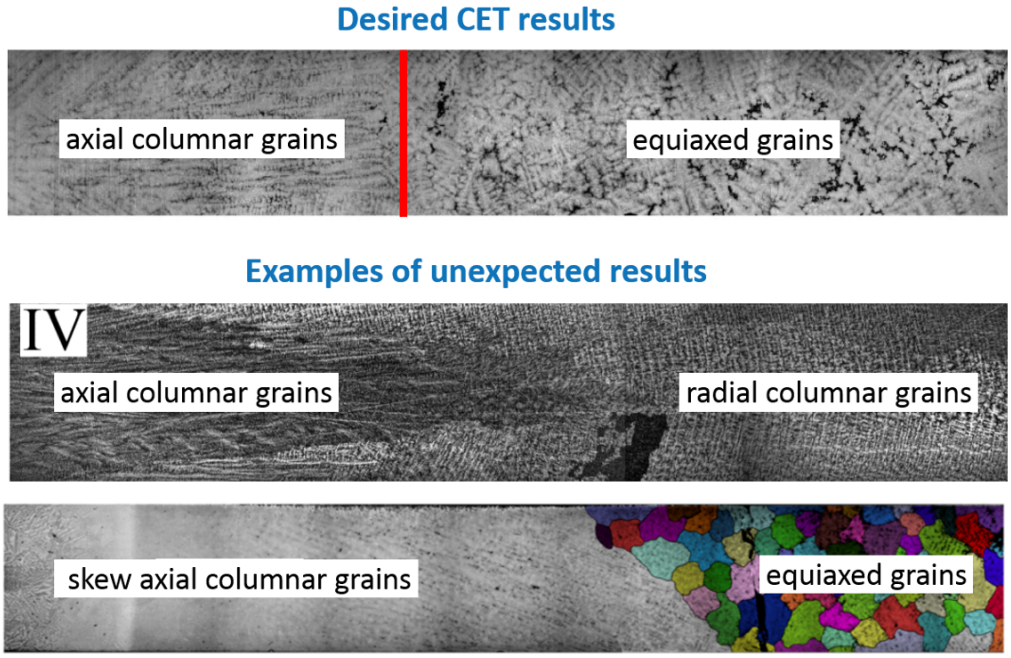

FIGURE 1.6: Outcomes of different GRADECET experiments.

1.2.3 Role of this thesis within GRADECET

Numerical simulations play a crucial role both in the preparation of the experiments and in the analysis of the experimental results. In order to cover different aspects of the solidification process, two sub-tasks were established within GRADECET, *i.e.* the development of numerical models for the investigation of grain growth at the scale of several dendrites (microscale), and the development of meso-macroscopic models for the investigation of temperature, fluid flow patterns, and CET at the scale of the samples (mm to m).

Within this context, the main task of the author was to provide for the development of a methodology for the numerical investigation of directional solidification at the scale of the sample. In particular, a novel numerical model for directional solidification, incorporating heat transfer, fluid flow, and grain growth, should be implemented and applied to reproduce different GRADECET experimental scenarios. The chosen methodology should be able to give enlightenment and deeper understanding of the solidification process under different gravity conditions, with particular focus on the questions raised by the experimental results discussed in the previous paragraph.

1.3 Thesis objectives and contribution

As mentioned in the previous section, the overarching objective of this work is to develop a computational model of directional solidification of γ titanium aluminide samples under micro, terrestrial, and hyper-gravity conditions in order to contribute to the understanding of mechanisms leading to the development of different grain morphologies and CET. In order to achieve this goal, the following sub-objectives are identified:

- to develop a transient numerical method for the investigation of directional solidification in absence of convection (*e.g.*, microgravity conditions) in cylindrical samples;
- to perform simulations of experimental scenarios and parametric investigations in order to gain a better understanding of the influence of process parameters on temperature and grain structure evolution, with particular focus on phenomena such the formation of radial columnar grains and CET;
- to include the effect of thermal convection in the model in order to investigate solidification under terrestrial and hyper-gravity conditions in centrifuges;
- to perform numerical simulations in order to gain a better understanding of the influence of different gravity levels on the development of flow patterns in the melt during directional solidification, and their effect on the evolution of temperatures and grain structures in the samples.

Each of these points is addressed in the thesis, providing enlightenment on different aspects of the solidification process under consideration, as shown in figure 1.7. In fulfilment of the first task, a 2D axisymmetric enthalpy method for Bridgman solidification of binary alloys in the absence of convection is developed. Following this, the model is expanded to include a front tracking algorithm, and applied to investigate Bridgman/power down solidification of γ-TiAl samples in absence of convection. Finally, according to the third task, the front tracking model is further expanded by incorporating the treatment of thermal convection arising under terrestrial gravity and hypergravity conditions in a centrifuge.

To accomplish the second and fourth tasks, the three models are used for simulating different experimental scenarios, both from the literature and from experiments carried out in the frame of GRADECET. These simulations corroborate the ability of the models in reproducing realistic results. Furthermore, they enable to gain information on hard to observe phenomena, such as transient evolution of temperature and fluid flow in the bulk of the samples, or transient growth of different grain morphologies. This gives a significant contribution to the analysis and understanding of experimental results, which usually consist in the measurement of surface temperatures and post mortem analysis of the solidified samples. In addition, throughout the thesis several parametric simulations are performed, in order to shed light on different queries arising either from gaps in the literature or from observation

of experimental data.

Model I, chapter 2: Bridgman solidification of binary alloys with NO CONVECTION	Model II, chapter 3: Bridgman/power-down solidification of TiAl alloys with NO CONVECTION	Model III, chapter 4: Power-down solidification of TiAl alloys with THERMAL CONVECTION
ENTHALPY MODEL	FRONT TRACKING MODEL	FRONT TRACKING MODEL
• Parametric study on the influence of process parameters on the development of radial temperature gradients which might lead to radial columnar growth	• Evaluation of the dependence of radial columnar growth on the applied cooling rate • Parametric investigation of the likelihood of CET at different cooling rates, depending on equiaxed nuclei density an nucleation undercooling	• Evaluation of melt flow during top or bottom heated solidification under terrestrial gravity conditions • Parametric investigation of directional solidification in a centrifuge to study the influence of centrifugal and Coriolis forces on melt flow and solidification

FIGURE 1.7: Models and case studies addressed the thesis.

The different models proposed in the thesis were developed following a meticulous study of the literature, and implemented by the author into a solution code written using FORTRAN, briefly described in the Appendix. Unless where explicitly mentioned (*i.e.* section 2.5), no commercial solver was used, and all the simulations were run by the author using the FORTRAN code, while experimental data and results were either taken from the literature or provided to the author by other GRADECET partners.

1.4 Numerical modelling of alloys solidification

Modelling the solidification process of alloys is a challenging task in many respects [18, 19]:

- coupled, non-linear, conservation equations for mass, energy, species, and momentum must be solved for each phase;
- from a mesoscopic point of view, alloys do not exhibit a sharp interface between solid and liquid, but a mushy zone with changing properties where solid and liquid coexist;
- nucleation and growth of different grain structures (columnar and equiaxed), that interact in complex ways, must be modelled;
- phenomena taking place at different length scales are involved, *e.g.*, dendrite growth and fragmentation on the micrometres scale, and heat transfer and fluid flow on the scale of the casting (metres).

Several models that focus on different aspects of the solidification process can be found in literature (see figure 1.8). Some of these simulation techniques, like the phase field

method [20, 21], are extremely accurate in simulating the shape and features of each growing grain, but they are suitable only for microscale problems, due to their severe computational cost.

On the other hand, when the computational domain is macroscopic, the simplest way to model phase change problems is using single domain models, such as the enthalpy method [22–25]. These methods do not need to track phase interfaces, and are developed from volume averaging techniques based on mixture theory. In this case, solidification phenomena are included in the macroscopic transport equations through solid fraction evolution, averaged thermophysical properties and appropriate source terms, and latent heat effect is usually treated by the general enthalpy formulation. However, these models, despite being computationally efficient, suffer from significant limitations since they cannot identify different grain regions developing in the mushy zone, and hence they are unable to predict phenomena such as CET.

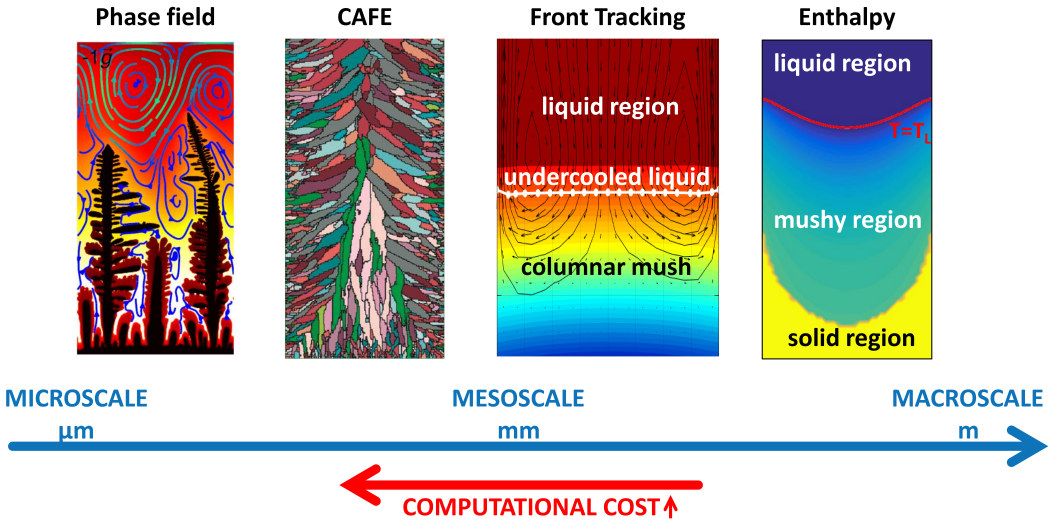

FIGURE 1.8: Different models for alloys solidification in relation to phenomena length-scale and computational cost.

Therefore, some bridging technique is needed that is able to capture, in some measure, the development of different grain morphologies, but at the same time retaining an acceptable computational cost to be used on macroscopic domains. With this purpose in mind, Spittle and Brown proposed a Monte Carlo technique to simulate solidification in small castings [26]. Another model was developed by Gandin and Rappaz [27], who coupled cellular automata (CA) techniques to simulate grain growth with finite elements (FE) flow calculations. This method, known as CAFE approach, allows the solution of heat flow on a fairly coarse grid (scale of geometric features of the casting), but requires a much finer mesh to simulate grain growth, typically of the order of 50-100 μm [18]. Hence, the requirement of such a fine grid

makes this method still quite computationally intensive to be applied to a whole casting domain.

A good compromise can be found in the front tracking method (FTM) by Browne and Hunt [28]. According to this approach, a front corresponding to the envelope of columnar grains tips is traced during the process. This allows the resolution of a region of undercooled liquid where equiaxed grains could nucleate and grow, leading eventually to the blocking of columnar grains. Once the undercooled liquid region is identified, CET can be investigated using either direct (*e.g.*, FTM for equiaxed growth [29]), or indirect (*e.g.*, Hunt analysis [30] or equiaxed index approach [31]) methods. At the same time, computational cost for this method is reasonable since calculations are performed on a fixed control volume grid of the order of millimetres, such as in the case of single domain models.

1.4.1 Front tracking method studies

In the work by Browne and Hunt [28], the front tracking technique was employed to model the problem of solidification of Al-2wt%Cu in the absence of convection on a 2D planar square domain. Even if some simplifying assumptions were used in this case, such as linear evolution of solid fraction with temperature and constant thermophysical properties, the effectiveness of the FTM was successfully verified via comparison with enthalpy method results.

An improved model was then proposed by McFadden and Browne [29]. In this case, several advances were introduced. In particular, an improved algorithm for solid fraction evolution according to Scheil law was included, as well as eutectic solidification and variable thermal conductivity. Furthermore, the FTM was extended to treat growth and impingement of multiple equiaxed grains.

Banaszek et al. [19,32] applied the FTM to model solidification in the presence of natural thermal convection. To do so, the FTM was coupled to a fully implicit control volume finite difference method for the solution of fluid flow and heat transfer phenomena. The columnar region was modelled as an isotropic porous medium. Equiaxed growth was not directly simulated. However, using an indirect approach for CET prediction (equiaxed index [31]), the influence of natural convection on the potential formation of equiaxed grains was evaluated. Results of this analysis showed that natural convection promoted the occurrence of CET. The model was also validated by comparison with Al-Si solidification experiments.

Mirihanage [33] employed the front tracking technique to predict CET in Al-7wt%Si castings in the presence of natural convection. In this study, the FTM, used to trace columnar growth and identify the undercooled liquid zone, was coupled with a volume averaging approach to follow the evolution of equiaxed grains. A mechanical blocking criterion was then

used to simulate CET, giving results in good agreement with experimental data.

Later, Seredyński and Banaszek [34] extended the FTM to study alloys solidification considering both thermal and solutal convection. The authors introduced some modifications to the original algorithm by Browne and Hunt [28]. In particular, they employed a grid independent method, where the markers forming the front could be located inside the control volumes, and not only on grid lines. This choice was made in order to simplify the algorithm for further extension of the model to 3D geometries [35]. In addition, a slurry model was included for treating the fluid flow in the undercooled liquid by modelling the growth of equiaxed grains as an increasing dynamic viscosity. To calculate the flow field, a single domain model based on the study of Ni and Incropera [36] was used to write conservation equations valid in the whole domain. In addition, a switching coefficient, defined as a function of the front position, was included in order to switch on and off specific terms, such as Darcy's term, or slurry model terms, in different regions. The model was compared with available experimental and numerical data from the literature and good agreement was found. Remaining discrepancies with experimental data were attributed to the assumption of an isotropic porous medium in the columnar region and the simple slurry model in the undercooled/equiaxed grain region. In ref. [35], an extension of the FTM to a 3D problem was proposed and applied for the solution of a solidification problem in a cubic cavity. Results where compared with those obtained by the 2D version of the model, finding good agreement. In addition, an analysis of the role of different dendrite tip kinetics was conducted, showing that the chosen dendrite growth model had a weak impact on the final results.

Within the framework of GRADECET, Mooney et al. [37] developed a hybrid 1D Bridgman Furnace FTM (BFFTM) for studying directional solidification, including the sample translation in accordance to the Bridgman solidification process. The BFFTM was developed for modelling solidification in cylindrical samples where heat flow could be regarded as 1D in the axial direction (small sample radius, $Bi<0.1$). In this case, the front was represented by a unique marker that could move in the axial direction. Unlike the previous FTMs, where the markers velocity was determined exclusively by the assumed dendrite tip kinetic law, in the BFFTM an additional velocity component was included to account for the movement of the sample. This model was firstly applied for studying Bridgman solidification of Al-7wt%Si, investigating the effect of pulling velocity jumps applied to the sample [37]. Finally, the BFFTM was adapted for treating solidification of multicomponent alloys (Ti-44.5Al-4.5Nb-0.2C-0.2B), and employed to examine a series of directional solidification experiments which combined power down and Bridgman techniques [38, 39]. This analysis allowed to characterize the heat transfer in the Bridgman furnace used during GRADECET experiments, and to evaluate conditions leading to CET. Nonetheless, due to the intrinsic limitation of the model to treat 1D problems, several aspects remain to be investigated, such as the development of radial heat fluxes and melt convection in the sample.

1.4.2 General methodology adopted in the thesis

In light of the discussion reported above, the front tracking method is identified as a suitable approach for modelling, at the scale of the sample, the directional solidification process of γ-TiAl alloys in different gravity environments, as required for the fulfilment of the thesis objectives. Hence, this section gives an overview of the main steps to be considered for the development of this model.

In the case of a general solidification process, the modelling of transport phenomena requires the solution of conservation equations for mass, energy, and momentum. In particular, considering the mixture theory, the set of macroscopic conservation equations, valid in all the solid, mushy, and liquid regions, is well established and can be found in the literature, such as in Bennon and Incropera [22] or in Ni and Incropera [36]. Table 1.1 reports the general conservation equations employed throughout the thesis. These equations are valid with the assumption of equal densities for the solid and liquid phases ($\rho_s = \rho_l = \rho$). Also, it is assumed that the solid phase velocity is either zero for stationary sample cases, or constant and equal to the pulling velocity in the case of Bridgman solidification. The term $\boldsymbol{S}$ in the momentum equation is a general source term representing the interactions of the solid and liquid phases. In the equations, the mixture value of a general variable ϕ_m in the solid-liquid mush is defined as a linear combination of its value in the liquid and solid phases as $\phi_m = g_s\phi_s + (1 - g_s)\phi_l$, where g_s is the fraction of solid phase in the mush.

TABLE 1.1: General mixture conservation equations.

Continuity	$\frac{\partial \rho}{\partial t} + \nabla \cdot (\rho \boldsymbol{u}_m) = 0$
Energy	$\frac{\partial H_m}{\partial t} + \nabla \cdot (H_m \boldsymbol{u}_m) = \nabla \cdot (k_m \nabla T) - \nabla \cdot [(H_l - H_m)(\boldsymbol{u}_m - \boldsymbol{u}_s)]$
Momentum	$\frac{\partial \rho \boldsymbol{u}_m}{\partial t} + \nabla \cdot (\rho \boldsymbol{u}_m \boldsymbol{u}_m) = -g_l \nabla p_l + \rho \boldsymbol{B} - \nabla \cdot \left[\rho \frac{g_s}{g_l}(\boldsymbol{u}_m - \boldsymbol{u}_s)(\boldsymbol{u}_m - \boldsymbol{u}_s)\right] - \nabla \cdot (\mu_l \nabla \boldsymbol{u}_m) + \boldsymbol{S}$

In the following chapters of the thesis, the conservation equations reported in table 1.1 are specialized, depending on the case study under consideration, by defining appropriately the different terms.

In order to solve the set of conservation equations, either explicit or implicit finite volume methods are employed in the thesis. Therefore, the discretized equations must be solved in each defined control volume (CV) of the computational domain representing the solidifying sample. As figure 1.9 shows, when an enthalpy method is used (chapter 2), the CVs can be of three types, *i.e.*, liquid ($g_s = 0$), mushy ($0 < g_s < 1$), or solid ($g_s = 1$). In this case, the

fraction of solid g_s in the CVs is calculated exclusively as a function of the local temperature.

On the other hand (see figure 1.9), when the front tracking model is employed (chapters 3 and 4), four types of CVs are identified, *i.e.*, liquid, partially liquid and partially mushy (CVs containing the front), mushy, and solid. For this reason, a new variable G_s is defined to represent the overall fraction of solid in a CV, which is proportional to the fraction of solid of the mush and the volume of the mush in the CV: $G_s = g_s \frac{V_m}{V_{CV}}$. Clearly, in fully mushy CVs, $g_s = G_s$. The volume of mush V_m in a CV is calculated from the position of the front.

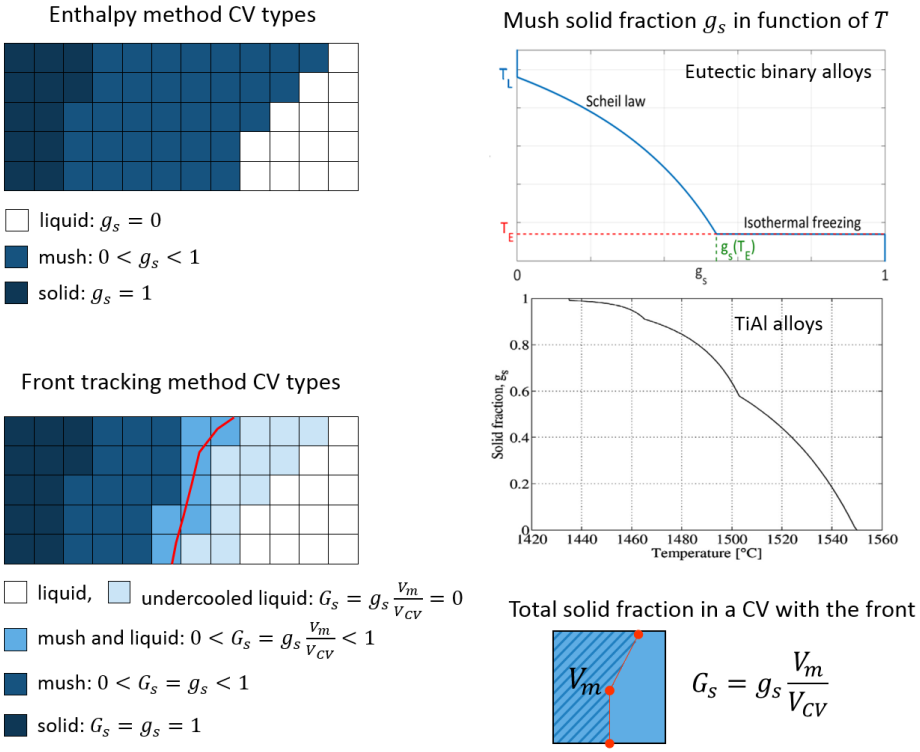

FIGURE 1.9: Enthalpy method versus front tracking method control volume types and calculation of solid fraction.

The front is composed by a series of markers connected by linear segments, and represents the envelope of the columnar grain tips. Hence, the displacement of the markers in time models the growth of the columnar grain region during the solidification process. In particular, the markers advance in a direction which is normal to the front, and their speed is calculated according to a dendrite tip kinetic law, function of the local undercooling, characteristic for the alloy under consideration.

For a more detailed and specific description of the different algorithms and procedures adopted, please refer to each chapter's methodology section (sections 2.2, 3.2, and 4.2).

1.5 Thesis structure

This work is presented in the form of "Thesis by publications", therefore the following chapters correspond to research papers which are either published or submitted for publication.

In accordance to this format choice, the structure of each chapter reflects the specific journal paper, including an introductory section where the relevant literature is discussed and objectives of the paper are identified. This is followed by a specific methodology section, where the main equations, model description, and case studies are illustrated. Finally results and conclusions are discussed. Also, "addendum" sections report additional results which are not included in the published documents. References are included at the end of each chapter.

The contents of the thesis are organized as follows:

- Chapter 2: reports the paper entitled *"Numerical simulation of Bridgman solidification of binary alloys"* [40] [2], published in the International Journal of Heat and Mass Transfer. Here, a transient 2D axisymmetric enthalpy model is presented and applied for the investigation of Bridgman solidification of binary alloys. A parametric investigation is reported, in order to contribute to the understanding of the influence of process parameters on important aspects such as the development of axial and radial temperature gradients in the solidifying sample. The addendum section reports a summary of the paper *"Code-to-code verification of an axisymmetric model of the Bridgman solidification process of alloys"* [41], published in the International Journal of Numerical Methods for Heat and Fluid Flow.

- Chapter 3: reports the paper entitled *"Axisymmetric front tracking model for the investigation of grain structure evolution during directional solidification"* [42] [3], published in the International Journal of Heat and Mass Transfer. In this paper, the model is improved by the inclusion of the front tracking algorithm and is applied for the simulation of experimental scenarios involving combined Bridgman and power down solidification of TiAl alloys. Empirical results are used for validating the model and tuning boundary conditions. Furthermore, the model is used to provide enlightenment on mechanisms leading to undesired radial columnar growth, which was found to block axial columnar growth and prevent CET during previous experiments. CET is parametrically investigated by the means of indirect methods (equiaxed index and Hunt's analysis). In particular, an adaptation of Hunt's model to the 2D front tracking is illustrated in the addendum (results presented at the SP17 and TMS2018 conferences).

- Chapter 4: reports the paper entitled *"Influence of natural and forced gravity conditions during directional columnar solidification"* [43] [4], published in the International

[2] https://doi.org/10.1016/j.ijheatmasstransfer.2016.08.030
[3] https://doi.org/10.1016/j.ijheatmasstransfer.2017.07.095
[4] https://doi.org/10.1016/j.ijheatmasstransfer.2018.05.151

Journal of Heat and Mass Transfer. This paper introduces a further development of the numerical model by the inclusion of thermal convection induced either by terrestrial gravity or by accelerations due to centrifugation. Data from power down solidification experiments carried out in the framework of GRADECET are used to set up boundary conditions for the simulations. The influence of terrestrial gravity is then investigated by considering different furnace configurations (top or bottom heated). Furthermore, a parametric investigation is performed in order to understand the influence of centrifugal and Coriolis accelerations on fluid flow and solidification during centrifugal casting.

- Chapter 5: presents the overall conclusions for the thesis and provides suggestions for potential future work.
- Appendix: describes the main features of the FORTRAN code developed for the solution of the front tracking model adopted in the thesis.

Since the journal papers listed above are included in their entirety, it is acknowledged that some repetitions are present throughout the thesis. Nonetheless, each chapter reports different numerical models and case studies, so that none of the sections is deemed redundant.

References

[1] D. Dimiduk, "Gamma titanium aluminide alloys—an assessment within the competition of aerospace structural materials," *Mater. Sci. Eng. A*, vol. 263, no. 2, pp. 281–288, 1999.

[2] H. Clemens and S. Mayer, "Design, processing, microstructure, properties, and applications of advanced intermetallic TiAl alloys," *Adv. Eng. Mater.*, vol. 15, no. 4, pp. 191–215, 2013.

[3] F. Appel, H. Clemens, and F. Fischer, "Modeling concepts for intermetallic titanium aluminides," *Prog. Mater. Sci.*, vol. 81, pp. 55–124, 2016.

[4] N. Lavery, D. Jarvis, and D. Voss, "Emission mitigation potential of lightweight intermetallic TiAl components," *Intermetallics*, vol. 19, no. 6, pp. 787–792, 2011.

[5] C. Austin, "Current status of gamma Ti aluminides for aerospace applications," *Curr. Opin. Solid State Mater. Sci.*, vol. 4, no. 3, pp. 239–242, 1999.

[6] K. Kothari, R. Radhakrishnan, and N. M. Wereley, "Advances in gamma titanium aluminides and their manufacturing techniques," *Prog. Aerosp. Sci.*, vol. 55, pp. 1–16, 2012.

[7] E. A. Loria, "Quo vadis gamma titanium aluminide," *Intermetallics*, vol. 9, no. 12, pp. 997–1001, 2001.

[8] X. Wu, "Review of alloy and process development of TiAl alloys," *Intermetallics*, vol. 14, no. 10-11, pp. 1114–1122, 2006.

[9] J. Aguilar, A. Schievenbusch, and O. Kättlitz, "Investment casting technology for production of TiAl low pressure turbine blades – Process engineering and parameter analysis," *Intermetallics*, vol. 19, no. 6, pp. 757–761, 2011.

[10] D. Jarvis and D. Voss, "IMPRESS Integrated Project—An overview paper," *Mater. Sci. Eng. A*, vol. 413, pp. 583–591, 2005.

[11] M. Heppener, O. Minster, and D. J. Jarvis, "First results of ESA's IMPRESS Project," *Acta Astronaut.*, vol. 63, no. 1, pp. 20–23, 2008.

[12] I. Egry, R. Brooks, D. Holland-Moritz, R. Novakovic, T. Matsushita, E. Ricci, S. Seetharaman, R. Wunderlich, and D. Jarvis, "Thermophysical properties of γ-titanium aluminide: The european IMPRESS project," *Int. J. Thermophys.*, vol. 28, pp. 1026–1036, 2007.

[13] V. Witusiewicz, A. Bondar, U. Hecht, and T. Velikanova, "The Al–B–Nb–Ti system: IV. Experimental study and thermodynamic re-evaluation of the binary Al–Nb and ternary Al–Nb–Ti systems," *J. Alloys Compd.*, vol. 472, pp. 133–161, mar 2009.

[14] U. Hecht, D. Daloz, J. Lapin, A. Drevermann, V. T. Witusiewicz, and J. Zollinger, "Solidification of TiAl-based Alloys," *Mater. Res. Soc. Symp. Proc.*, vol. 1128, 2008.

[15] D. Daloz, U. Hecht, J. Zollinger, H. Combeau, a. Hazotte, and M. Založnik, "Microsegregation, macrosegregation and related phase transformations in TiAl alloys," *Intermetallics*, vol. 19, no. 6, pp. 749–756, 2011.

[16] H. Wang, G. Djambazov, K. Pericleous, R. A. Harding, and M. Wickins, "Modelling the tilt-casting process for the tranquil filling of titanium alloy turbine blades," *Modeling of Casting, Welding, and Advanced Solidification Processes - XII (MCWASP XII)*, pp. 61–68, 2009.

[17] A. Kartavykh, V. Ginkin, S. Ganina, S. Rex, U. Hecht, B. Schmitz, and D. Voss, "Numerical study of convection-induced peritectic macro-segregation effect at the directional counter-gravity solidification of Ti–46Al–8Nb alloy," *Intermetallics*, vol. 19, no. 6, pp. 769–775, 2011.

[18] J. A. Dantzig and M. Rappaz, *Solidification*. Engineering sciences, EFPL Press, 2009.

[19] J. Banaszek and D. J. Browne, "Modelling Columnar Dendritic Growth into an Undercooled Metallic Melt in the Presence of Convection," *Mater. Trans.*, vol. 46, no. 6, pp. 1378–1387, 2005.

[20] A. Karma, "Phase-field formulation for quantitative modeling of alloy solidification," *Phys. Rev. Lett.*, vol. 87, no. 11, pp. 115701–1–115701–4, 2001.

[21] A. Badillo and C. Beckermann, "Phase-field simulation of the columnar-to-equiaxed transition in alloy solidification," *Acta Mater.*, vol. 54, no. 8, pp. 2015–2026, 2006.

[22] W. D. Bennon, "A continuum model for momentum , heat and species transport in binary solid-liquid phase change systems- I . Model formulation," *Int. J. Heat Mass Transf.*, vol. 30, pp. 2161–2170, 1987.

[23] W. D. Bennon and F. P. Incropera, "Numerical Analysis of Binary Solid-Liquid Phase Change Using a Continuum Model," *Numer. Heat Transf.*, vol. 13, no. 3, pp. 277–296, 1988.

[24] V. Voller and C. Prakash, "A fixed grid numerical modelling methodology for convection-diffusion mushy region phase-change problems," *Int. J. Heat Mass Transf.*, vol. 30, no. 8, pp. 1709–1719, 1987.

[25] V. R. Voller, M. Cross, and N. C. Markatos, "An enthalpy method for convection/diffusion phase change," *Int. J. Numer. Methods Eng.*, vol. 24, no. 1, pp. 271–284, 1987.

[26] J. A. Spittle and S. G. R. Brown, "Computer simulation of the effects of alloy variables on the grain structures of castings," *Acta Metall.*, vol. 37, no. 7, pp. 1803–1810, 1989.

[27] C. A. Gandin and M. Rappaz, "A coupled finite element-cellular automaton model for the prediction of dendritic grain structures in solidification processes," *Acta Metall. Mater.*, vol. 42, no. 7, pp. 2233–2246, 1994.

[28] D. J. Browne and J. D. Hunt, "A Fixed Grid Front-Tracking Model of the Growth of a Columnar Front and an Equiaxed Grain During Solidification of an Alloy," *Numer. Heat Transf. Part B Fundam.*, vol. 45, no. 5, pp. 395–419, 2004.

[29] S. McFadden and D. J. Browne, "A front-tracking model to predict solidification macrostructures and columnar to equiaxed transitions in alloy castings," *Appl. Math. Model.*, vol. 33, no. 3, pp. 1397–1416, 2009.

[30] J. D. Hunt, "Steady state columnar and equiaxed growth of dendrites and eutectic," *Mater. Sci. Eng.*, vol. 65, no. 1, pp. 75–83, 1984.

[31] D. J. Browne, "A New Equiaxed Solidification Predictor from a Model of Columnar Growth," *ISIJ Int.*, vol. 45, no. 1, pp. 37–44, 2005.

[32] J. Banaszek, S. McFadden, D. J. Browne, L. Sturz, and G. Zimmermann, "Natural Convection and Columnar-to-Equiaxed Transition Prediction in a Front-Tracking Model of Alloy Solidification," *Metall. Mater. Trans. A*, vol. 38, no. 7, pp. 1476–1484, 2007.

[33] W. U. Mirihanage, D. J. Browne, G. Zimmermann, and L. Sturz, "Simulation of international space station microgravity directional solidification experiments on columnar-to-equiaxed transition," *Acta Mater.*, vol. 60, no. 18, pp. 6362–6371, 2012.

[34] M. Seredyński and J. Banaszek, "Front Tracking Based Macroscopic Calculations of Columnar and Equiaxed Solidification of a Binary Alloy," *J. Heat Transfer*, vol. 132, no. 10, pp. 102301–1 – 102301–10, 2010.

[35] M. Seredynski and J. Banaszek, "Front tracking approach to modeling binary alloy solidification," *Int. J. Numer. Methods Heat Fluid Flow*, vol. 24, no. 4, pp. 920–931, 2014.

[36] J. Ni and F. P. Incropera, "Extension of the continuum model for transport phenomena occurring during metal alloy solidification-I. The conservation equations," *Int. J. Heat Mass Transf.*, vol. 38, no. 7, pp. 1271–1284, 1995.

[37] R. P. Mooney, S. McFadden, M. Rebow, and D. J. Browne, "A Front Tracking Model for Transient Solidification of Al–7wt%Si in a Bridgman Furnace," *Trans. Indian Inst. Met.*, vol. 65, no. 6, pp. 527–530, 2012.

[38] R. P. Mooney, S. McFadden, Z. Gabalcová, and J. Lapin, "An experimental–numerical method for estimating heat transfer in a Bridgman furnace," *Appl. Therm. Eng.*, vol. 67, no. 1-2, pp. 61–71, 2014.

[39] R. P. Mooney, U. Hecht, Z. Gabalcová, J. Lapin, and S. McFadden, "Directional solidification of a TiAl alloy by combined Bridgman and power-down technique," *Kov. Mater. - Met. Mater.*, vol. 53, 2015.

[40] S. Battaglioli, S. McFadden, and A. Robinson, "Numerical simulation of Bridgman solidification of binary alloys," *Int. J. Heat Mass Transf.*, vol. 104, pp. 199–211, 2017.

[41] M. Seredyński, S. Battaglioli, R. Mooney, A. Robinson, J. Banaszek, and S. McFadden, "Code-to-code verification of an axisymmetric model of the Bridgman solidification process for alloys.," *Int. J. Numer. Methods Heat Fluid Flow*, vol. 27, no. 5, pp. 1142–1157, 2017.

[42] S. Battaglioli, A. Robinson, and S. McFadden, "Axisymmetric front tracking model for the investigation of grain structure evolution during directional solidification," *Int. J. Heat Mass Transf.*, vol. 115, pp. 592–605, 2017.

[43] S. Battaglioli, A. Robinson, and S. McFadden, "Influence of natural and forced gravity conditions during directional columnar solidification," *Int. J. Heat Mass Transf.*, vol. 126, pp. 66 – 80, 2018.

Chapter 2

Numerical Simulation of Bridgman Solidification of Binary Alloys

Abstract

A transient 2D axisymmetric numerical model for the Bridgman solidification process for a stationary furnace and moving sample is presented. The model is able to predict the evolution of temperature and solid fraction of binary alloys in cases where buoyancy induced convection is negligible, such as in microgravity conditions. A dimensionless form of the governing equations is derived in order to identify the dimensionless parameters that characterise the process, those being the Stefan, Péclet, and Biot numbers. The problem is solved using a finite volume method and an explicit time stepping scheme. To test the efficacy of the model, simulated results are compared with experimental data from the literature and acceptable agreement is obtained. Finally, a parametric analysis is performed for understanding the influence of the process parameters on solidification. One key feature of this study is the inclusion of a term describing the advection of latent heat due to the translation of the mushy zone with varying solid fraction. This thermal transport mechanism is shown to be significant, since its magnitude is comparable to the advection of sensible heat. It is also found that when small Biot numbers are due to low values of the heat transfer coefficients at the surface of the sample, rather than to small sample radii, advective mechanisms are enhanced resulting in more convex shapes of the liquidus isotherm. This highlights the importance of considering both axial and radial heat fluxes when describing the process.

2.1 Introduction

The Bridgman–Stockbarger solidification process, originally developed to produce single crystals [1, 2], allows for control of directional solidification. Figure 2.1 shows a simple schematic of a Bridgman furnace where a cylindrical sample is held inside a long and slender crucible. Using a series of controlled coaxial heaters and an adiabatic baffle zone, the sample is subjected to a thermal gradient along its length such that the material is fully molten at the

hotter end and fully solid at the colder end. As figure 2.1 shows, when samples of binary or multicomponent alloys are considered, a mushy zone (where solid and liquid phases coexist) develops. A relative axial translation, identified as the pulling speed u, is imposed between the sample and the furnace either by pulling the crucible from the hot to the cold regions while keeping the furnace stationary or by moving the furnace and keeping the crucible stationary. For typical constant pulling speed operation, steady state conditions are reached and the solidification process keeps pace with the relative translation speed of the sample. However, the sample will experience initial transient conditions during start-up and stopping periods.

In steady state operation, the cooling rate of the solidification process can be roughly estimated as the product of the temperature gradient in the axial direction, G, and pulling speed, u. Accurate information about the temperature gradient may be lacking because of the temperature distribution, and hence temperature gradients, change along the length of the sample. In addition, width, shape and position of the mushy zone during the solidification process depend on the temperature distribution to which the sample is subjected. In some processes, much attention is paid to the morphology of the solid–liquid interface. For example, radial temperature gradients can cause a deviation from a planar interface to either a concave or convex ones [3].

In some cases the Bridgman furnace is used in a transient mode of operation. For example, when a phenomenon such as the Columnar to Equiaxed Transition (CET) is investigated, it is necessary to establish transient conditions during the solidification process [4]. In this case, a step change in pulling rate (known as a velocity jump) can cause a CET. In other modes of operation, the Bridgman may use a combination of velocity jump and controlled power down of the heaters to provide the desired transient conditions in the sample [5].

In metallurgical studies, a Bridgman furnace under steady-state operation may be used to determine which conditions are favourable for the formation of different microstructural features in the final casting. For instance, specific steady-state conditions can be related to microstructural characteristics such as primary and secondary arm spacing in dendritic growth [6]. In most cases, due to the opaque nature of metal alloys, only a post mortem analysis is possible, whereby the samples are cut, polished, and etched after solidification and then observed by optical or electron microscopy techniques. These types of procedures allow for the direct observation of relevant details, like the final grain structure and size, or the dendritic arm spacing [7–10]. Nevertheless, the observation of some features may still be difficult, as in the case of alloys that experience solid-state phase transformations that may alter or completely remove the initial solidification microstructure [11]. The main disadvantage of post mortem analysis is the lack of time resolved information during the solidification process.

Additional methods may be employed to investigate the solidification phenomenon in real time. X-ray radiographic imaging has been used in some alloy systems to monitor the real-time evolution of the microstructure. However, the applicability of this technique is limited by strict requirements on the sample geometry (thin samples only) and segregation of solute species [12–15]. For example, Reinhart et al. [16] observed CET in a Bridgman furnace in real-time after a velocity jump was imposed on the sample. Another approach for gathering real-time information during Bridgman solidification is the use of the ultrasonic pulse-echo technique. In this case the time-of-flight of an ultrasonic signal reflected by the solid–liquid interface was measured and used to estimate the velocity of the solidification front [17, 18].

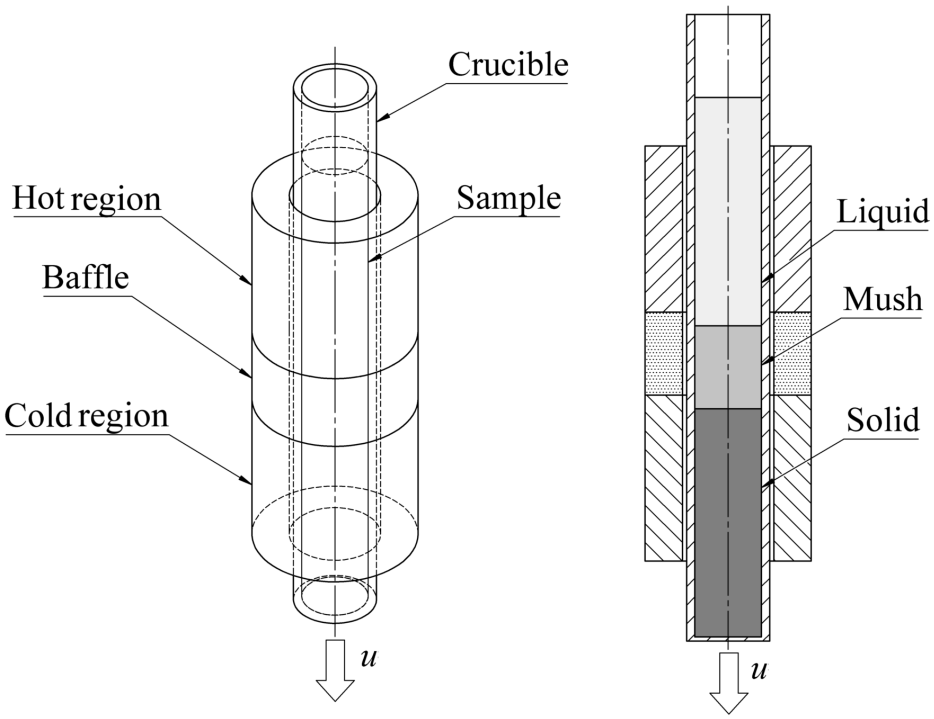

FIGURE 2.1: Schematic of a Bridgman furnace.

For the purpose of gaining accurate insight into the process, practitioners cannot always rely exclusively on experimental results. Therefore, reliable numerical models are valuable, and sometimes necessary tools for analysing alloy solidification. Simulations performed prior to physical experiments may be useful to predict the conditions that the material is likely to encounter during the process. In addition, computational models can be employed during or after the process to extract key information which would be difficult or impossible to observe or measure experimentally.

Nevertheless, it is crucial to highlight that the benefits of adopting numerical methods are highly dependent on the accuracy of the input data, the validity of initial modelling assumptions, and above all, the correctness of the model and solution technique themselves. Hence,

when possible, verification and validation of the model are essential steps in establishing the efficacy of the model predictions [19].

Several models for the investigation of the Bridgman solidification process of alloys have been developed in recent years. Timchenko et al. [20, 21] implemented a method, based on a single domain enthalpy approach, to study the evolution of temperature, solute concentration and solid–liquid interface during Bridgman solidification of Bi-1at%Sn. This model assumed furnace configurations with low growth speeds and high thermal gradients, allowing the model to treat the phase change as isothermal and without the formation of any mushy zone between solid and liquid. The simulated solutions showed good agreement with measured experimental results.

Mirihanage et al. [8] employed a front tracking method to simulate the advance of the columnar dendritic front and development of the undercooled region in Al-7wt%Si samples during Bridgman solidification in microgravity. The purpose of this study was to estimate the conditions for CET. Thermal data collected during experiments were used as inputs for the thermal boundary conditions. In the aforementioned models, the relative translation of sample and furnace was treated as a moving boundary condition. As a result, advection was not included in the conservation equations of the model.

A novel Bridgman Furnace Front Tracking Model (BFFTM) was developed by Mooney et al. [5, 22–24] where the boundary conditions were fixed and the movement of the sample was modelled by including an additional term in the energy equation for the advection of sensible heat. The model was used to solve an inverse heat transfer problem for the characterisation of the heat transfer conditions of a Bridgman furnace using experimental data as inputs [24]. The obtained thermal data were used in a subsequent study to investigate the solidification conditions during a series of experiments [5]. This particular BFFTM was based on a 1D hybrid approach; therefore its applicability was limited to cases when an axial heat flow assumption could be made, requiring that $\mathrm{Bi} < 0.1$.

The overarching objective of this study is to investigate the transient evolution of temperature and solid fraction during Bridgman solidification of binary alloys. To this end, a new 2D axisymmetric model is proposed that is capable of capturing both axial and radial heat flow within the cylindrical samples. Microgravity conditions are assumed, therefore buoyancy-induced convection is not considered. This assumption is applicable to practical cases, such as experiments carried out on the International Space Station or on sounding rockets [25], or experiments designed to suppress thermal and solutal convection in the sample [18]. Importantly, the new 2D model also accounts for the advection of latent heat due to the translation of the mushy zone with varying solid fraction within the mushy zone. The specific aims of this investigation are as follows:

1. to outline the details of a new general dimensional 2D axisymmetric numerical model for Bridgman solidification of binary alloys;
2. to derive a dimensionless form of the equation in order to identify key non-dimensional quantities that influence the evolution of temperature and solid fraction during solidification;
3. to test the efficacy of the general model by simulating a suitable and relevant experimental test case [18];
4. to perform a parametric analysis of the Bridgman solidification process so as to contribute to the understanding of the influence of different dimensionless parameters on temperature and solid fraction evolution.

2.2 Methodology

2.2.1 Model

To obtain the temperature field in the sample, the conservation equations for a mixture of solid and liquid phases must be solved. The general form of these equations is well established and may be found in Bennon and Incropera [26] and Ni and Incropera [27]. In order to reduce the complexity of the problem, the following assumptions are considered:

- negligible buoyancy induced convection;
- uniform velocity in the domain, equal for the solid and liquid phases ($\boldsymbol{u}_s = \boldsymbol{u}_l =$ pulling velocity u);
- constant and uniform density ρ in the sample.

With these assumptions, momentum and continuity equations are automatically satisfied so that it is sufficient to solve only the energy conservation equation. Applying the hypothesis of uniform axial velocity u to the general mixture energy equation [26, 27], it follows:

$$\frac{\partial H}{\partial t} + u\frac{\partial H}{\partial x} = \nabla \cdot (k \nabla T) \tag{2.1}$$

where enthalpy is defined as:

$$H = \rho \int_{T_{ref}}^{T} c_p dT + \rho \left(1 - g_s\right) L \tag{2.2}$$

Therefore, by substituting equation 2.2 into equation 2.1, the heat transfer equation written in terms of temperature becomes:

$$\rho c_p \frac{\partial T}{\partial t} = \frac{1}{r}\frac{\partial}{\partial r}\left(rk\frac{\partial T}{\partial r}\right) + \frac{\partial}{\partial x}\left(k\frac{\partial T}{\partial x}\right) + \rho L\frac{\partial g_s}{\partial t} - u\rho\frac{\partial\left(c_p T\right)}{\partial x} + u\rho L\frac{\partial g_s}{\partial x} \tag{2.3}$$

Note that r is the radial coordinate and x is the axial coordinate (figure 2.2). Since zero gravity conditions are assumed, the orientation of the axial direction is not relevant. The term on the left hand side of this equation represents the rate of change of sensible heat per unit volume. The first and second terms on the right hand side represent the conductive rate of heat flow per unit volume in the radial and axial directions. The third term accounts for the release of latent heat due to the solidification process. The fourth and fifth terms are, respectively, the rate of sensible and latent heat flow per unit volume due to the advection of material at the given pulling velocity u. Clearly, the terms that include variations of solid fraction g_s are present exclusively in the mushy zone. Hence, these terms are only present in alloy systems that exhibit a mushy zone and are not applicable in the case where there is a sharp interface between liquid and solid regions.

In the context of the past literature, Bridgman solidification of binary alloys under the assumption of negligible buoyancy induced convection was investigated by Mirihanage et al. [8] and by Mooney et al. [22]. In the case of Mirihanage et al., the relative translation between the sample and the furnace was simulated by applying moving boundary conditions. With the assumption of this reference frame, the effect of advection on solidification was intrinsically included in the boundary conditions hence the two advection terms of equation 2.3 were not considered in the model. Mooney et al., did model a moving sample, however the last term of equation 2.3 was not considered, which limits its range of applicability to cases when $c_p \gg L \cdot |\partial g_s/\partial T|$. Furthermore, this study focussed on scenarios where radial temperature gradients were negligible such that the heat flow throughout the sample could be approximated as 1D.

In the present study, the reference frame choice of a moving sample in a stationary furnace facilitates for the study of both advection thermal transport mechanisms on the solidification process. Also, the model considers 2D effects which can be significant with respect to the development of the mushy zone.

In order to solve equation 2.3, a closure relation for evaluating the evolution of the solid fraction, g_s, during the process must be included in the model. In the case of binary alloys, the solid fraction may be derived from the Scheil equation as follows [28]:

$$g_s = 1 - \left(\frac{T_M - T}{T_M - T_L}\right)^{\frac{1}{k_{part}-1}} \quad \text{for} \quad T_L < T < T_E,\ 0 < g_s < g_E \tag{2.4}$$

where g_E is the value of solid fraction at eutectic temperature, calculated by using $T = T_E$ in equation 2.4. Finally, eutectic solidification was assumed to be in equilibrium and was treated using a conservative enthalpy method for isothermal freezing at eutectic temperature T_E [29], such that,

$$g_s = 1 - \frac{H - c_p T_E}{L} \quad \text{for} \quad T = T_E,\ g_E \leq g_s < 1 \tag{2.5}$$

Specific heat capacity c_p and thermal conductivity k, in general, change as functions of temperature and are often different for the solid and liquid phases. Depending on the data available for the alloy under consideration, the model can accommodate these thermophysical properties as being either constants or variable. When distinct values for the different phases are available, the general property P in the mushy zone is calculated as follows:

$$P = (1 - g_s)\, P_l + g_s P_s \tag{2.6}$$

where P_l and P_s may be either constants or polynomial functions of temperature [30].

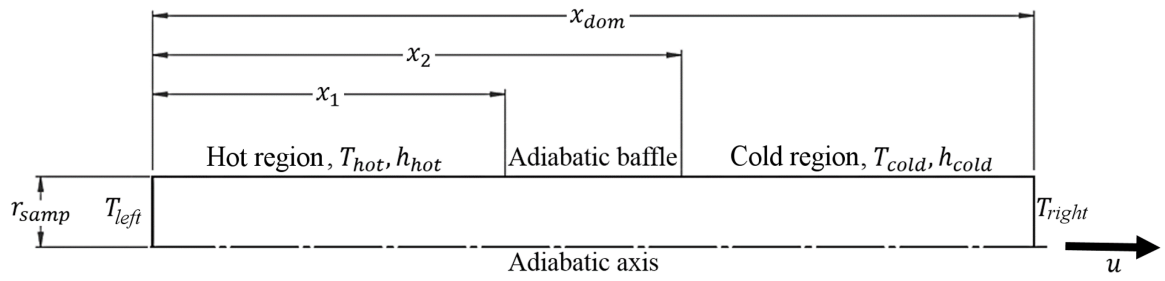

FIGURE 2.2: Computational domain for simulations.

Figure 2.2 shows the computational domain adopted for the simulations. As it is shown, the heat input and heat extraction zones are separated by an adiabatic baffle zone. The total length of the domain is x_{dom}, while the radius of the cylindrical sample is r_{samp}.

Since the problem is axisymmetric, half of the axial cross section of the sample was considered and an adiabatic boundary condition was assumed on the axis to enforce symmetry.

Dirichlet boundary conditions were applied at each end of the domain such that,

$$T(x,r,t) = \begin{cases} T_{left} & \text{for } x = 0 \\ T_{right} & \text{for } x = x_{dom} \end{cases} \tag{2.7}$$

where T_{left} and T_{right} could be either constant or variable with time.
To model the radial heat flow at the sample circumference, the following boundary conditions were applied along the interface between the sample and the heaters,

$$-k\frac{\partial T}{\partial r}(x, r_{samp}, t) = \begin{cases} h_{hot}(T - T_{hot}) & \text{for } 0 \le x < x_1 \\ h_{cold}(T - T_{cold}) & \text{for } x_2 < x \le x_{dom} \end{cases} \tag{2.8}$$

where T_{hot} and T_{cold} are the temperatures of the hot and cold heaters respectively. In reality, the heat flux between the furnace heaters and the sample has a convective component, $h_{conv}(T - T_{heater})$, as well as a radiative component, $h_{rad}(T^4 - T_{heater}^4)$. Nonetheless, the radiative component can be rewritten as:

$$q_{rad} = h_{rad}\left(T^4 - T_{heater}^4\right) \approx h_{rad} \cdot 4\overline{T}(T - T_{heater}) = \overline{h_{rad}}(T - T_{heater}) \tag{2.9}$$

from this approximation, an overall heat transfer coefficient, that includes both convection and radiation, can be defined as $h = h_{conv} + \overline{h_{rad}}$. Therefore, the heat transfer coefficients h_{hot} and h_{cold} in equation 2.8 include both convective and radiative heat transfer between the furnace and the sample.

Finally, at the interface with the adiabatic baffle, the radial heat flux is zero such that,

$$\frac{\partial T}{\partial r}(x, r_{samp}, t) = 0 \quad \text{for} \quad x_1 \le x \le x_2 \tag{2.10}$$

2.2.2 Non-dimensional formulation

In order to perform a parametric study, and to identify the dimensionless numbers that characterise the Bridgman solidification process, a non-dimensional formulation of equation 2.3 was derived. For this purpose, the following dimensionless variables are defined:

$$x^* = \frac{x}{l_{ref}}; \quad r^* = \frac{r}{l_{ref}}; \quad T^* = \frac{T}{\Delta T_{ref}}; \quad t^* = \frac{\alpha t}{l_{ref}^2} \tag{2.11}$$

where α is the thermal diffusivity, and l_{ref} and ΔT_{ref} are the length and temperature reference scales respectively. By substituting these quantities into equation 2.3, a new dimensionless formulation for the energy equation is obtained:

$$\frac{\partial T^*}{\partial t^*} = \frac{1}{r^*}\frac{\partial}{\partial r^*}\left(r^*\frac{\partial T^*}{\partial r^*}\right) + \frac{\partial^2 T^*}{\partial {x^*}^2} + \frac{1}{Ste}\frac{\partial g_s}{\partial t^*} - Pe\frac{\partial T^*}{\partial x^*} + \frac{Pe}{Ste}\frac{\partial g_s}{\partial x^*} \tag{2.12}$$

Note that, for the derivation of equation 2.12, all the thermophysical properties were considered constant.

Here, two dimensionless numbers are identified, the Péclet number and Stefan number:

$$Pe = \frac{u l_{ref}}{\alpha}; \quad Ste = \frac{c_p \Delta T_{ref}}{L} \tag{2.13}$$

From a physical point of view, the first parameter represents the relative magnitude of convective and diffusive transport of heat, whereas the second parameter represents the ratio of sensible and latent heat. In order to assign a meaningful value to the Stefan number for a eutectic alloy, the difference between the liquidus and eutectic temperatures of the alloy under consideration was used to define the reference temperature scale: $\Delta T_{ref} = T_L - T_E$.

It is also noticed that the axial variation of solid fraction is proportional to the ratio Pe/Ste. This quantity may be rewritten as follows,

$$\frac{Pe}{Ste} = \frac{\frac{u l_{ref}}{\alpha}}{\frac{c_p \Delta T_{ref}}{L}} = \frac{\frac{\rho u L}{l_{ref}}}{\frac{k \Delta T_{ref}}{l_{ref}^2}} \sim \frac{\text{convective latent heat transport}}{\text{diffusive heat transport}} \tag{2.14}$$

Therefore this dimensionless quantity has the same meaning as the Péclet number, in the sense that it represents the relative magnitude of conductive to advective heat transport, though for this instance it is latent heat advection opposed to that of sensible heat.
The dimensionless formulation of equations 2.4-2.10 was obtained in an analogous way; in particular, the convective condition expressed in equation 2.8 becomes:

$$-\frac{\partial T^*}{\partial r}\left(x^*, r^*_{samp}, t^*\right) = \begin{cases} Bi_{hot}\left(T^* - T^*_{hot}\right) & \text{for } \; 0 \leq x^* < x^*_1 \\ Bi_{cold}\left(T^* - T^*_{cold}\right) & \text{for } \; x^*_2 < x^* \leq x^*_{dom} \end{cases} \tag{2.15}$$

In doing so a third dimensionless number is identified, the Biot number Bi, defined as,

$$Bi = \frac{h l_{ref}}{k} \tag{2.16}$$

This quantity represents the relative magnitude of the diffusion resistance inside the sample and the convective resistance at the surface of the sample. To characterise the value of Bi along with the other dimensionless parameters the reference length scale was chosen as the ratio between the volume and the external surface where the heat transfer is occurring. Thus, for the cylindrical domain under consideration, the reference length scale is $l_{ref} = r_{samp}/2$ as is common for radial systems.

2.2.3 Numerical model

A finite volume numerical model was implemented for solving the problem outlined above. The cylindrical computational domain was divided into annular control volumes of length Δx and thickness Δr, as shown in figure 2.3. For practical purposes, related to the performance of a grid convergence study, half control volumes were considered at the boundaries.

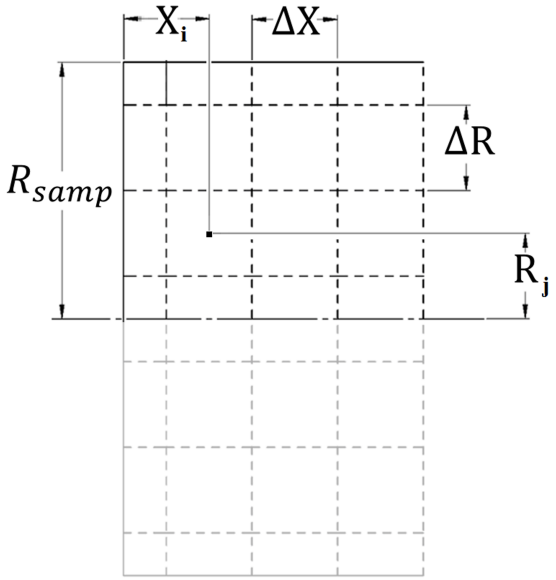

FIGURE 2.3: Domain discretization.

Using an explicit formulation in time, the temperature at the centre of a general control volume (i, j) at the new time step, given by the discretized heat equation 2.3, is:

$$\begin{aligned} T_{i,j}^{new} =& T_{i,j} + \frac{\Delta t}{\rho c_{p_{i,j}}} \left\{ \frac{1}{V_{CV\,i,j}} \left[\left(A_{si,j} q_{si,j} + A_{ni,j} q_{ni,j} \right) + \left(A_{wi,j} q_{wi,j} + A_{ei,j} q_{ei,j} \right) \right] \right. \\ & \left. - u\rho \frac{\left(c_{p_{ei,j}} T_{ei,j} - c_{p_{wi,j}} T_{wi,j} \right)}{\Delta x} + u\rho L \frac{\left(g_{sei,j} - g_{swi,j} \right)}{\Delta x} + \rho L \frac{\left(g_{si,j}^{new} - g_{si,j} \right)}{\Delta t} \right\} \end{aligned} \tag{2.17}$$

where the volume and faces of each control volume are calculated as follows:

$$\begin{aligned} & V_{CV\,i,j} = 2\pi r_j \Delta r \Delta x; \quad A_{wi,j} = A_{ei,j} = 2\pi r_j \Delta r; \\ & A_{si,j} = 2\pi \left(r_j - \frac{\Delta r}{2} \right) \Delta x; \quad A_{ni,j} = 2\pi \left(r_j + \frac{\Delta r}{2} \right) \Delta x \end{aligned} \tag{2.18}$$

The quantities q_s, q_n, q_w, and q_e are the heat fluxes at the faces of each control volume such that:

$$\begin{aligned} q_{si,j} &= k_{i,j_s}\frac{(T_{i,j-1}-T_{i,j})}{\Delta r}; \quad q_{ni,j} = k_{i,j_n}\frac{(T_{i,j+1}-T_{i,j})}{\Delta r}; \\ q_{wi,j} &= k_{i,j_w}\frac{(T_{i-1,j}-T_{i,j})}{\Delta r}; \quad q_{ei,j} = k_{i,j_e}\frac{(T_{i+1,j}-T_{i,j})}{\Delta r} \end{aligned} \tag{2.19}$$

The values of the thermophysical properties at the CV faces were calculated as harmonic means of the values at their respective centres [31]. The model adopted is explicit in time so that all the terms on the right hand side of equation 2.17 refer to the previous time step, except for the new value for solid fraction g_{snew}, given by the discretization of the time derivative of solid fraction in equation 2.3. To calculate this term, a Newton–Raphson iteration method was employed at each time step, similar to that described in [29]. This was required because the solid fraction is expressed by the Scheil equation 2.4 which is a non-linear function of temperature.

The numerical scheme for the solution of the dimensionless form of the equation is analogous and its derivation straightforward so is not discussed here for conciseness.
As an initial condition for the temperature distribution in the sample, an arbitrary piece-wise linear function was defined as follows:

$$T(x,r,0) = \begin{cases} T_{left} & \text{for } \; 0 \le x < x_1 \\ (T_{left} - T_{right})\,\frac{x-x_2}{x_1-x_2} + T_{right} & \text{for } \; x_1 \le x \le x_2 \\ T_{right} & \text{for } \; x_2 < x \le x_{dom} \end{cases} \tag{2.20}$$

In order to obtain a physically realistic distribution of temperature within the sample, during the first stage of the simulations the pulling velocity u was set to zero. The first stage lasted until temperature and solid fraction distribution settled to a steady-state solution. After this condition was reached, a velocity jump was applied to the sample.

2.2.4 Conditions for comparison with experimental data

In order to verify the efficacy of the model and solution technique, simulations were compared with data from experiments performed by Zimmerman et al. [18]. In the experiments, directional Bridgman solidification of Al-1.3 wt%Cu cylindrical samples was performed in a furnace with argon atmosphere. Three thermocouples were used to measure temperature evolution during the process and an ultrasonic pulse echo technique was employed to determine the growth rate. Importantly, the availability of time-dependent measurements makes this experiment particularly suitable for the comparison with the transient model developed

in this work. It is important to note that in the experiments the sample was stationary while the furnace was translated. On the contrary, the model simulates a moving sample in a stationary furnace. Nevertheless, since the pulling velocity was constant it is possible to compare the result by considering the simple relation $x = u \cdot t$.

Table 2.1 shows the setup parameters used for the comparisons. As shown in the last two columns, h_{hot} and h_{cold} were varied in different ranges of values. This calibration was necessary due to the impossibility to calculate precise values for the heat transfer coefficients relative to the considered experiments. In fact, such calculation would require the knowledge of precise data, such as heaters geometry and emissivity values, which are not available. Nonetheless, the values reported in table 2.1 were measured for a similar Bridgman furnace (sample diameter of 16 mm) with argon atmosphere [32, 33], hence the real heat transfer coefficients for the experiment are deemed to fall in this range.

TABLE 2.1: Setup for comparison with experimental data from Zimmermann et al. [18].

x_{dom}	Baffle length	r_{samp}	u	$T_{left} = T_{hot}$	$T_{right} = T_{cold}$	h_{hot}	h_{cold}
[m]	[m]	[m]	[m/s]	[°C]	[°C]	[W/(m^2°C)]	[W/(m^2°C)]
$200{\cdot}10^{-3}$	$4{\cdot}10^{-3}$	$4{\cdot}10^{-3}$	$2{\cdot}10^{-6}$	1100	25	[100,350]	[20,50]

2.2.5 Conditions for the parametric study

A parametric study was carried out simulating the Bridgman solidification process for a range of conditions aimed to gain knowledge with respect to the relative influence of each of the important dimensionless parameters, along with several key aspects of the solidification process, such as the temperature evolution, shape of the mushy zone and its position in the furnace.

The parametric study was performed by considering only variations corresponding to physically realistic scenarios, *i.e*, material properties were not allowed to change. Here, the length of the domain x_{dom} and the length and temperatures of the heaters were maintained constant and the same sample material was used for all the simulations, such that the thermophysical properties, and hence Ste, were constant.
Table 2.2 reports the dimensional input data used in the study, while table 2.3 shows the relevant dimensionless quantities relative to each simulation. An arbitrary reference setup (simulation S0) was selected and the following cases were considered:

- samples with different radii (simulations S1 and S2): x^*_{dom}, Pe and Bi change at the same time;
- different pulling velocities (simulations S3 and S4): only Pe changes;

- different heat transfer coefficients (simulations S5 and S6): only Bi changes.

Note that in this case arbitrary values for the heat transfer coefficients were used since this analysis does not attempt to reproduce a real experimental case study.

TABLE 2.2: Dimensional input values for parametric simulations.

Simulation run	x_{dom} [m]	x_1 [m]	x_2 [m]	$T_{left} = T_{hot}$ [°C]	$T_{right} = T_{cold}$ [°C]	r_{samp} [m]	u [m/s]	h [W/(m^2°C)]
S0	$200{\cdot}10^{-3}$	$90{\cdot}10^{-3}$	$110{\cdot}10^{-3}$	668	527	$2{\cdot}10^{-3}$	$0.5{\cdot}10^{-3}$	1000
S1	$200{\cdot}10^{-3}$	$90{\cdot}10^{-3}$	$110{\cdot}10^{-3}$	668	527	$1{\cdot}10^{-3}$	$0.5{\cdot}10^{-3}$	1000
S2	$200{\cdot}10^{-3}$	$90{\cdot}10^{-3}$	$110{\cdot}10^{-3}$	668	527	$4{\cdot}10^{-3}$	$0.5{\cdot}10^{-3}$	1000
S3	$200{\cdot}10^{-3}$	$90{\cdot}10^{-3}$	$110{\cdot}10^{-3}$	668	527	$2{\cdot}10^{-3}$	$0.25{\cdot}10^{-3}$	1000
S4	$200{\cdot}10^{-3}$	$90{\cdot}10^{-3}$	$110{\cdot}10^{-3}$	668	527	$2{\cdot}10^{-3}$	$1{\cdot}10^{-3}$	1000
S5	$200{\cdot}10^{-3}$	$90{\cdot}10^{-3}$	$110{\cdot}10^{-3}$	668	527	$2{\cdot}10^{-3}$	$0.5{\cdot}10^{-3}$	500
S6	$200{\cdot}10^{-3}$	$90{\cdot}10^{-3}$	$110{\cdot}10^{-3}$	668	527	$2{\cdot}10^{-3}$	$0.5{\cdot}10^{-3}$	2000

TABLE 2.3: Dimensionless input values for parametric simulations.

Simulation run	x^*_{dom}	r^*_{samp}	Ste	Pe	Bi
S0	20	2	0.211	0.1686	0.1250
S1	40	2	0.211	0.0843	0.0625
S2	10	2	0.211	0.3372	0.2500
S3	20	2	0.211	0.0843	0.1250
S4	20	2	0.211	0.3372	0.1250
S5	20	2	0.211	0.1686	0.0625
S6	20	2	0.211	0.1686	0.2500

Table 2.4 lists the thermophysical properties of the alloys used in the comparison with experimental data and in the parametric study. Al-1.3 wt%Cu was the alloy used by Zimmerman et al. in the experiments [18], and hence used in the comparison.

TABLE 2.4: Thermophysical properties of Al-1.3wt%Cu and Al-7wt%Si used in simulations.

	Al-1.3wt%Cu		Al-7wt%Si
	Solid	Liquid	
T_M / [°C]	660.2		660.2
T_L / [°C]	657		618
T_E / [°C]	547		577
k_{part}	0.17		0.13
ρ / [kg/m^3]	2500		2452.5
ρL / [J/m^3]	$961 \cdot 10^6$		$1064 \cdot 10^6$
c_p / [J/(kg°C)]	2396	496	1100
k / [W/(m°C)]	209	90.7	80

The material considered for the parametric study was Al-7 wt%Si. This alloy was selected both due to the availability of data in the literature and for its solidification behaviour. In fact, at eutectic temperature, the solid fraction is equal to 0.5417 which means that half of the solidification process occurs over a wide range of temperatures ($T_L - T_E = 41$°C). As such, a wide mushy zone develops during solidification. This characteristic is particularly suitable for observing the influence of the process parameters on this region.

2.3 Results and discussion

This section reports and discusses the results of the comparison with experimental data and of the parametric investigation. In all simulations the domain was divided into annular control volumes of length $\Delta x = 1$ mm and thickness $\Delta r = 1$ mm. The time step used in the simulations was equal to 0.001 s, which ensured the stability of the explicit scheme employed. Grid and time step independence for this choice were investigated and the numerical model was proven to be convergent. The estimated L2 norm of the truncation error due to the discretization was of the order of 0.1°C. It should be noted that a code-to-code verification exercise was performed with this model by comparing it with a commercial code (ANSYS Fluent). The details of this numerical verification are provided in section 2.5.

2.3.1 Comparison with experimental data

Due to the complex nature of the solidification process under consideration, there does not yet exist benchmark experimental data that can be leveraged to validate numerical simulations in accordance with established validation criteria [34]. As a result, relevant measurements from the literature have been used which means that the analysis cannot be regarded as a rigorous validation exercise, since the experiments do not provide all of the relevant data to reproduce exactly the same conditions. Regardless, the data provided from the experiments are sufficient to establish the veracity of the simulations provided that any assumptions, such as the magnitudes of the heat transfer coefficients, are within acceptable limits. Albeit adjustable parameters, there are established ranges for their magnitudes and, for the scenario under consideration here, adequate agreement was found when $h_{hot} = 300$ W/(m^2°C) and $h_{cold} = 40$ W/(m^2°C) which are acceptable values based on the literature [32, 33].

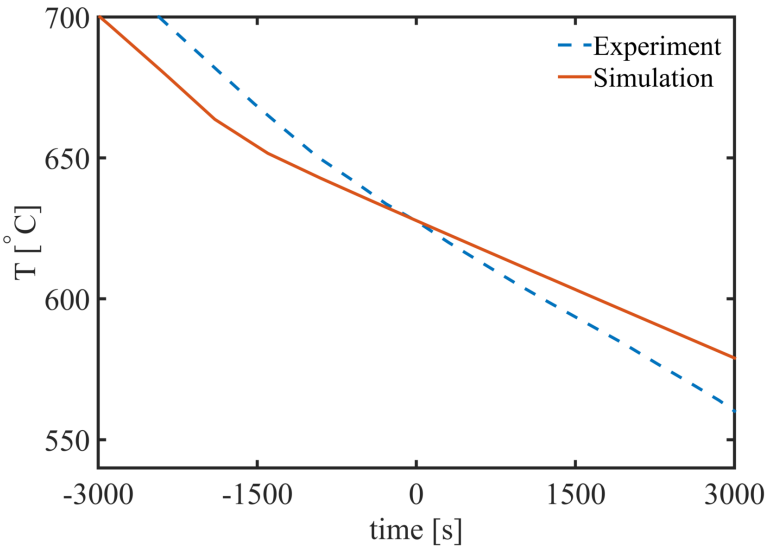

FIGURE 2.4: Measured and computed cooling curves at steady state, normalised to the time where the temperature equals the solidus temperature of the alloy in thermal equilibrium (627.5°C).

Figure 2.4 shows the cooling curve measured during the experiments by thermocouples at steady state during the pulling stage. This is compared with the computed cooling curve at steady state after the velocity jump. The time scale is normalised to the time where the temperature was equal to the equilibrium solidus temperature of Al-1.3 wt%Cu, which in this case is 627.5 °C. The experimental cooling rates were about $34 \cdot 10^{-3}$ °C/s in the liquid and $20 \cdot 10^{-3}$ °C/s in the solid. In the simulations, similar results were obtained, with cooling rates of $33 \cdot 10^{-3}$ °C/s in the liquid and $16 \cdot 10^{-3}$ °C/s in the solid.

Figure 2.5 shows the temperature gradient obtained from the difference of temperatures measured by two thermocouples located 16 mm and 10 mm above the measured solid–liquid

interface at the beginning of the pulling stage. Since the numerical model reproduces the actual formation of a mushy zone, instead of a sharp solid–liquid interface, the simulated temperature gradient in figure 2.5 was calculated as the difference of temperatures between two points located 16 mm and 10 mm ahead of the mid-point of the mushy zone. Time $t = 0$ s corresponds to the beginning of the pulling stage when the velocity jump was imposed.

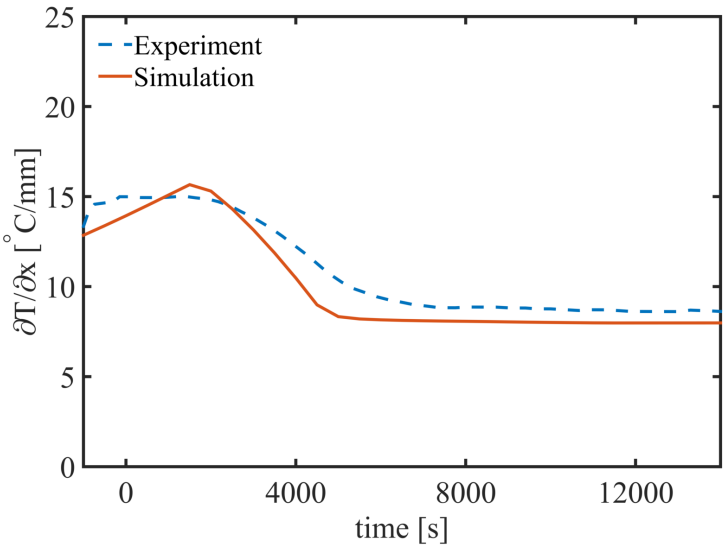

FIGURE 2.5: Axial temperature gradient taken from the temperature difference measured by two thermocouples and temperature gradient from simulations; time is normalised to the beginning of the pulling stage.

In general, the simulation results show qualitative agreement with experimental data from Zimmermann et al. [18]. Nevertheless, some differences are present. These differences could be due to several reasons. For example, the values of the heat transfer coefficients at the circumference were chosen in a realistic range for an argon atmosphere furnaces, but the actual values from the experiments were unavailable. Also, in reality the heat transfer coefficients may vary with axial position, while in the simulations constant values of h_{cold} and h_{hot} were assumed. In addition, for the Dirichlet boundary condition at the right and left ends of the sample, constant temperatures were assumed, since precise measurements of real temperatures from thermocouples were not available. Nonetheless, the agreement between the simulations and experiments was deemed to be acceptable, especially considering the uncertainty in the experimental data. In particular, figure 2.5 shows good agreement, demonstrating that the model was capable of effectively reproducing the axial temperature gradient.

Since the pulling velocity was very low ($u = 2 \cdot 10^{-6}$ m/s), and with respect to the resolution of the grid ($\Delta x = \Delta r = 1$ mm), it was not possible to observe a transient in the shape and position of the mushy zone envelope in the simulations for this test scenario. However,

it was possible to detect the duration of the transient phase by calculating the difference of temperature at subsequent time steps. The total duration of the transient stage was similar to the one measured in ref. [18]. During the experiments the transient stage lasted about 500 s while in the simulations a full steady-state condition was reached after about 530 s, which is deemed to be acceptable agreement.

Based on the verification work [35] and the validation attempt against the relevant but limited experimental data, it is believed that the model is sufficiently accurate that it can be used to provide correct physical insight into the influence of physical parameters on the Bridgman solidification process.

2.3.2 Influence of varying Pe and Bi on Bridgman solidification

The dimensionless parameters that characterise the Bridgman solidification process are the Stefan number Ste, Péclet number Pe, and Biot number Bi. Ste is defined as $c_p \Delta T_{ref}/L$. In the present work, the temperature range is defined as $\Delta T_{ref} = T_L - T_E$. Hence Ste represents the ratio of sensible and latent heat released across the temperature range where solidification occurs, *i.e.*, in the range of temperature where a mushy zone exists. With this choice, Ste is exclusively a function of the sample material properties and is not a variable process parameter. Hence variations in Ste were not characterized explicitly in the parametric study since only one alloy, Al-7 wt%Si, was considered. That is not to say that its influence is not considered since the ratio Pe/Ste defines the order of magnitude of the advection of latent heat, which is a key parameter under investigation in this work.

On the other hand, Pe and Bi are functions of the material properties as well as of process parameters such as pulling velocity, dimension of the sample and furnace heat transfer coefficients. Therefore, their variations were considered explicitly in the parametric study.

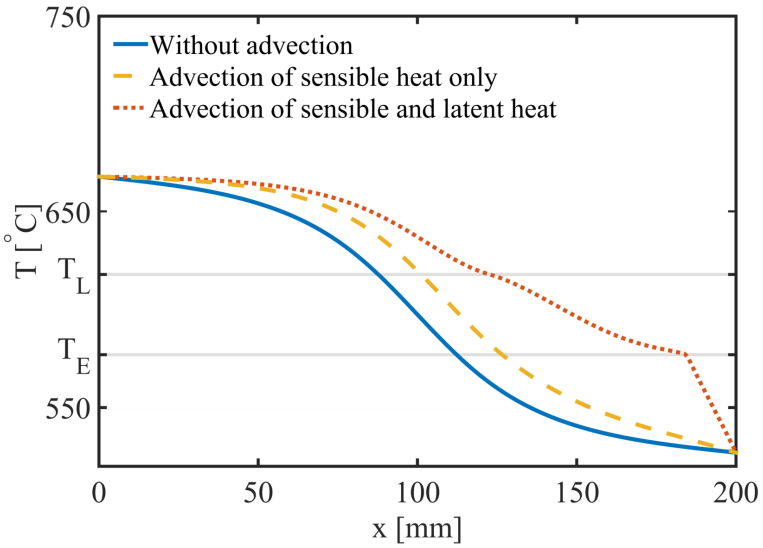

FIGURE 2.6: Simulation S0: temperature distribution on the axis of the sample, obtained with and without advection.

In the discussion, particular emphasis is placed on the evolution of the envelope of the mushy zone on the liquid side, corresponding to the liquidus isotherm ($T = 618°C$). In fact, depending on the magnitude of axial and radial heat fluxes at locations close to the liquidus isotherm, the development of different grain structures in front of the axial columnar grains which usually constitute the mushy zone in Bridgman processes could be promoted, *i.e.*, radial columnar or equiaxed grains. In particular, previous studies [5] suggest that negative radial thermal gradients close to this position could promote the growth of radial columnar grains, while this radial growth would be suppressed by positive radial thermal gradients.

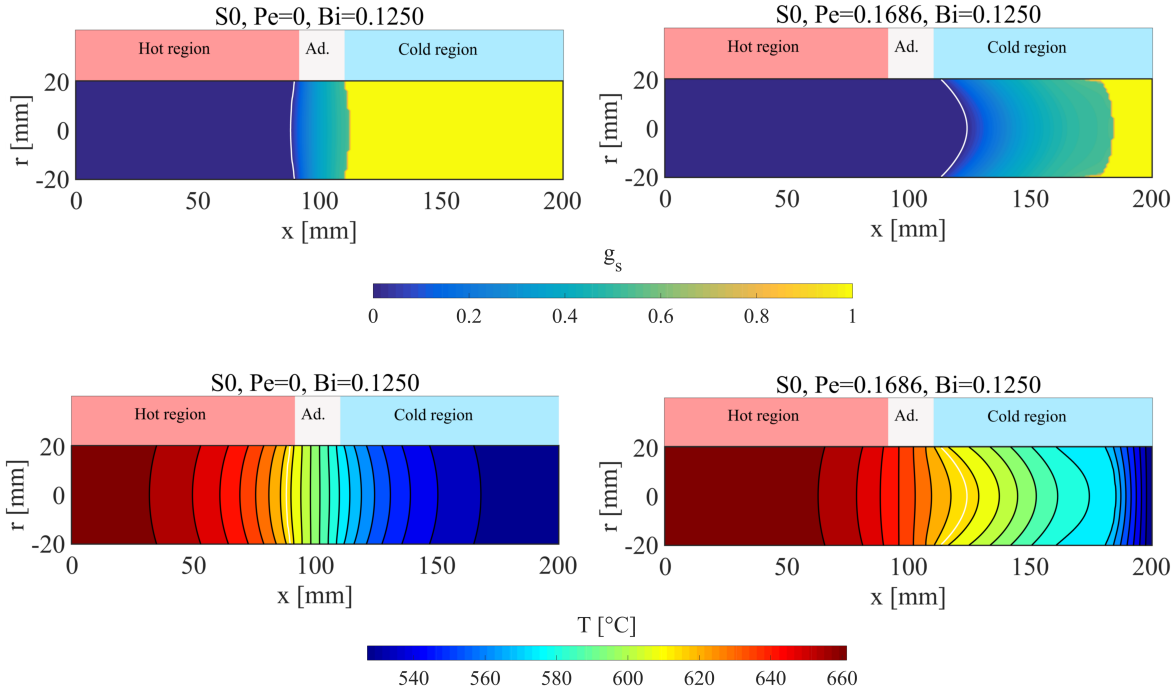

FIGURE 2.7: Simulation S0: solid fraction and temperature distribution in an axial section of the sample. Resting stage $Pe = 0$ (left), and pulling stage $Pe > 0$ (right).The white highlights the position of the liquidus isotherm, which represents the envelope of the mushy zone on the liquid side.

As mentioned earlier, the last two terms of the heat equation 2.12 describe the thermal transport by advection and are functions of Ste and/or Pe. In particular, the term that expresses the transport of sensible heat by advection is directly proportional to Pe, while the last term representing the transport of latent heat by advection is proportional to the ratio Pe/Ste. From table 2.3, $Ste = 0.211$, while Pe ranges between 0.0843 and 0.3372, such that $0.4 < Pe/Ste < 1.6$. From a scaling point of view, one would thus expect the latter to be the dominant advection mechanism in the mushy zone *i.e.*, within the region between the liquidus isotherm and the eutectic isotherm where the solid fraction is varying. To demonstrate the relative influence of each advection term, figure 2.6 shows the temperature distribution along the axis of the sample both with and without advection terms, for the baseline simulation S0. In one case, advection is assumed to be absent by setting $u = 0$. Advection of sensible heat only, as well as the case whereby advection of both sensible and latent heat together, are also simulated for comparison. It is clear that the steady state temperatures for the $Pe > 0$ cases are higher when the terms describing the advection of both sensible and latent heat are included. In particular, the inclusion of the advection of latent heat has a significantly higher impact on the temperature distribution, highlighting it as the dominant advection mechanism which is consistent with the scaling argument posed above.

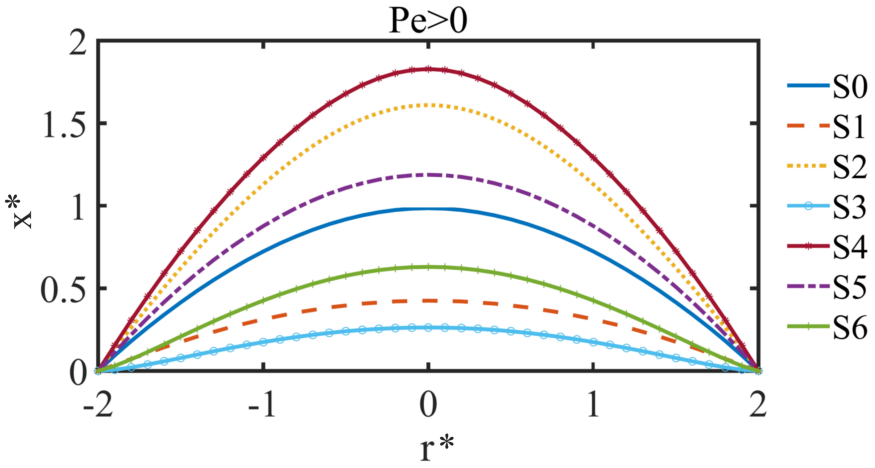

FIGURE 2.8: Curvature of the liquidus isotherm ($T = 618°C$) at steady state in the pulling stages; note that both axes are dimensionless.

Figure 2.7 shows the distribution of solid fraction and temperature in a cross section of the sample for the baseline simulation S0. The images on the left represent the steady state solution in the resting stage ($Pe = 0$), while the images on the right are the steady state solution reached during the pulling stage ($Pe > 0$). As it is shown, when the pulling velocity is zero the mushy zone is located within the adiabatic zone *i.e.*, 90 mm$\leq x \leq$ 110 mm. In this case, the liquidus isotherm is located marginally inside the left hand heat source side of the domain. Here, heat flows inward to the material from the heat source along its circumference such that $\partial T/\partial r > 0$, hence the liquidus line assumes a corresponding concave shape. Heat transfer from the heat source region to the heat sink region is thus predominantly axial, across the thin mushy zone, resulting in the steep temperature gradient observed in figure 2.6. Once steady state is achieved subsequent to the velocity jump ($Pe > 0$), the mushy zone moves to the right penetrating deep into the low temperature heat sink region. In contrast to the $Pe = 0$ case, the liquidus isotherm is now positioned within the heat sink region. Thermal access to the cold heat sink walls causes $\partial T/\partial r < 0$ for the entire mushy zone resulting in a convex liquidus isotherm. The figure also shows a substantially lengthened mushy zone, to the point that it occupies a significant portion of the heat sink domain. Latent heat is being released within this region, acting as a volumetric heat source term. Generation and advection of latent heat cause the higher temperatures over the mushy zone compared with the $Pe = 0$ case, as shown clearly in figure 2.6. There is also a prominent and almost discontinuous increase in the magnitude of the temperature gradient near the end of the heat sink region, which occurs after the end of the mushy zone ($T = T_E$). This is due to the fact that the latent heat terms, whose magnitude is particularly high in correspondence to the

eutectic zone where the solid fraction gradient is higher, drop abruptly to zero in the solid zone. Thus, the inclusion of advection, in particular for this case that of latent heat, has a significant influence on the heat transfer within the system, especially in the region where the solid fraction is varying. As will be discussed, advection and 2D effects are coupled and can influence the heat transfer and solidification mechanics, as is represented in figure 2.8 which shows a wide variation of the shape of the liquidus isotherms ($T = 618°C$) from each simulation listed in table 2.3 for the steady state pulling stage.

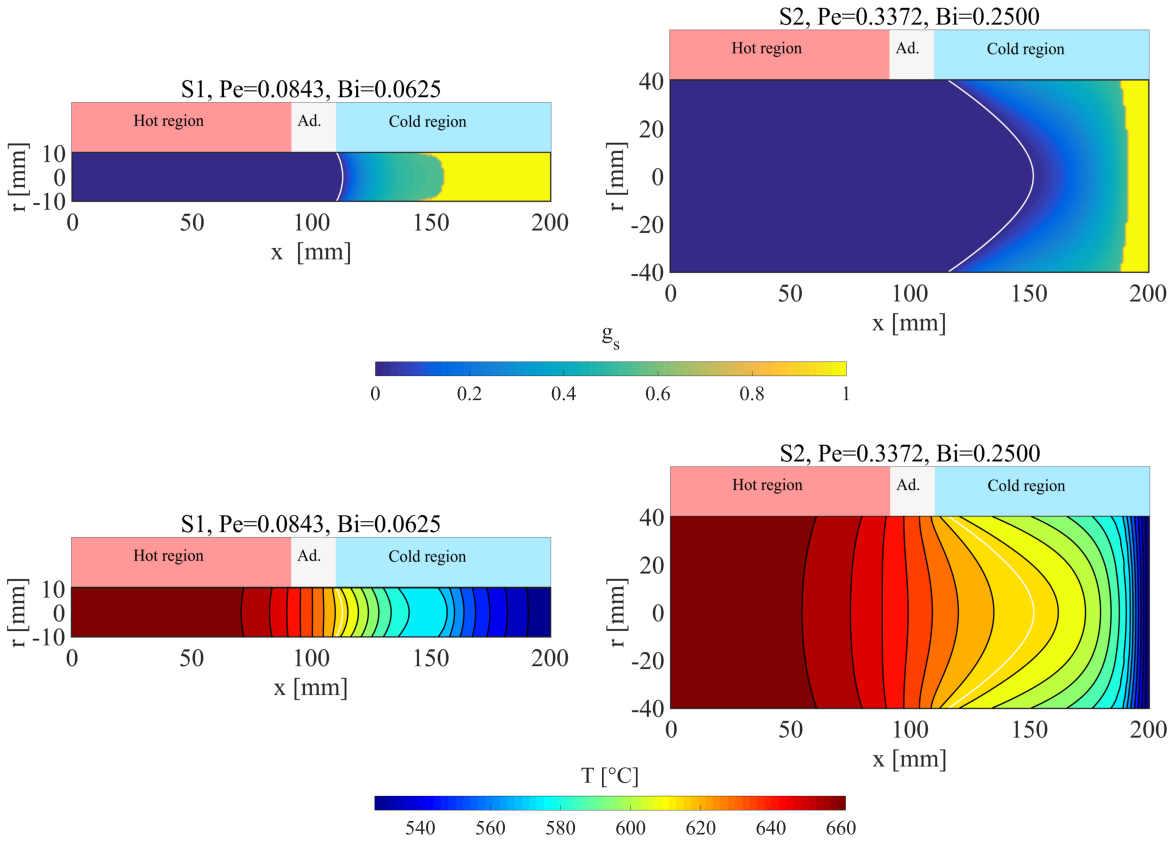

FIGURE 2.9: Simulations S1 (left) and S2 (right) showing solid fraction (top) and temperature distribution (bottom) in an axial section of the samples during the pulling stage ($Pe > 0$).

Figure 2.9 shows the steady state solution of solid fraction (top) and temperature (bottom) during the pulling stage for simulations S1 and S2, corresponding to $Bi = 0.0625$ and $Pe = 0.0843$, and $Bi = 0.25$ and $Pe = 0.3372$ respectively. When the radius is smaller (S1) Bi is also lower due to a reduction in the scale of the radial conductive thermal resistance within the sample. Compared with S2, the overall radial thermal gradients of S1 are expectedly weaker and the curvatures of the isotherms are notably smaller along the entire domain. In this comparison, Pe is also small for S1, so that advection is weak compared with thermal diffusion. Albeit weak, it is still sufficient to influence the position of the mushy zone such that it is located inside the cold heat sink region with the liquidus positioned just

outside of the adiabatic zone. Being inside the heat sink zone, heat is transferred both axially and radially which influenced the breadth of the mushy zone and curvature of the liquidus isotherm, showing low yet noticeable positive curvature in figure 2.8. In comparison, by increasing the radius (S2) the radial component of the conductive thermal resistance increases, increasing Bi, while at the same time the effect of advection becomes stronger by the increase in Pe. The former reduces the scale of radial conduction while the latter increases the scale of advection causing the mushy zone to penetrate deeper into the colder heat sink region. These two effects compound in such a way as to induce strong radial heat flow, including significantly more pronounced curvature of the liquidus isotherm, as seen in figure 2.8. For later reference, it is also worth noting that both Bi and Pe are directly proportional to the value of the sample radius, hence when r_{samp} changes the ratio Bi/Pe as well as $Bi/(Pe/Ste)$ remain constant.

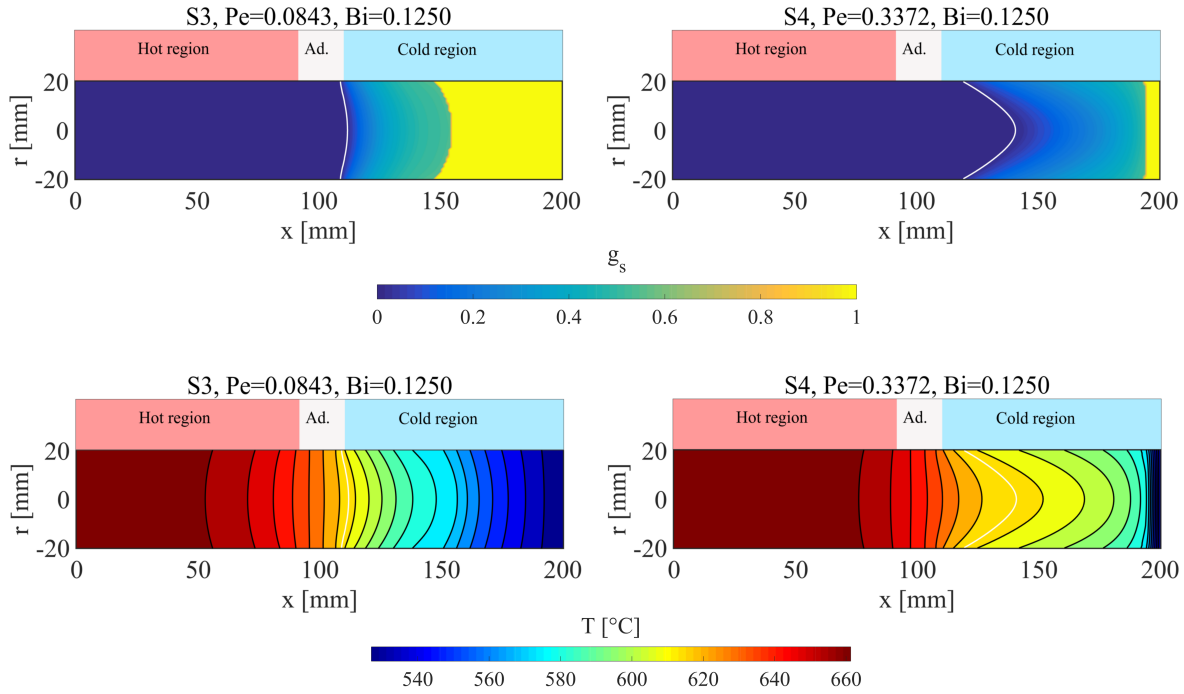

FIGURE 2.10: Simulations S3 (left) and S4 (right) showing solid fraction (top) and temperature distribution (bottom) in an axial section of the samples during the pulling stage ($Pe > 0$).

Figure 2.10 shows the steady state solution of solid fraction and temperature during the pulling stage for simulations S3 and S4, corresponding to $Pe = 0.0843$ ($Pe/Ste = 0.4$) and $Pe = 0.3372$ ($Pe/Ste = 1.598$) respectively. It is noticed from the temperature plots of figure 2.10 as well as the liquidus isotherm profiles of figure 2.8 that radial gradients are significantly higher for S4 even though the Biot number is the same for both cases, at $Bi = 0.125$. As implied considering S2 discussed above, the reason for this is that for certain cases advective thermal transport within the material can be significant and Bi does not account for this as

it only scales the relative magnitude of conduction within the sample and convection at the boundaries. To highlight this, figure 2.11 shows the distribution of the dimensionless rate of sensible heat flow by advection, $-Pe\partial T^*/\partial x^*$ (top), and latent heat flow by advection, $Pe/Ste \cdot \partial g_s/\partial x^*$ (middle). Since these terms are dimensionless, figure 2.11 illustrates the relative magnitudes of the two advective thermal transport mechanisms in order to reveal which one is dominant and over what region within the domain. When the pulling velocity is lower, Pe is lower. Therefore, in simulation S3 the advective terms are weaker and the mushy zone is located partially within the adiabatic zone and the curvature of the liquidus isotherm is low (figure 2.8), similar to the case S1 described earlier. Correspondingly, the length of the mushy zone is small. On the contrary, in simulation S4 Pe is significantly higher and both sensible and latent heat transfer by advection are more important. Advection causes the mushy zone to shift towards the cold end of the domain and the shape of the liquidus isotherm becomes notably more convex (figure 2.8) due to enhanced radial heat transfer. Considering the scales of to figure 2.11, it is clear that only the sensible heat advection is present in the single phase liquid and solid regions, whereas the latent heat advection is dominant within the mushy zone. Thus, advection of heat, both sensible and latent, can be an important factor in determining the thermal profile within the sample, which of course will influence the resulting grain structure of the resulting solid.

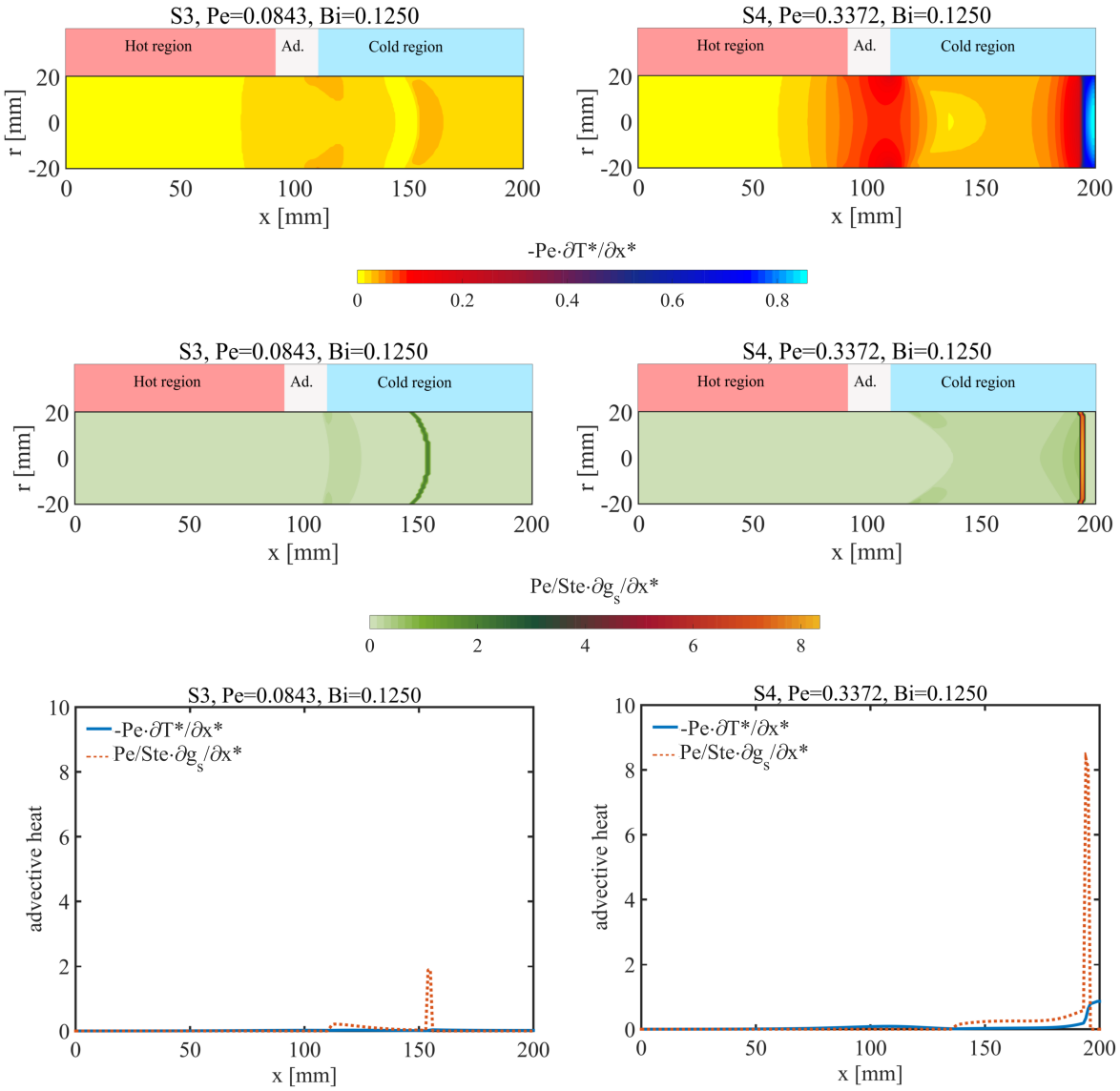

FIGURE 2.11: Simulations S3 (left) and S4 (right) showing the advective sensible heat term $-Pe\partial T^*/\partial x^*$ (top), the advective latent heat term $Pe/Ste \cdot \partial g_s/\partial x^*$ (middle), and the comparison of the two terms at $r = 0$; note that these terms are dimensionless.

The above discussion indicates that 2D effects, here broadly considered by scrutinising the shape of the liquidus isotherm, are strongly influenced by advective thermal transport. Above, the strength of this term was considered by increasing Pe, by increasing the length and velocity scales separately. As it was shown, increasing Pe has the effect of increasing the curvature of the liquidus isotherm even for the case when Bi is identical. However, all of the above simulated cases have the same heat transfer coefficient, in the sense that Bi was altered by changing the radius of the sample. Figure 2.12, on the other hand, shows the radial temperature gradient distribution in the samples for simulations S5 and S6 correspond to $Bi = 0.0625$ and $Bi = 0.25$ respectively, where Bi is increased for S6 by increasing the heat transfer coefficient whilst keeping the dimensions the same as S5. For reference, the

baseline S0 simulation corresponds to an intermediate case with $Bi = 0.125$ whilst having the same dimensions as S5 and S6. Each S0, S5 and S6 have the same $Pe = 0.1686$.

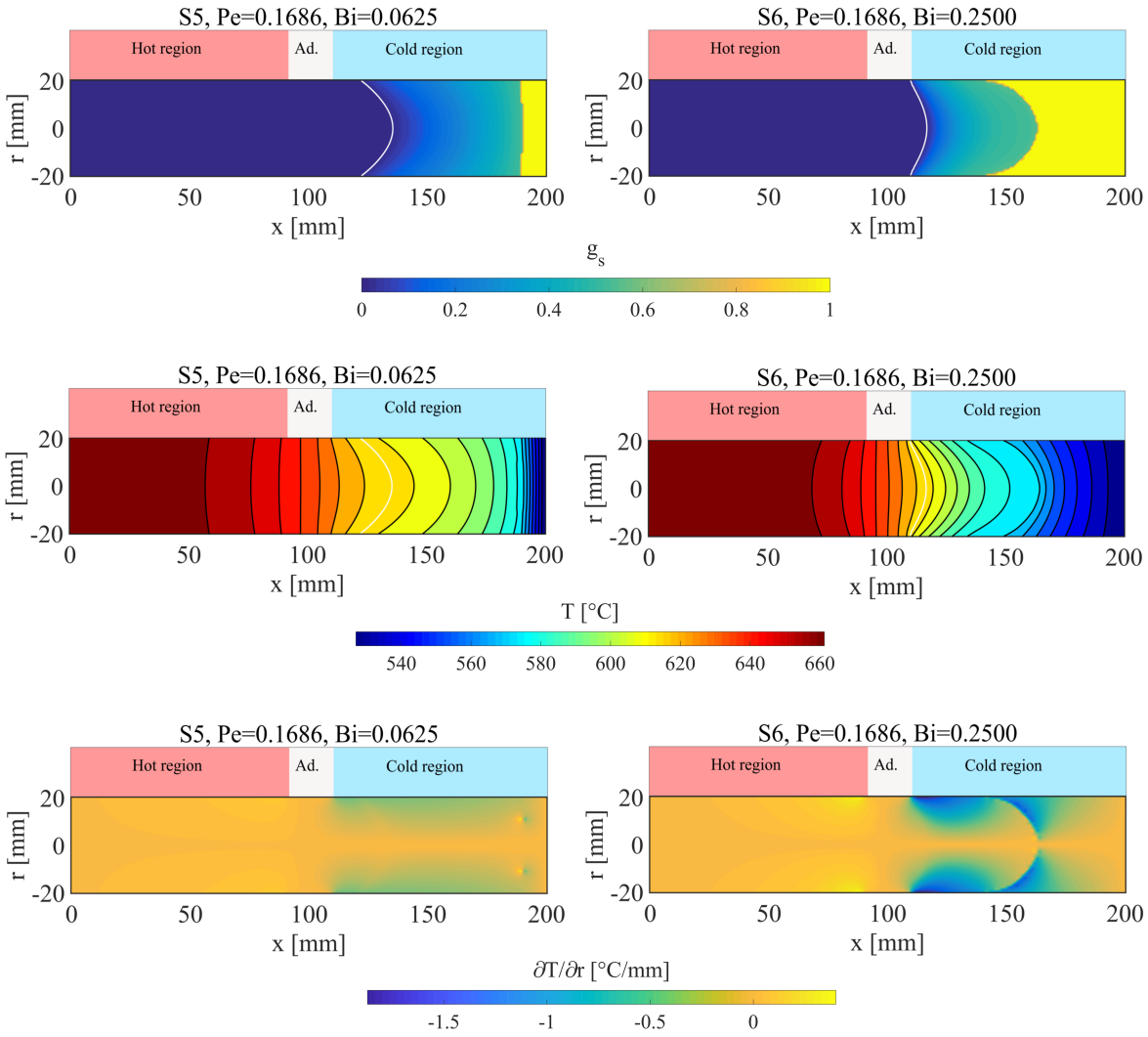

FIGURE 2.12: Simulations S5 (left) and S6 (right) showing the solid fraction, temperature distribution, and radial temperature gradient in an axial section of the samples during the pulling stage ($Pe > 0$).

Simulation S5 has a lower Bi compared with the baseline S0 case. This would suggest that the radial thermal gradients in the sample would generally be weaker than S6 due to the lower relative thermal resistance of convective heat transport compared with that of radial conduction. In fact, the mean value of the radial temperature gradient in the cold heat sink region at the circumference is $\partial T/\partial r \approx -0.6°\text{C/mm}$ in simulation S0 and $\partial T/\partial r \approx -0.4°\text{C/mm}$ in simulation S5, showing the expected trend. Similarly, in simulation S6 Bi is larger than that of both the S0 and S5 cases and the magnitude of the radial heat flux increases as is clear in figure 2.12. Here the mean value of the radial temperature gradient is $\partial T/\partial r \approx -0.8°\text{C/mm}$.

Thus, there is clear evidence that Bi in part determines the temperature distribution, including 2D radial effects, during Bridgman solidification of alloys due to the interplay of the conductive and convective thermal resistances. Interestingly however, figure 2.8 shows that, compared with the baseline S0 case, the curvature of the liquidus isotherm increases in simulation S5 and decreases in simulation S6, which is opposite to what one would expect based purely on a Biot number scaling argument *i.e.*, one that only includes convective and conductive thermal resistances to characterise 2D heat flow. This behaviour can be understood by observing the position of the mushy zone in the sample. It is evident that in simulation S5 the liquidus isotherm is located much deeper in the heat sink region even though Pe is the same as in S6. As discussed earlier, the radial heat fluxes are generally higher due to the relative location of the mushy zone with respect to thermal communication with the cold heat sink walls, since the latent heat generated during the phase change induces higher temperature gradient between the sample and the cold boundary. On the contrary, in simulation S6 the liquidus is located at the border region between the adiabatic and heat sink zone where the isotherms are inherently flatter. Although the location of the mushy zone accounts for the enhanced (S5) or the reduced (S6) curvature of the liquidus isotherm, the reason for the different positions is not immediately clear since the magnitude of advection, as defined by the scale of Pe, is the same in both simulations. However, this could be understood by considering the meaning of the ratios Bi/Pe and $Bi/(Pe/Ste)$. In fact, these two terms could be regarded to as the ratios of the sensible and latent heat advective resistances inside the sample to the convective resistance at the boundary, respectively. Therefore, when h is lower (S5), Bi/Pe and $Bi/(Pe/Ste)$ diminish, which means that the sensible and latent heat advective resistances in the sample are relatively lower. As a consequence, the mushy zone moves deeper in the cold region due to the enhanced effect of advection. On the contrary, when the heat transfer coefficient is higher (S6), Bi/Pe and $Bi/(Pe/Ste)$ increase, hence the sensible and latent heat advective resistances in the sample are greater and the effect of advection is reduced. For the alloy under consideration in this work, this effect is dominated by the latter of the two, meaning that the advection of latent heat largely determines this effect, though it cannot be generally stated that this is true for all alloys and will be the focus of future study.

2.4 Conclusions

This investigation aimed to contribute to the understanding of Bridgman solidification. In particular, this work focussed on numerical simulations which included 2D effects and the interaction of advective thermal transport mechanisms. With reference to the stated objectives the following steps were addressed:

1. A new 2D axisymmetric numerical model for Bridgman solidification of binary alloys was developed.

2. Key non-dimensional quantities that influence the evolution of temperature and solid fraction during solidification were identified as Stefan number, Péclet number, and Biot number.

3. The efficacy of the model was tested by simulating a suitable and relevant experimental test case [18].

4. A parametric analysis of the Bridgman solidification process was performed so as to contribute to the understanding of the influence of different parameters on temperature and solid fraction evolution.

The main conclusions from this study are as follows:

the Bridgman solidification process of binary alloy systems that exhibit a freezing range is characterized by several mechanisms of heat transfer. In particular, there is a strong interaction between the convective heat transfer at the boundaries, conduction and advection of sensible and latent heat in the sample. The parametric study showed that changing any of the process parameters, either in isolation or in combination, can induce significant and sometimes counter intuitive responses. This investigation suggests that, in order to anticipate the development of the mushy zone (position in the sample, shape of the mushy zone envelope), the single values of the dimensionless numbers Bi, Pe and Ste might not be sufficient, and that considering the ratios Pe/Ste, Bi/Pe and $Bi/(Pe/Ste)$ will give more relevant information on the process. One advantage of the proposed model is the ability to reproduce both axial and radial thermal gradients. This is an important feature for investigating Bridgman solidification, since magnitude and direction of heat transfer at locations close to the liquidus isotherm could lead to the formation of different grain structures in front of the axial columnar grains, *i.e.*, radial columnar or equiaxed grains [5]. In order to investigate the formation of different grain morphologies, plans for future work include the integration of a front tracking algorithm into the model. The front tracking method would facilitate the prediction of distinct regions in the mushy zone, namely columnar mush, equiaxed mush, or in the absence of equiaxed nucleation, constitutionally undercooled liquid regions.

2.5 Addendum

2.5.1 Code-to-code verification

In this section, the main results of a code-to-code verification of the 2D axisymmetric model described in section 2.2.1 are discussed.

As part of model development, a numerical model should be verified before it is validated. Validation is achieved by confirming agreement between numerical model simulations

and well-understood benchmark experiments. Verification (a prerequisite to validation) is preferably achieved by comparing numerical model simulation results against a closed-form analytical solution [19]. However, such closed-form solutions are often difficult or impossible to obtain. In the case where an analytical solution is unavailable, numerical modelling simulation results can be compared to alternative or established numerical models of the process; this approach is known as code-to-code verification. It is important to note that complete code verification can only be achieved using an exact analytical model, nonetheless the code-to-code approach is useful as a confidence building exercise in the overall model development process.

Therefore, results from the numerical model proposed in section 2.2.1 are compared to the ones obtained with the commercially established software ANSYS Fluent 15, which was adapted to solve the Bridgman solidification process of binary alloys by the inclusion of User Defined Function macros [35, 36]. In order to perform a thorough verification, different scenarios were considered, with different samples and furnace dimensions, and different alloy compositions (Al-7wt%Si and Al-11wt%Si). In this section, results for Bridgman solidification of Al-7wt%Si are reported as an example.

Tables 2.5 and 2.6 show the main input parameters for the specific case study. In particular, with the purpose of proving the ability of the model to solve correctly a transient process, two different pulling regimes are investigated, *i.e.*, a double velocity jump input, and a velocity ramp input.

TABLE 2.5: Input values for code-to-code verification.

x_{dom}	x_1	x_2	r_{samp}	$T_{left} = T_{hot}$	$T_{right} = T_{cold}$	h
[m]	[m]	[m]	[m]	[°C]	[°C]	[W/(m^2°C)]
$200{\cdot}10^{-3}$	$60{\cdot}10^{-3}$	$90{\cdot}10^{-3}$	$16{\cdot}10^{-3}$	668	527	1500

TABLE 2.6: Pulling velocity input data.

Simulation run	pulling velocity u / [m/s]	time t / [s]
S_{jump}	0	$t < 500$
	$0.5 \cdot 10^{-3}$	$500 \leq t < 800$
	$1 \cdot 10^{-3}$	$t \geq 800$
S_{ramp}	0	$t < 500$
	$\frac{t-500}{550-500} \cdot 1 \cdot 10^{-3}$	$500 \leq t < 550$
	$1 \cdot 10^{-3}$	$t \geq 550$

Figure 2.13 shows the thermal histories registered during the simulations S_{jump} (left) and S_{ramp} (right) at different axial locations. Recalling that in the setup under consideration the hot region of the furnace is located on the left (see figure 2.2), the temperature curves on the top correspond to earlier axial positions (x=63 mm), and the bottom ones to more advanced axial locations (x=87 mm). Results obtained using the non-commercial code are shown in blue, while the ones obtained with ANSYS Fluent are shown in red.

Clearly, the two models show good mutual agreement in their transient thermal responses, since the temperature curves are nearly coincident in all cases. The same level of agreement was found when comparing simulations for samples with a different radius [35], and for different alloy compositions [36], hence giving confidence in the efficacy of the non-commercial code.

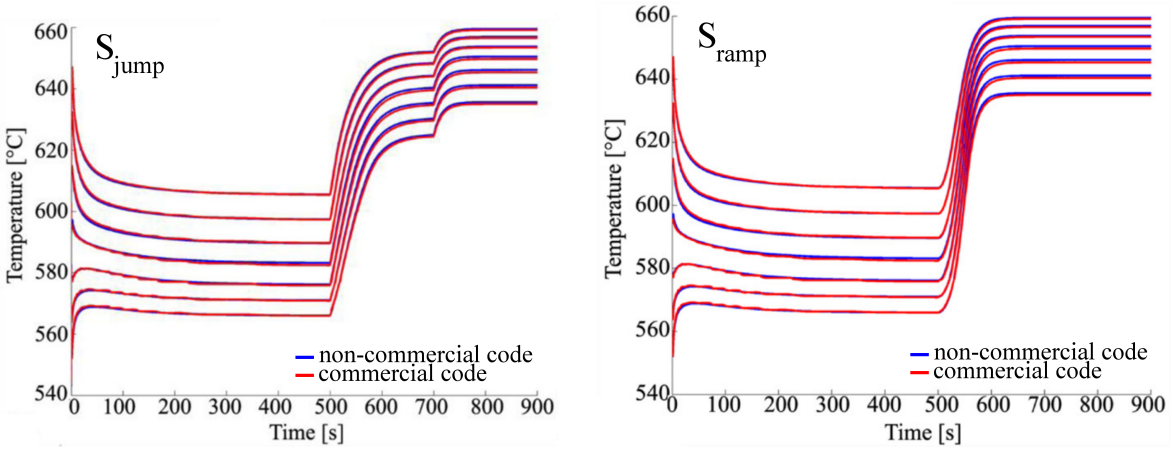

FIGURE 2.13: Temperature histories at several axial location in response to the velocity jump regime (left) and the velocity ramp regime (right). Axial location shown are: x=63 mm (top), 67 mm, 71 mm, 75 mm, 79 mm, 83 mm, and 87 mm (bottom).

Acknowledgements

The author would like to thank Dr. Gerhard Zimmermann and Dr. Laszlo Sturz for providing experimental data for comparisons. Also, gratitude goes to Dr. Mirosław Seredyński for carrying out the simulations in ANSYS Fluent and providing the results for the code-to-code verification.

References

[1] P. W. Bridgman, "Certain Physical Properties of Single Crystals of Tungsten, Antimony, Bismuth, Tellurium, Cadmium, Zinc, and Tin," *Proceedings of the American Academy of Arts and Sciences*, vol. 60, 1925.

[2] D. C. Stockbarger, "The Production of Large Single Crystals of Lithium Fluoride," *Rev. Sci. Instrum.*, vol. 7, no. 3, pp. 133–136, 1936.

[3] D. Kang, J. Liu, C. Jiang, and H. Xu, "Control of solid–liquid interface morphology and radial composition distribution: TbDyFe single crystal growth," *J. Alloys Compd.*, vol. 621, pp. 331–338, feb 2015.

[4] H. Jung, N. Mangelinck-Noël, H. Nguyen-Thi, B. Billia, G. Reinhart, and A. Buffet, "Directional solidification processing on CET in Al-based alloys," *Met. Mater. Int.*, vol. 15, no. 1, pp. 21–26, 2009.

[5] R. P. Mooney, U. Hecht, Z. Gabalcová, J. Lapin, and S. McFadden, "Directional solidification of a TiAl alloy by combined Bridgman and power-down technique," *Kov. Mater.*, vol. 53, no. 3, pp. 187–917, 2015.

[6] M. Gündüz and E. Çadırlı, "Directional solidification of aluminium–copper alloys," *Mater. Sci. Eng. A*, vol. 327, no. 2, pp. 167–185, 2002.

[7] D. Liu, N. Mangelinck-Noël, C.-A. Gandin, G. Zimmermann, L. Sturz, H. Nguyen Thi, and B. Billia, "Structures in directionally solidified Al–7wt.% Si alloys: Benchmark experiments under microgravity," *Acta Mater.*, vol. 64, pp. 253–265, 2014.

[8] W. U. Mirihanage, D. J. Browne, G. Zimmermann, and L. Sturz, "Simulation of international space station microgravity directional solidification experiments on columnar-to-equiaxed transition," *Acta Mater.*, vol. 60, no. 18, pp. 6362–6371, 2012.

[9] E. Çadırlı, "Effect of solidification parameters on mechanical properties of directionally solidified Al-Rich Al-Cu alloys," *Met. Mater. Int.*, vol. 19, no. 3, pp. 411–422, 2013.

[10] J. Fan, J. Liu, S. Tian, S. Wu, S. Wang, H. Gao, J. Guo, X. Wang, Y. Su, and H. Fu, "Effect of solidification parameters on microstructural characteristics and mechanical properties of directionally solidified binary TiAl alloy," *J. Alloys Compd.*, vol. 650, pp. 8–14, 2015.

[11] J. Lapin, Z. Gabalcová, U. Hecht, R. P. Mooney, and S. Mcfadden, "Columnar to Equiaxed Transition in Peritectic TiAl Based Alloy Studied by a Power-Down Technique," *Mater. Sci. Forum*, vol. 790-791, pp. 193–198, 2014.

[12] R. H. Mathiesen and L. Arnberg, "X-ray radiography observations of columnar dendritic growth and constitutional undercooling in an Al–30wt%Cu alloy," *Acta Mater.*, vol. 53, no. 4, pp. 947–956, 2005.

[13] S. McFadden, P. Schaffer, R. Mathiesen, and D. Browne, "Analysis of an Equiaxed Dendrite Growth Model with Comparisons to In-Situ Results of Equiaxed Dendritic Growth in an Al-Ge Alloy," *Mater. Sci. Forum*, vol. 654-656, pp. 1359—-1362, 2010.

[14] H. Nguyen-Thi, G. Reinhart, G. Salloum Abou Jaoude, R. Mathiesen, G. Zimmermann, Y. Houltz, and et al, "XRMON-GF: A novel facility for solidification of metallic alloys with in situ and time-resolved X-ray radiographic characterization in microgravity conditions," *J. Cryst. Growth*, vol. 374, pp. 23–30, 2013.

[15] G. Reinhart, H. Nguyen-Thi, N. Mangelinck-Noël, J. Baruchel, and B. Billia, "In Situ Investigation of Dendrite Deformation During Upward Solidification of Al-7wt.%Si," *JOM*, vol. 66, no. 8, 2014.

[16] G. Reinhart, N. Mangelinck-Noël, H. Nguyen-Thi, T. Schenk, J. Gastaldi, B. Billia, P. Pino, J. Härtwig, and J. Baruchel, "Investigation of columnar–equiaxed transition and equiaxed growth of aluminium based alloys by X-ray radiography," *Mater. Sci. Eng. A*, vol. 413, pp. 384–388, 2005.

[17] A. Drevermann, L. Sturz, N. Warnken, and G. Zimmermann, "Investigation of the initial transient in directional solidification of binary AlCu alloys," *Mater. Sci. Eng.*, pp. 259–262, 2005.

[18] G. Zimmermann, A. Drevermann, L. Sturz, and N. Warnken, "Time-dependent directional solidification of binary Al–Cu alloys in the initial transient," *Int. J. Mater. Res.*, vol. 98, no. 3, pp. 221–227, 2007.

[19] D. Pelletier and P. J. Roache, *Verification and Validation of Computational Heat Transfer*. Wiley-Blackwell, 2009.

[20] V. Timchenko, P. Y. P. Chen, E. Leonardi, G. De Vahl Davis, and R. Abbaschian, "A computational study of transient plane front solidification of alloys in a Bridgman apparatus under microgravity conditions," *Int. J. Heat Mass Transf.*, vol. 43, no. 6, pp. 963–980, 2000.

[21] V. Timchenko, P. Y. P. Chen, E. Leonardi, G. de Vahl Davis, and R. Abbaschian, "A computational study of binary alloy solidification in the MEPHISTO experiment," *Int. J. Heat Fluid Flow*, vol. 23, no. 3, pp. 258–268, 2002.

[22] R. P. Mooney, S. McFadden, M. Rebow, and D. J. Browne, "A Front Tracking Model for Transient Solidification of Al–7wt%Si in a Bridgman Furnace," *Trans. Indian Inst. Met.*, vol. 65, no. 6, pp. 527–530, 2012.

[23] R. P. Mooney and S. McFadden, "Order verification of a Bridgman furnace front tracking model in steady state," *Simul. Model. Pract. Theory*, vol. 48, pp. 24–34, 2014.

[24] R. P. Mooney, S. McFadden, Z. Gabalcová, and J. Lapin, "An experimental–numerical method for estimating heat transfer in a Bridgman furnace," *Appl. Therm. Eng.*, vol. 67, no. 1-2, pp. 61–71, 2014.

[25] R. Mooney, S. Rex, L. Froyen, S. McFadden, O. Budenkova, D. Voss, B. Schmitz, Y. Fautrelle, A. Kartavykh, and D. Browne, "Review of the maxus 8 sounding rocket experiment to investigate solidification in a ti-al-nb alloy," *European Space Agency, (Special Publication) ESA SP*, vol. 700, pp. 453–458, 2011.

[26] W. Bennon and F. Incropera, "A continuum model for momentum, heat and species transport in binary solid-liquid phase change systems—I. Model formulation," *Int. J. Heat Mass Transf.*, vol. 30, no. 10, pp. 2161–2170, 1987.

[27] J. Ni and F. P. Incropera, "Extension of the continuum model for transport phenomena occurring during metal alloy solidification-I. The conservation equations," *Int. J. Heat Mass Transf.*, vol. 38, no. 7, pp. 1271–1284, 1995.

[28] E. Scheil, "Bemerkungen zur schichtkristallbildungle," *Zeitschrift Fur Met.*, no. 34, pp. 70–72, 1942.

[29] S. McFadden and D. J. Browne, "A front-tracking model to predict solidification macrostructures and columnar to equiaxed transitions in alloy castings," *Appl. Math. Model*, vol. 33, pp. 1397–1416, 2009.

[30] S. McFadden, D. J. Browne, and C. A. Gandin, "A Comparison of Columnar-to-Equiaxed Transition Prediction Methods Using Simulation of the Growing Columnar Front," *Metall. Mater. Trans. A*, vol. 40, no. 3, pp. 662–672, 2009.

[31] S. Patankar, *Numerical heat transfer and fluid flow.* 1980.

[32] W. Rosch, W. Jesser, W. Debnam, A. Fripp, G. Woodell, and T. K. Pendergrass, "A technique for measuring the heat transfer coefficient inside a Bridgman furnace," *J. Cryst. Growth*, vol. 128, pp. 1187–1192, 1993.

[33] W. Rosch, A. Fripp, W. Debnam, and T. Pendergrass, "Heat transfer measurements in the Bridgman configuration," *J. Cryst. Growth*, vol. 137, no. 1-2, pp. 54–58, 1994.

[34] W. L. Oberkampf and C. J. Roy, *Verification and Validation in Scientific Computing.* Cambridge University Press, 2010.

[35] M. Seredyński, S. Battaglioli, S. McFadden, A. Robinson, and R. P. Mooney, "Verification of a 2D Axisymmetric Model of the Bridgman Solidification Process for Metallic Alloys," in *Proc. Eurotherm Semin. 109 Numer. Heat Transf. 2015*, 2015.

[36] M. Seredyński, S. Battaglioli, R. P. Mooney, A. Robinson, J. Banaszek, and S. McFadden, "Code-to-code verification of an axisymmetric model of the Bridgman solidification process for alloys," *Int. J. Numer. Method H.*, vol. 27, no. 5, 2017.

Chapter 3

Axisymmetric Front Tracking Model for the Investigation of Grain Structure Evolution During Directional Solidification

Abstract

The numerical investigation reported in the previous chapter shows that the heat and mass transfer associated with steady-state Bridgman furnace solidification is dependent on advection of sensible and latent heat, and also on the axisymmetric geometry of the sample. The present work extends the previous one by considering more complex non-steady solidification scenarios, where transient (limited-duration) Bridgman solidification is subsequently combined with a controlled power-down cooling process. A significant advancement with respect to the previous model is the inclusion of a front tracking method for the simulation of columnar growth. In the front tracking method the columnar mush region is demarcated by a series of markers that advance at a growth rate governed by the solutal undercooling at the dendrite tips. A classic micro-segregation law is used to govern the evolution of solid fraction in the columnar mush and the release of latent heat. The inclusion of the front tracking method provides greater insights into how heat fluxes and thermal conditions can influence the final grain structure. Firstly, it is shown that by analysing the trajectories of the markers, it is possible to predict the transition from axial columnar growth (directional solidification) to radial columnar growth due to significant radial heat fluxes in the sample. Secondly, it is demonstrated that model can simulate an undercooled liquid region ahead of the columnar front where equiaxed grains could possibly nucleate and grow, leading to a columnar to equiaxed transition (CET). Two indirect CET prediction methods from literature are included in the model to assess the likelihood of a CET occurring in the as-cast grain structure of the alloy. The model is employed to simulate experimental scenarios from literature involving a γ-TiAl alloy where the samples are subjected to different transient cooling conditions in a Bridgman furnace. Examples of axial columnar growth, radial columnar

growth, and CET are discussed in detail with elucidation from the model.

3.1 Introduction

Typical processing technologies for metallic components, such as investment casting or near net shape casting, involve melting and solidification. The grain structure that develops during the solidification process significantly influences the mechanical properties of the final product, and usually either fully columnar or fully equiaxed grains are desired. For example, in the case of directionally solidified turbine blades, axial columnar grains help to improve the creep resistance at high temperatures. On the other hand, equiaxed grains allow for higher strength and improved feeding in castings.

In order to produce a component that satisfies given requirements, it is crucial to understand how solidification process parameters influence the evolution of grain morphologies, leading to the formation of columnar grains, equiaxed grains, or a columnar to equiaxed transition (CET). In metallurgical research, a Bridgman furnace is well-suited for this purpose. Indeed, this apparatus (originally developed for the production of single crystals [1]) provides a means for the control of solidification parameters such as the nominal temperature gradient, cooling rate, and growth rate in a sample. A schematic of a Bridgman furnace was shown in figure 2.1. A heater and a crystallizer, separated by an adiabatic baffle, allow for the imposition of a desired axial temperature gradient, G, in the furnace. The sample is then translated with respect to the furnace towards the crystallizer at a pulling velocity, given by parameter u. In particular, during steady-state operation the growth rate of the solidification front keeps pace with the translation velocity, u, of the sample. Therefore, in such conditions the cooling rate of the solidification process can be approximated as the product of gradient and pulling velocity ($\dot{T} = G \cdot u$). In addition, Bridgman furnaces can be operated in a transient mode, for example by imposing step changes in the pulling velocity. This is required when transient phenomena such as CET are investigated [2]. Alternatively, Bridgman furnaces may be operated in stationary mode, *i.e.*, keeping $u = 0$ and imposing a cooling rate by varying the temperature of the heater in a controlled way. This mode of operation, which is not unique to Bridgman furnaces, is often referred to as power-down mode.

Several experimental and numerical studies, aimed at investigating grain structure evolution during Bridgman solidification, can be found in literature [3–7]. Most of these works consider binary alloys, such as Al-Si [4, 6], Al-Cu [3, 5], or Ti-Al [7]. Nonetheless, in recent years much attention has been paid to the study of multicomponent γ titanium aluminides. In fact, these intermetallic alloys are of particular interest due to their attractive mechanical and chemical properties such as low density, high specific strength and creep resistance at high temperatures [8–10]. Such qualities make γ-TiAl alloys excellent candidates as structural materials in advanced engineering applications, such as automotive and aeronautical

engines, where control of the microstructure and mechanical properties is essential.

Some examples of Bridgman solidification studies on γ-TiAl alloys, can be found in the archived literature. Saari et al. [11] investigated the columnar grains development in a directionally solidified γ-TiAl alloy at different pulling velocities. The experimental results showed that for lower withdrawal rates the grains were aligned to the axial direction of the casting. For faster rates, finer columnar grains were obtained, however they tended to converge towards the centre of the casting. This behaviour is due to the fact that for faster withdrawal rates, higher negative radial temperature gradients develop, as demonstrated in the previous chapter, hence columnar grains tend to grow towards the center of the sample.

Zhong et al. [12] performed a series of directional solidification experiments to investigate CET in Ti-48Al-2Cr-2Nb cylindrical samples. Their results suggested that growth rates below 500 $\mu m/s$ should be used to obtain fully columnar grain structures.

Lapin et al. [13] studied the solidification behaviour of two different TiAl based alloys, Ti-46Al-8Ta and Ti-46Al-8Nb, by performing two types of experiments, one at steady state conditions to investigate columnar dendritic growth, and another in transient mode to characterize CET. A CET diagram was experimentally determined for Ti-46Al-8Nb, however for Ti-46Al-8Ta the observation of CET was prevented by solid state phase transformation. In a subsequent study, Lapin et al. [14] carried out a series of combined Bridgman solidification and power down experiments with different cooling rates of Ti-44.5Al-4.5Nb-0.2C-0.2B samples. These experiments were designed to investigate directional solidification and CET. However, the experimental findings showed unwanted radial columnar growth, which in some cases appeared to prohibit the development of a CET. When CET occurred, regions with axial columnar, radial columnar and equiaxed grains were present, and it was observed that longer columnar grain regions corresponded to lower cooling rates.

Mooney et al. [15,16] employed a bespoke 1D transient Bridgman Furnace Front Tracking Model (BFFTM) for investigating the experiments by Lapin et al. [14]. Firstly, the model was applied to solve a steady state inverse heat transfer problem for the determination of the heat transfer coefficients at the circumference of the crucible [15]. Subsequently, in ref. [16], the thermal data obtained were used as boundary conditions for the series of combined Bridgman and power down experiments [14]. The 1D BFFTM directly modelled axial columnar growth, and was able to predict CET by indirect analysis of the conditions in the undercooled liquid ahead of the axial columnar front [16,17] (indirect CET prediction methods are reviewed in McFadden et al. [18]), but could not directly model radial growth. The 1D model did highlight the onset of conditions for radial growth (by showing a change in direction of the radial heat flux), but, nevertheless, the model was limited to predicting directional solidification along the axis.

Hence, the BFFTM by Mooney et al. is limited to cases when the thermal gradient can be assumed 1-dimensional in the axial direction, *i.e.*, when the sample radius is sufficiently small and the Biot number is lower than 0.1. In general, in order to include the effect of radial heat fluxes, which can induce the growth of radial columnar grains, it is necessary to extend the method to 3D geometries. Nevertheless, if the assumption of zero buoyancy-induced convection is considered, the cylindrical sample solidification process can be regarded as 2D axisymmetric.

In the previous chapter, the author developed a 2D axisymmetric transient model for the investigation of Bridgman solidification of binary eutectic alloys. The model assumed equilibrium solidification, therefore a mushy zone existed between the liquidus and eutectic temperatures, without distinction of the columnar and undercooled liquid regions. The evolution of solid fraction in the mushy zone was non-linear and followed Scheil law. The model, which was verified by code-to-code comparison [19], was employed in a parametric study [20] to understand the influence of process parameters on temperature and solid fraction evolution. Interestingly, the study suggested that, due to the combination of several heat transfer mechanisms, the existence of radial heat fluxes did not depend exclusively on the Biot number. This demonstrates the importance of using an axisymmetric geometry for a more accurate description of the process.

The work outlined here details the development of a transient model for the prediction of combined Bridgman and power down solidification of γ-TiAl alloys. The 2D axisymmetric thermal model is derived from the one described in ref. [20]. In order to model γ-TiAl instead of binary alloys, Scheil's law is replaced with a non-linear solid fraction to temperature relationship [15]. The main advancement with respect to the previous model is represented by the inclusion of a front tracking algorithm, similar to the approach of Browne and Hunt [21]. According to this method, the envelope of the columnar grains tips is represented by a series of markers connected by linear segments. These markers advance at a speed that is a function of the local undercooling. Furthermore, a series of inactive markers, set to nucleate when a given undercooling is reached, is placed on the sample circumference to simulate radial columnar growth. Ahead of the axial and radial columnar zone, a region of undercooled liquid is identified. Nucleation and growth of equiaxed grains in this region are not directly modelled, however the likelihood of CET is assessed indirectly with the equiaxed index by Browne [22] and with Hunt's method for CET prediction [23].

This new model is applied to the original experimental results from refs. [14, 16]. Using this extended approach, predictions of both axial and radial columnar growth morphologies are possible and will be demonstrated.

The main objectives of the present study are as follows:

- to illustrate the details of a 2D axisymmetric front tracking model for the investigation of transient Bridgman and power down solidification of multicomponent alloys;
- to simulate a series of experimets from refs. [14] and [16], involving combined Bridgman and power down solidification of γ-TiAl;
- to parametrically investigate the development of axial and radial columnar grains and CET.

3.2 Methodology

3.2.1 Thermal model

The general conservation equations for a mixture of solid and liquid phases may be found in refs. [24, 25]. In this work, the following assumptions are considered:

- negligible buoyancy induced convection;
- uniform velocity in the domain, equal for the solid and liquid phases ($u_s = u_l$ =pulling velocity u);
- constant and uniform density ρ in the sample.

With these assumptions, the momentum and continuity equations are automatically satisfied so that it is sufficient to solve only the heat equation [24, 25]:

$$\frac{\partial H}{\partial t} + u\frac{\partial H}{\partial x} = \nabla \cdot (k \nabla T) \tag{3.1}$$

The enthalpy of a control volume V_{CV} containing a volume of solid V_s is defined as:

$$H = \rho \int_{T_{ref}}^{T} c_p dT + \rho \left(1 - \frac{V_s}{V_{CV}}\right) L \tag{3.2}$$

In general, the volumetric solid fraction of a mushy volume V_m is defined as $g_s = V_s/V_m$, therefore the overall solid fraction within a given control volume CV containing a volume of mush V_m is equal to $g_s V_m/V_{CV}$. By substituting this definition and equation 3.2 into equation 3.1 it follows that:

$$\rho c_p \frac{\partial T}{\partial t} = \frac{1}{r}\frac{\partial}{\partial r}\left(rk\frac{\partial T}{\partial r}\right) + \frac{\partial}{\partial x}\left(k\frac{\partial T}{\partial x}\right) - u\rho\frac{\partial (c_p T)}{\partial x} + u\rho L\frac{\partial}{\partial x}\left(\frac{g_s V_m}{V_{CV}}\right) + \rho L\frac{\partial}{\partial t}\left(\frac{g_s V_m}{V_{CV}}\right) \tag{3.3}$$

Note that r is the radial coordinate and x is the axial coordinate (figure 3.1). The term on the left hand side of this equation represents the rate of change of sensible heat per unit volume. The first and second terms on the right hand side represent the conductive rate of heat flow per unit volume in the radial and axial directions respectively. The third term is the advective rate of sensible heat flow per unit volume. The fourth and fifth terms account for the latent heat due respectively to the advection of material with varying solid fraction and to the solidification of the alloy.

Equation 3.3 is a Eulerian formulation of the heat transfer equation for a moving sample *i.e.*, its solution gives the temperature field in a fixed domain where the sample-crucible system translates. The total computational Eulerian domain is shown in figure 3.1. The overall domain is further subdivided into two adjacent sub-domains corresponding to the TiAl sample (light grey) and the Y_2O_3 crucible (dark grey).

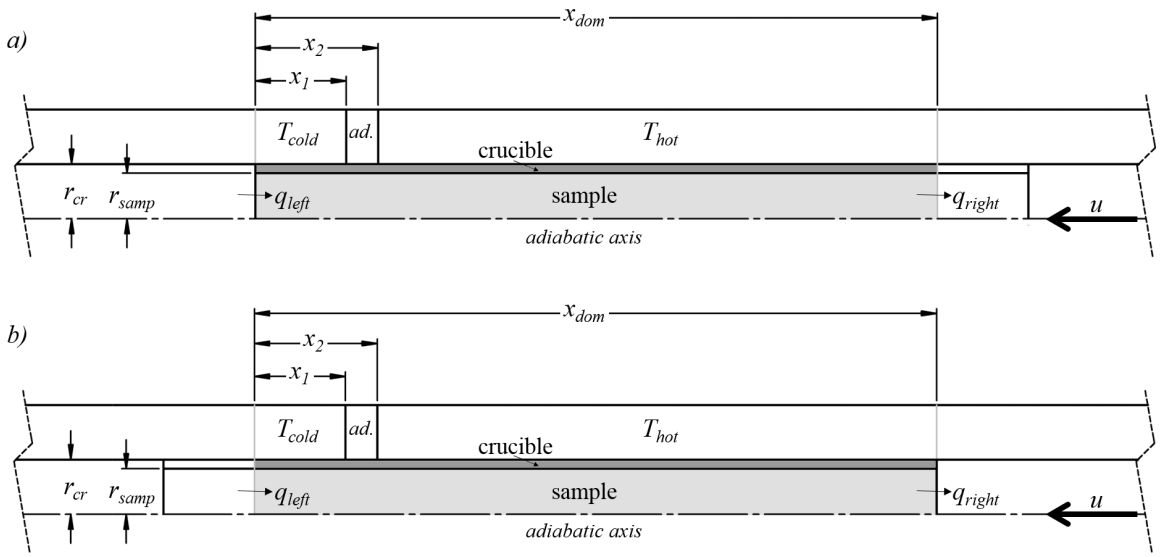

FIGURE 3.1: Computational domain for simulations in grey. a) Beginning of pulling stage. b) End of pulling stage.

For the solution of equation 3.3 a finite volume numerical model was implemented. The two adjacent computational domains representing the sample and the crucible were discretized into annular control volumes of length Δx and thickness Δr, as depicted in figure 3.2.

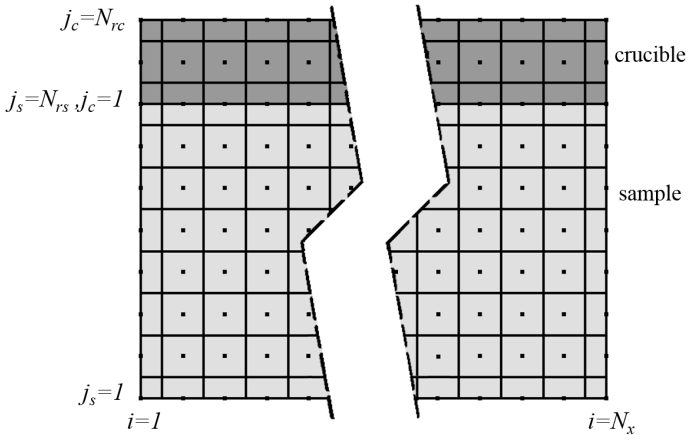

FIGURE 3.2: Discretization grid of computational domain.

The general description and derivation of a similar FV model is reported in the literature [20]. From this procedure, the following discretized equation was obtained:

$$
\begin{aligned}
T_{i,j}^{new} = T_{i,j} + \frac{\Delta t}{\rho c_{p_{i,j}}} \Bigg\{ & \frac{1}{V_{CV_{i,j}}} \left[\left(A_{s_{i,j}} q_{s_{i,j}} + A_{n_{i,j}} q_{n_{i,j}} \right) + \left(A_{w_{i,j}} q_{w_{i,j}} + A_{e_{i,j}} q_{e_{i,j}} \right) \right] \\
& - u\rho \frac{\left(c_{p_{e_{i,j}}} T_{e_{i,j}} - c_{p_{w_{i,j}}} T_{w_{i,j}} \right)}{\Delta x} + u\rho L \frac{V_{m_{i,j}}}{V_{CV_{i,j}}} \frac{\left(g_{s_{e_{i,j}}} - g_{s_{w_{i,j}}} \right)}{\Delta x} + u\rho L \frac{g_{s_{i,j}}}{V_{CV_{i,j}}} \frac{\left(V_{m_{e_{i,j}}} - V_{m_{w_{i,j}}} \right)}{\Delta x} \\
& + \rho L \frac{V_{m_{i,j}}}{V_{CV_{i,j}}} \frac{\left(g_{s_{i,j}}^{new} - g_{s_{i,j}} \right)}{\Delta t} + \rho L \frac{g_{s_{i,j}}}{V_{CV_{i,j}}} \frac{\left(V_{m_{i,j}}^{new} - V_{m_{i,j}} \right)}{\Delta t} \Bigg\}
\end{aligned}
\tag{3.4}
$$

where $A_{i,j}$ are the areas of the faces of the i,j-th control volume and $q_{i,j}$ are the entering heat fluxes at each face of the i,j-th control volume [20]. Note that the last four terms in equation 3.4 result from the decomposition of the derivatives in the last two terms of equation 3.3.

The explicit time scheme expressed by equation 3.4 is coupled to a Newton-Raphson iterative scheme for the calculation of g_s^{new} and to a front tracking algorithm for determining V_m and V_m^{new}.

Equation 3.4 is valid in a general CV where a mixture of solid and liquid phases are present. In fully liquid and fully solid CVs, including the crucible region, the last four terms of equation 3.4 must not be considered.

3.2.2 Solidification model

In order to solve equation 3.4, it is necessary to model the evolution of the mushy zone in the sample during solidification to calculate the values of V_m and g_s at any time step during the process.

As described in section 3.1, two different dendritic structures may develop during alloys solidification, *i.e.*, columnar or equiaxed grains. In the present study, only columnar grain growth is directly modelled, by the means of a front tracking algorithm. According to this procedure, the volume of columnar mush is delimited at the liquid side by a front that envelopes the columnar grains tips.

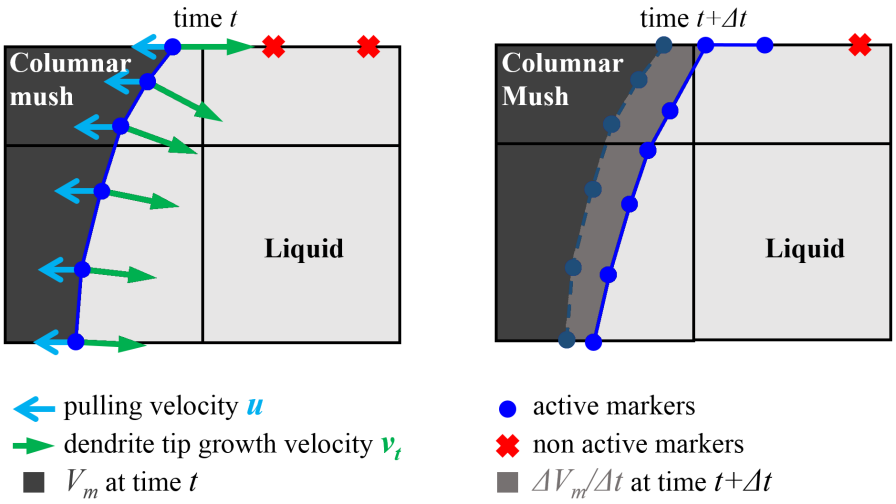

FIGURE 3.3: Front tracking model.

Figure 3.3 shows the front, identified by a series of markers connected by linear segments, at two consecutive time steps. Also, in the liquid non active markers are positioned on each physical border of the sample, and are activated if a given nucleation undercooling ΔT_{nucl} is reached. This allows the modelling nucleation and growth of radial columnar grains from the sample circumference and axial columnar grains from the right end of the sample.

The velocity at which each active marker, and hence the front, advances during the process is calculated as the sum of two components which represent the contribution of the solidification process and of the sample translation. The first component, $\boldsymbol{v}_t$, is normal to the front and directed towards the liquid, and its magnitude is calculated according to the following dendrite tip kinetic law [26]:

$$|\boldsymbol{v}_t| = C\Delta T_t^b \tag{3.5}$$

where ΔT_t is the undercooling at each marker position, *i.e.*, the difference between the equilibrium liquidus temperature of the alloy and the temperature at the marker position. The latter is calculated by bilinear interpolation from the temperatures of the four CVs closest to the marker. C and b are the dendrite growth coefficient and the undercooling exponent, respectively.
For the alloy under consideration, the dendrite growth coefficient and undercooling exponent for the evaluation of equation 3.5 are equal to $C = 2.63 \cdot 10^{-6}$ m/s·°C^{-b} and $b = 2.79$, respectively [15].

The second component is equal to the axial pulling velocity, $\boldsymbol{u}$, and is the same for each marker.

After the markers displacement, the new markers positions are checked to avoid marker rarefaction or accumulation, and the new front is determined. The marker spacing is determined in order to maintain the resolution of the grid spacing, therefore the distance between two markers could not be greater than the chosen Δx, nor smaller than $0.5\Delta x$.

Knowing the position of the front in the domain permits one to calculate, at each time step, the volume of mush V_m in each CV containing the front. This value, V_m, is the captured mushy volume.

Finally, a further relation must be included to calculate the value of solid fraction, g_s, in the mushy zone as a function of temperature. For this purpose, a solid fraction-temperature relationship for the TiAl intermetallic alloy of interest was estimated by Mooney et al. [15], and is shown in figure 3.4.

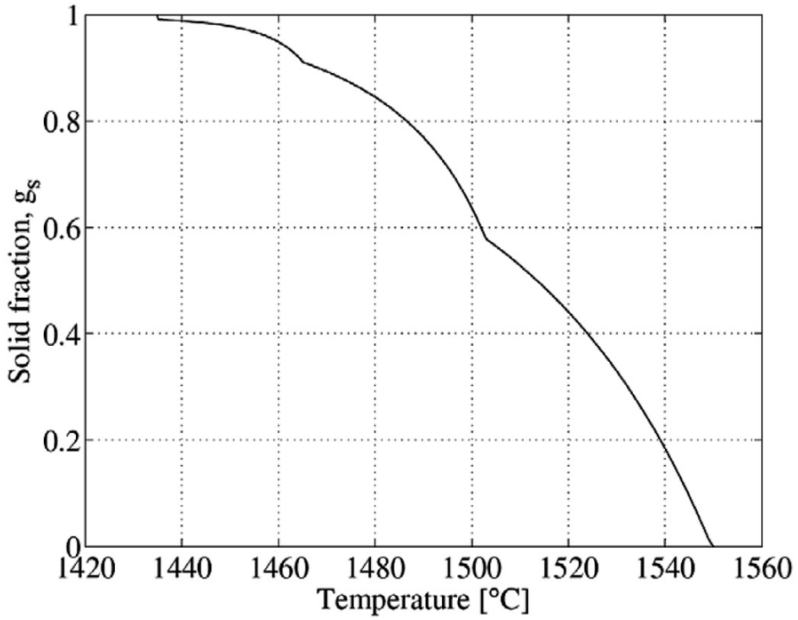

FIGURE 3.4: Solid fraction to temperature relationship for Ti-44.5Al-4.5Nb-0.2C-0.2B estimated using Thermocalc via the "Modified Scheil Module" [15].

3.2.3 CET prediction

The nucleation and growth of equiaxed grains in the undercooled liquid ahead the columnar region, and hence CET, were not modelled directly. In order to assess the potential of a CET occurrence, two indirect methods were employed.

The first approach consisted in the evaluation, at each time step, of the equiaxed index, according to Browne [21]:

$$I_{eq} = \sum_{i,j}^{N_{CV_s}} U_{b_{i,j}} V_{CV_{i,j}} \tag{3.6}$$

where $U_{b_{i,j}}$ is the undercooling in the i,j-th control volume:

$$U_{b_{i,j}} = \begin{cases} T_L - T_{i,j} & \text{if } T_{i,j} \leq T_L \text{ and } \frac{V_{m_{i,j}}}{V_{CV_{i,j}}} < 0.5 \\ 0 & \text{elsewhere} \end{cases} \tag{3.7}$$

The equiaxed index rises during the solidification process as the temperature in the sample is lowered and the volume of undercooled liquid and level of undercooling increase. The parameter reaches a maximum after which it quickly drops as the undercooled liquid is consumed by the columnar mush. As I_{eq} increases, CET becomes more probable, and the peak reached by I_{eq} during the process corresponds to the instant at which the transition is most likely to occur. Therefore, the peak value for I_{eq} highlights the moment when conditions for CET formation within the sample are at their optimum level. Equiaxed index is a useful comparison tool for predicting the likelihood of CET between experiments with different process conditions. However, when used on its own or without knowledge of a threshold value, equiaxed index provides insufficient evidence to determine whether a CET could take place.

To overcome this issue, Hunt's method [23] is used in conjunction with the equiaxed index. According to Hunt, the critical temperature gradient condition for fully equiaxed growth is:

$$G < 0.617 \cdot N_0^{1/3} \left[1 - \left(\frac{\Delta T_{nucl}}{\Delta T_t}\right)^3\right] \Delta T_t = G_{CET} \tag{3.8}$$

where G is the temperature gradient at the columnar front location, N_0 is the nuclei density, ΔT_t is the undercooling at the columnar front location and ΔT_{nucl} is the nucleation undercooling of the equiaxed grains.

Hunt's model is formulated for 1D directional steady state solidification. Since the axisymmetric model proposed is 2D, Hunt's analysis is performed at specific marker locations where the local temperature gradient and columnar growth are either fully axial or fully radial. This allows a qualitative evaluation of the possibility of CET occurrence at different locations at each time step of the solidification process.

3.2.4 Boundary conditions

Given the axisymmetric nature of the problem, on the x axis an adiabatic boundary condition is assumed.

At each end of the two sub-domains, *i.e.*, at $x = 0$ and $x = x_{dom}$, Neumann boundary conditions are imposed such that:

$$\begin{cases} q_{left} = -k\frac{\partial T}{\partial x}|_{x=0} & \text{for } \; x = 0, \; 0 \leq r \leq r_{cr} \\ \\ q_{right} = -k\frac{\partial T}{\partial x}|_{x=x_{dom}} & \text{for } \; x = x_{dom}, \; 0 \leq r \leq r_{cr} \end{cases} \tag{3.9}$$

As shown in figure 3.5, at the common nodes st the interface between the sample and the crucible domains, the temperature difference between the two materials is modelled by considering a thermal contact resistance [27], hence:

$$-k\frac{\partial T}{\partial r} = \frac{1}{R_{int}}\left(T_{samp} - T_{cr}\right) \quad \text{for} \quad 0 \leq x \leq x_{dom},\ r = r_{samp} \tag{3.10}$$

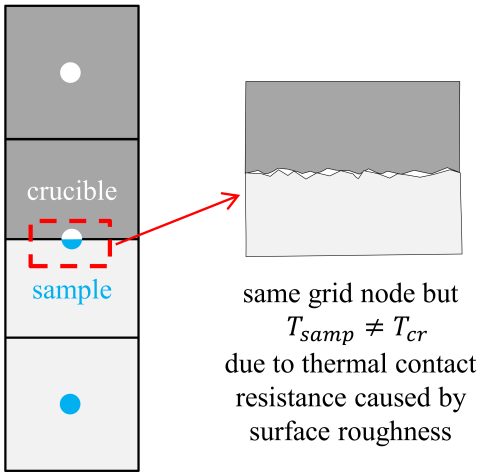

FIGURE 3.5: Thermal contact resistance between sample and crucible

To model the radial heat flow at the crucible external circumference, the following boundary conditions are applied along the heater and the heat sink:

$$-k\frac{\partial T}{\partial r} = \begin{cases} h_{cold}\left(T - T_{cold}\right) & \text{for} \quad 0 \leq x < x_1,\ r = r_{cr} \\ h_{hot}\left(T - T_{hot}\right) & \text{for} \quad x_2 < x \leq x_{dom},\ r = r_{cr} \end{cases} \tag{3.11}$$

Note that to model the power down solidification process, T_{hot} is a function of time, T_{hot}^0 being its initial value. The heat transfer coefficients include both the effect of convective and radiative heat transfer.

Finally, at the interface with the adiabatic baffle the radial heat flux is set to zero so that:

$$\frac{\partial T}{\partial r} = 0 \quad \text{for} \quad x_1 \leq x \leq x_2,\ r = r_{cr} \tag{3.12}$$

3.2.5 Input data

Table 3.1 shows the main thermophysical properties of the crucible and the sample material, taken from refs. [28] and [29]. In particular, the specific heat and thermal conductivity are modelled as polynomial functions of temperature, $P = a_0 + a_1 T + a_2 T^2 + a_3 T^3$. For the alloy, the properties in the mushy zone are given by a linear combination of the solid fraction as follows:

$$P_m = \left(1 - \frac{g_s V_m}{V_{CV}}\right) P_l + \frac{g_s V_m}{V_{CV}} P_s \tag{3.13}$$

The heterogeneous nucleation undercooling of the columnar grains at the crucible surface is ΔT_{nucl} =1 °C.

Finally, the geometrical data used in the simulations are reported in table 3.2.

TABLE 3.1: Thermophysical properties of Ti-45.5Al-4.7Nb-0.2C-0.2B and Y_2O_3 used in the simulations.

		Ti-45.5Al-4.7Nb-0.2C-0.2B	Y_2O_3
T_L / [°C]		1550	
T_S / [°C]		1434	
ρ / [kg/m^3]		3674	5000
ρL / [J/m^3]		$1249 \cdot 10^6$	
c_p / [J/(kg°C)]	sol.	$6.32 \cdot 10^2 + 7.44 \cdot 10^{-2} T - 2.07 \cdot 10^{-4} T^2 + 2.97 \cdot 10^{-7} T^3$	$0.44 \cdot 10^3 + 0.14 T$
	liq.	1040	
α / [m^2/s]		$5.36 \cdot 10^{-6} + 5.18 \cdot 10^{-9} T + 4.3 \cdot 10^{-13} T^2 - 3.01 \cdot 10^{-15} T^3$	
k / [W/(m°C)]		$\alpha \cdot \rho c_p$	$21.31 - 0.02 T + 5.83 \cdot 10^{-6} T^2$

TABLE 3.2: Geometrical data used in the simulations.

x_{dom} / [m]	x_1 / [m]	x_2 / [m]	r_{samp} / [m]	r_{cr} / [m]
$150{\cdot}10^{-3}$	$20{\cdot}10^{-3}$	$27{\cdot}10^{-3}$	$5{\cdot}10^{-3}$	$7.5{\cdot}10^{-3}$

3.2.6 Simulation setups

The simulation setups described in the following sections are aligned to two different experimental scenarios from the literature [15, 16]. Two operation modes are considered, namely, stationary operation and Bridgman combined with power-down operation. Stationary operation was performed experimentally in order to characterise the heat transfer performance (and boundary conditions) of the furnace. In this case the sample was held under steady conditions while temperature measurements were recorded [15] . Combined Bridgman with power-down operation was performed experimentally where the Bridgman (or pulling) mode was used to initiate columnar growth and was then switched to a power-down (stationary with controlled cooling) mode. This combined mode of operation was designed to generate suitable conditions for CET [16].

Stationary solidification

As a first step, the model is used to simulate a series of experiments carried out in stationary conditions. During these experiments, the temperatures of the crystallizer and of the heater are kept constant and the pulling velocity is set equal to zero. This analysis is used to test the efficacy of the model in reproducing realistic solutions. Hence the numerical results are compared to the measured temperature profiles along the axis of the samples. The main input data for these simulations are reported in table 3.3.

TABLE 3.3: Input data for stationary simulations.

	Simulation run			
	S1	S2	S3	S4
T_{cold} / [°C]	17			
T_{hot} / [°C]	1600	1630	1650	1680
R_{int} / [(m^2°C)/W]	$1{\cdot}10^{-5}$			
$\partial T/\partial x\|_{x=0}$ / [°C/m]	$7.5{\cdot}10^{3}$			
$\partial T/\partial x\|_{x=x_{dom}}$ / [°C/m]	0			
h_{cold} / [W/(m^2°C)]	70			
h_{hot} / [W/(m^2°C)]	200			

Combined Bridgman and power-down simulation

The numerical model is set up for the simulation of combined Bridgman and power down experiments. Starting from an initial steady state condition, the sample is first pulled 20 mm towards the crystallizer (pulling stage). Following this, the temperature of the heater is gradually lowered with a constant cooling rate (stationary stage). This procedure is repeated with different cooling rates applied, just as was done in the experiments [16]. The input data for these simulations are shown in table 3.4.

TABLE 3.4: Input data for combined Brigman and power down simulations.

		Simulation run			
		PD1	PD2	PD3	PD4
	T^0_{hot} / [°C]	1720			
Pulling Stage	u / [m/s]	$2.78{\cdot}10^{-4}$			
Cooling Stage	$-\partial T_{hot}/\partial t$ / [°C/min]	15	20	30	50

3.3 Results and discussion

In this section, the results of the stationary (S1 to S4) and combined Bridgman and power down (PD1 to PD4) simulations are reported and compared to experimental data from refs. [15], [14] and [16]. The grid and time steps assumed for all the simulations are Δx=Δr=0.625 mm and Δt=0.001 s, which ensure the stability and convergence of the numerical scheme. Grid and time step independence were investigated. The root mean square deviation of the temperature distributions obtained with Δx=Δr=0.625 mm and Δt=0.001 s, and with Δx=Δr=0.3125 mm and Δt=0.0005 s was of the order of $0.03°C$.

3.3.1 Stationary solidification

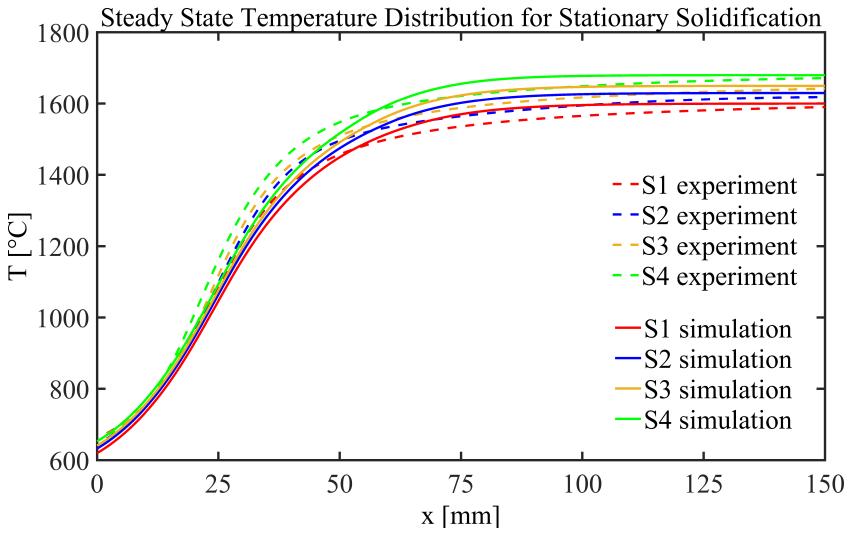

FIGURE 3.6: Comparison of experimental and simulated temperature profiles at the sample axial position.

For the case studies S1, S2, S3 and S4 the sample is stationary and the temperatures of crystallizer and heater are kept constant (table 3.3). The scope of this analysis is to assess the model efficacy in reproducing realistic results.

Figure 3.6 shows the temperature profiles in the sample when a steady state condition is reached. Experimental temperatures, available from Mooney et al. [15], are represented with dashed lines. These temperatures were measured by a thermocouple that was translated along the axis of the sample. The experimental data are compared to the simulated temperatures at the axial CVs, and are represented in figure 3.6 by solid lines.

The simulated results show good agreement with the experiments. Some differences are present, with a root mean square error between the simulated and experimental data of the order of $30°C$. These differences are due to a combination of several factors. For instance,

we assumed constant values for the heat transfer coefficients at the circumference of the crystallizer and heater respectively. The chosen values fall into a realistic range for furnaces with argon atmosphere [30, 31], though real values would vary with both temperature and geometrical, material and surface characteristics of the furnace and crucible interface. An accurate estimate of actual values would require further experimental data and analysis which are beyond the scope of the present study.

Another assumption was made for the values of the axial temperature gradients for the Neumann boundary conditions. In fact, uniform temperature gradients were imposed along the entire radius of the sample and the crucible. In reality, the values would change with the radius and in the different materials, however temperature measurements at different radii were not available.

Nevertheless, acknowledging the modelling assumptions and experimental uncertainties, the model is deemed to be sufficiently accurate to reproduce, in a realistic way, the solidification processes under consideration.

3.3.2 Bridgman and power down solidification

Simulations PD1, PD2, PD3 and PD4 are divided into two steps. First, starting from a steady state condition, the sample is pulled 20 mm into the crystallizer (Bridgman solidification or pulling stage). The first stage is common to all the simulations. Afterwards, four different cooling rates are imposed to each sample (power down or cooling stage). As mentioned, these scenarios replicate the conditions performed in the reported experiments [16].

Since equiaxed grains growth is not directly simulated in the model, a first analysis is presented considering the free evolution of axial and radial columnar grains in the entirety of the samples. Afterwards, the likelihood of CET will be discussed according to the results of the equiaxed index and Hunt models (section 3.2.3).

Figure 3.7 shows the temperature (top half of images) and solid fraction (bottom half of images) distribution in the samples at the initial time and at the end of the pulling stage. The columnar front, composed by markers connected by straight lines, is represented in white. Solid black lines demarcate the sample and the crucible domains.

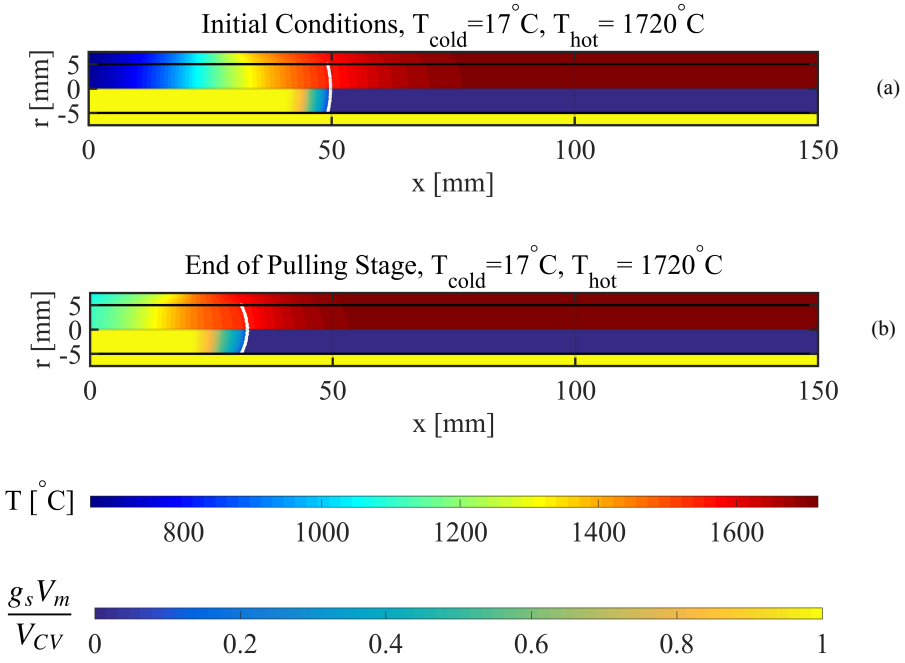

FIGURE 3.7: Temperature (top half of images) and solid fraction (bottom half of images) distributions at the beginning (a) and at the end (b) of the pulling stage.

Initially (figure 3.7(a)), the front is located close to x =50 mm, with the axial marker at x =49.8 mm and the radial marker at x =49.2 mm. The shape of the columnar front is slightly convex, meaning that the radial temperature gradient is positive, hence heat is flowing from the external heater to the center of the sample. The initial condition corresponds to the steady state solution for the initial furnace configuration with a stationary sample, T_{cold} = 17 °C and T_{hot} = 1720 °C. At steady state the columnar front is stationary and at equilibrium, hence its position corresponds to the one of the liquidus isotherm and an undercooled liquid region is not present.

During the pulling stage temperature in the sample increases due to the advection of sensible and latent heat, represented by the third and fourth terms of equation 3.3.

As figure 3.7(b) shows, at the end of the pulling stage the columnar front shifts towards the crystallizer according to the pulling direction. The overall displacement of the front is the effect of two distinct mechanisms: the pulling velocity u and the growth velocity of each marker due to the local undercooling as per equation 3.5. The final position of the axial marker is x =32.5 mm, while the position of the marker at the sample circumference is x =31.2 mm. The front is still located in the heater region, that begins at x_2 =27 mm. At this location, the radial heat flux is positive and the convexity of the front is slightly more pronounced than in the initial conditions. The width of undercooled liquid region is less than 1 mm, with a maximum undercooling of 2 °C.

Following the Bridgman solidification phase, the furnace is switched to power down mode. Cooling rates of 15, 20, 30 and 50 °C/min are imposed during simulations PD1, PD2, PD3 and PD4, respectively.

Figures 3.8, 3.9, 3.10 and 3.11 show the temperature and solid fraction distribution, and the front at different times during PD1, PD2, PD3 and PD4. In the figures, t_{PD} is the time passed since the beginning of the cooling stage.

Figures 3.8(a), 3.9(a), 3.10(a) and 3.11(a) show the sample at t_{PD} =200 s. At this time the front is still convex in all the simulations, meaning that the radial heat flux is positive. The instant corresponding to the radial heat flux reversal is represented in figures 3.8(b), 3.9(b), 3.10(b) and 3.11(b). The front at this time is almost perfectly flat in all the simulations, with a maximum difference between the x coordinate of the axial and outer markers of 0.08 mm.

The radial heat flux reversal is strictly related to the value of the applied cooling rate. In fact, due to the thermal inertia of the sample, its cooling rate is slower than the one applied to the furnace, hence at some point the temperature of the furnace becomes lower than the temperature of the solidifying material. Clearly, this effect is more pronounced for higher cooling rates. This is visible in figures 3.8(b), 3.9(b), 3.10(b) and 3.11(b), showing that proceeding from PD1 to PD4 the radial heat flux reversal occurs earlier in time, when the front is in a less advanced position. The exact times and axial marker positions are reported in table 3.5.

After, the front advances in a region with a negative radial heat flux. Furthermore, the radial thermal gradient is stronger towards the right end of the sample where the difference between the furnace and sample temperatures is higher. This condition is favourable for radial columnar growth, which occurs when the nucleation undercooling is reached at the circumference of the sample.

Figures 3.8(c), 3.9(c), 3.10(c) and 3.11(c) show the samples 100 s after the radial heat flux reversal. In all simulations, the front is evidently concave, and markers are nucleating at the circumference of the sample. Concavity and radial growth are more pronounced at higher cooling rates (PD3 and PD4). Figures 3.8(d), 3.9(d) and 3.10(d) show the solution 150 s after the reversal. At this time, nucleation of all the markers along the length of the sample PD1 is evident. In PD2 and especially PD3 radial growth is quite significant. Finally, figure 3.11(d) shows the sample from PD4 at t_{PD}=344 s, *i.e.*, 131 s after the radial heat flux reversal. At this time all the undercooled liquid is enveloped by the front, which has converged to the axis of the sample.

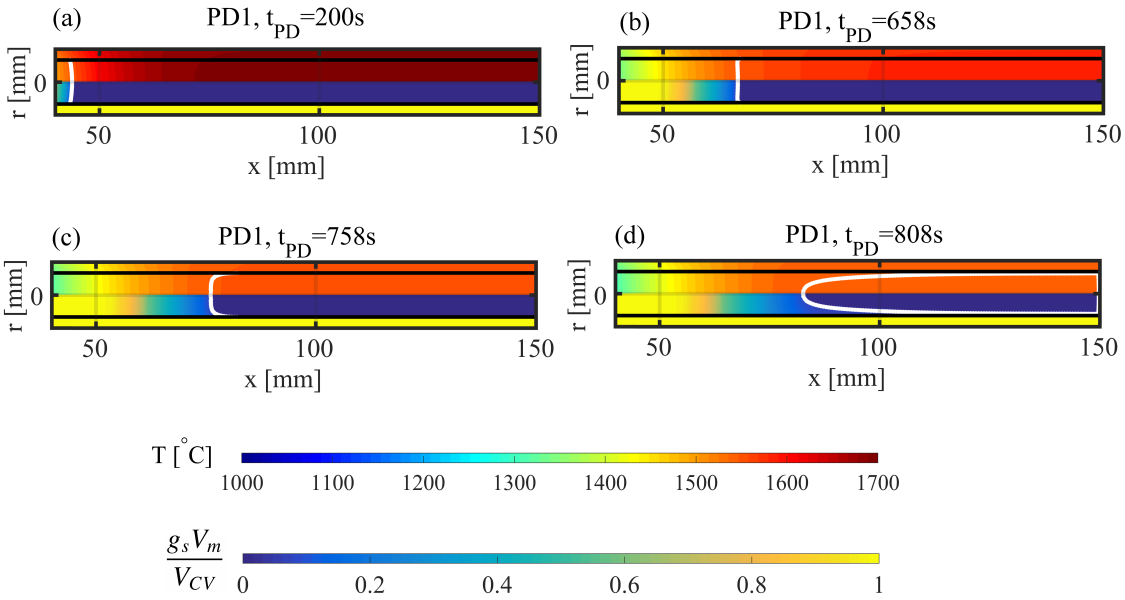

FIGURE 3.8: PD1: temperature, solid fraction and front evolution during the power down solidification process. t_{PD} is the time since the beginning of the cooling stage. (a) t_{PD}=200 s. (b) Radial heat flux reversal time. (c) 100 s after radial heat flux reversal. (d) 150 s after radial heat flux reversal.

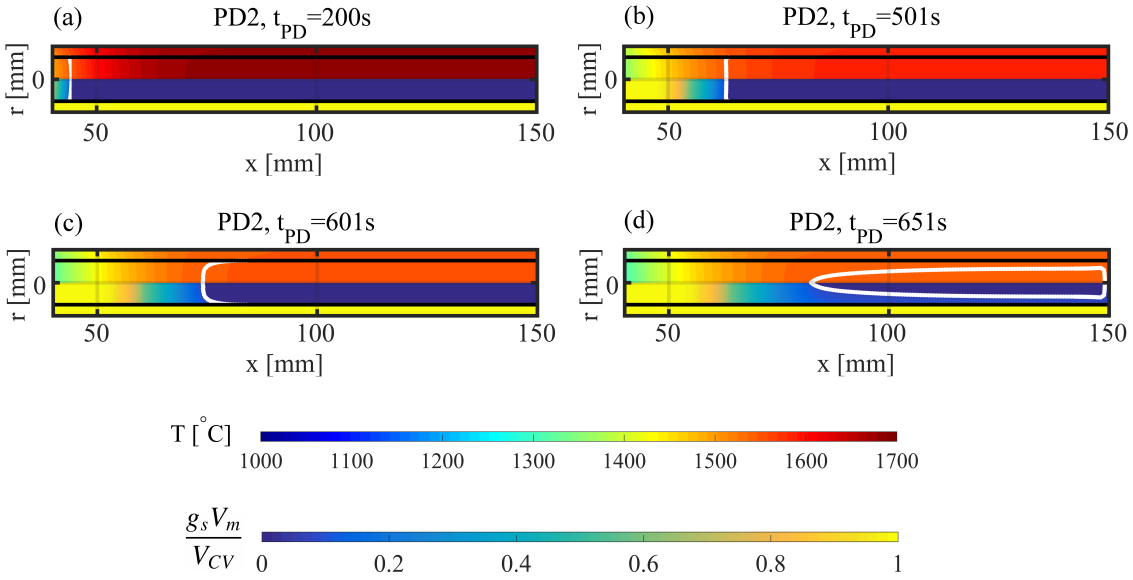

FIGURE 3.9: PD2: temperature, solid fraction and front evolution during the power down solidification process. t_{PD} is the time since the beginning of the cooling stage. (a) t_{PD}=200 s. (b) Radial heat flux reversal time. (c) 100 s after radial heat flux reversal. (d) 150 s after radial heat flux reversal.

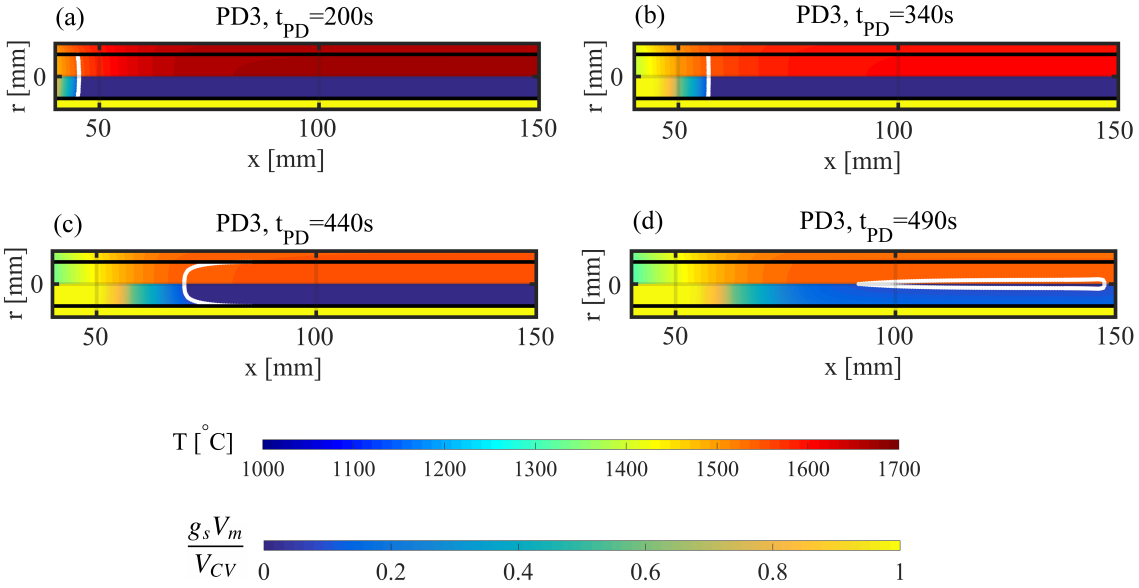

FIGURE 3.10: PD3: temperature, solid fraction and front evolution during the power down solidification process. t_{PD} is the time since the beginning of the cooling stage. (a) t_{PD}=200 s. (b) Radial heat flux reversal time. (c) 100 s after radial heat flux reversal. (d) 150 s after radial heat flux reversal.

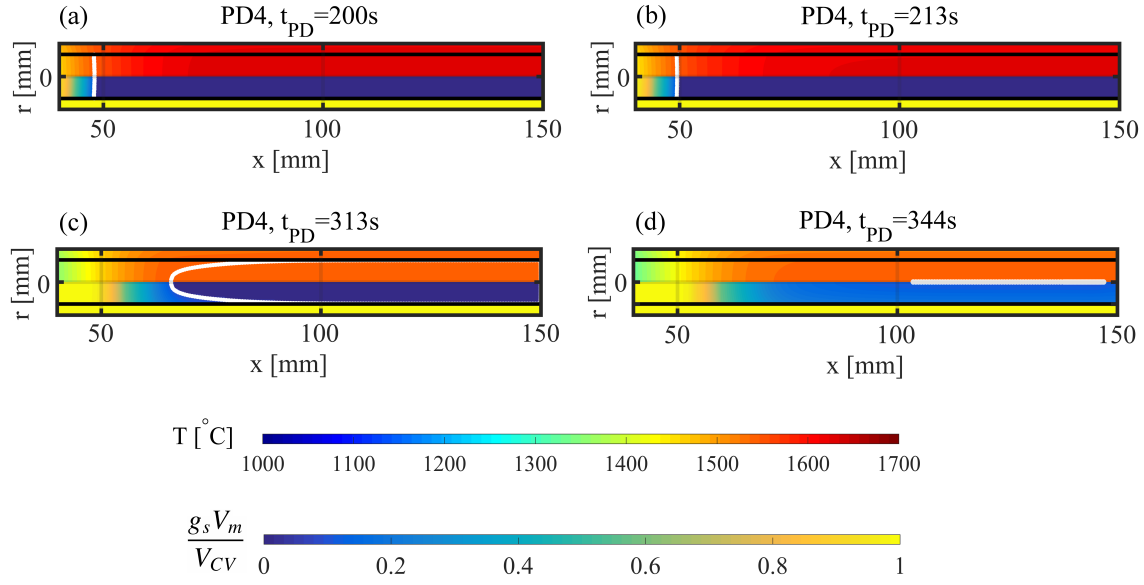

FIGURE 3.11: PD4: temperature, solid fraction and front evolution during the power down solidification process. t_{PD} is the time since the beginning of the cooling stage. (a) t_{PD}=200 s. (b) Radial heat flux reversal time. (c) 100 s after radial heat flux reversal. (d) Time at which all the liquid is enveloped by columnar mush.

TABLE 3.5: Time and axial marker position corresponding to the radial heat flux reversal and to the transition to a fully radial columnar growth.

	Radial heat flux reversal		Transition to fully radial growth	
	t_{PD} / [s]	$x(m_{axis})$ / [m]	t_{PD} / [s]	$x(m_{axis})$ / [m]
PD1	658	$67.0 \cdot 10^{-3}$	~823	$\sim 85 \cdot 10^{-3}$
PD2	501	$63.2 \cdot 10^{-3}$	~649	$\sim 82 \cdot 10^{-3}$
PD3	340	$56.9 \cdot 10^{-3}$	~466	$\sim 75 \cdot 10^{-3}$
PD4	213	$49.5 \cdot 10^{-3}$	~318	$\sim 67 \cdot 10^{-3}$

After the radial heat flux reversal, radial columnar grains start to nucleate and grow, and a region of mixed axial and radial columnar grains develops in the sample. After some time, however, axial columnar growth is obstructed by radial grains and a transition to a fully radial columnar region occurs.

The last two columns of table 3.5 show an estimate of the time and position of the axial marker corresponding to a full transition to radial grains. These results derive from a graphical analysis of the trajectory of the markers during the four solidification processes PD1, PD2, PD3 and PD4, shown in figure 3.12. The red vertical lines in the samples show the position of the radial heat flux reversal. The blue lines are the trajectories formed by the positions of the markers in time. It is evident that before the reversal the marker trajectories are directed from the axis to the circumference of the sample, accordingly to a convex shape of the front. In the proximity of the red line, the trajectory is basically parallel to the axial direction. Almost immediately after the reversal, some markers directed in the radial direction are present in all the samples. Finally, a region where the displacement of the markers is completely radial is observed. The overall process is faster for higher cooling rates. The images do not allow to identify a sharp transition from the axial to the radial columnar zone of the alloy, since the method employed models a unique front that delimits the overall region of columnar mush. Also, the trajectories of the markers are in part affected by the markers rarefaction/accumulation checking algorithm, hence they are not the precise scientific indication of the solidification process of the alloy. Nevertheless, the marker displacement depends mainly on the local temperature gradient, therefore their trajectories are useful in giving a rough estimate of the direction of the columnar grains in the different regions.

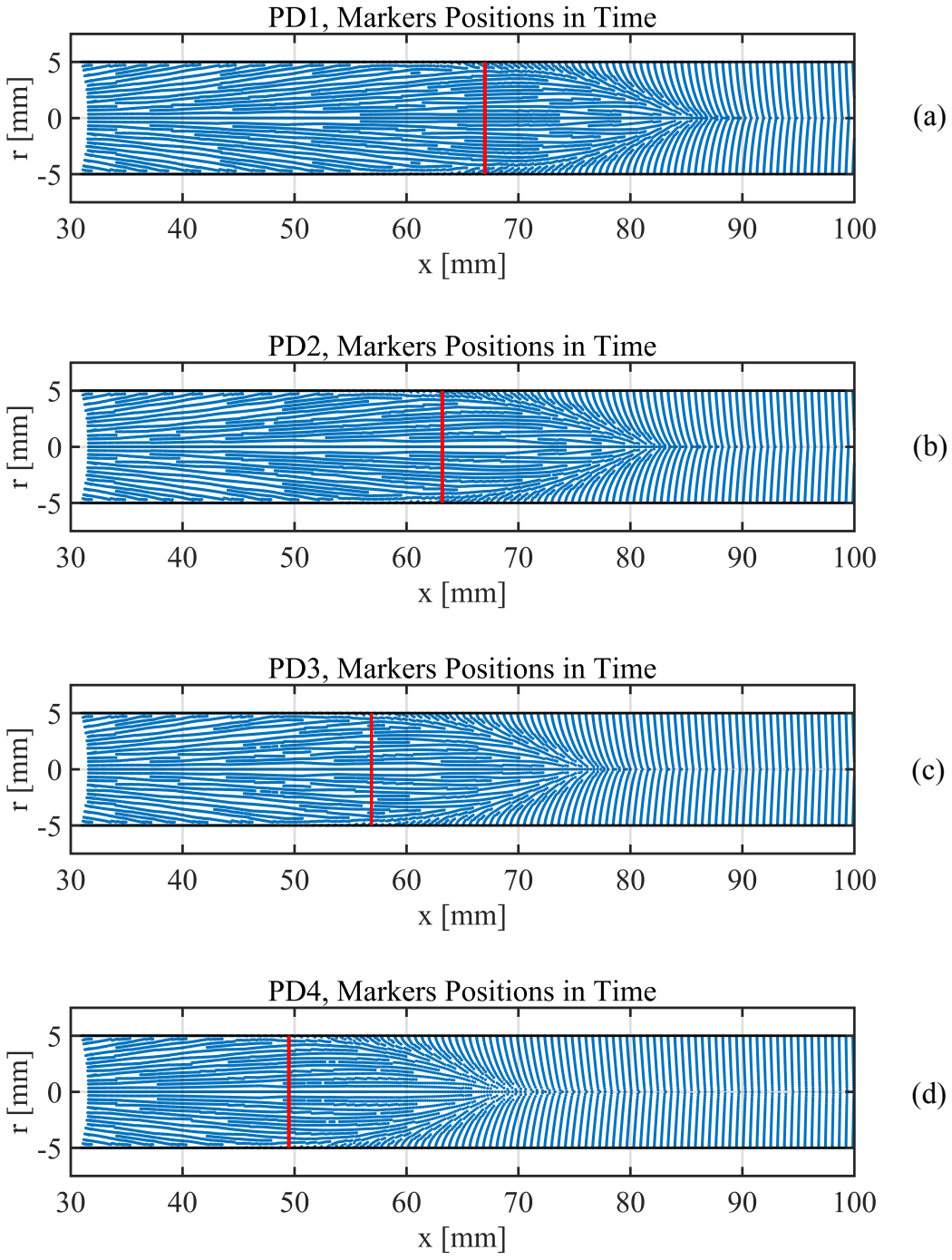

FIGURE 3.12: Marker trajectories during the power down solidification process.

CET prediction

The previous analysis does not consider the possible nucleation and growth of axial grains in the samples, since only columnar growth is directly modelled. Hence, the likelihood of CET is investigated indirectly by the means of the equiaxed index by Browne [22] and Hunt

analysis [23].

Figure 3.13 shows the equiaxed index (equation 3.6) for each of the four simulations from the beginning of the pulling stage ($t_{PD} \sim -72$ s) to the end of each simulation, that corresponds to the instant at which all the undercooled liquid is enveloped by the columnar front. Table 3.6 reports the exact time and axial marker position corresponding to the peak of I_{eq}, and figure 3.14 shows the level of undercooling in the samples at this time. The maximum of I_{eq} represents the instant at which CET is most likely. Nontheless, CET could develop also before the maximum of I_{eq}.

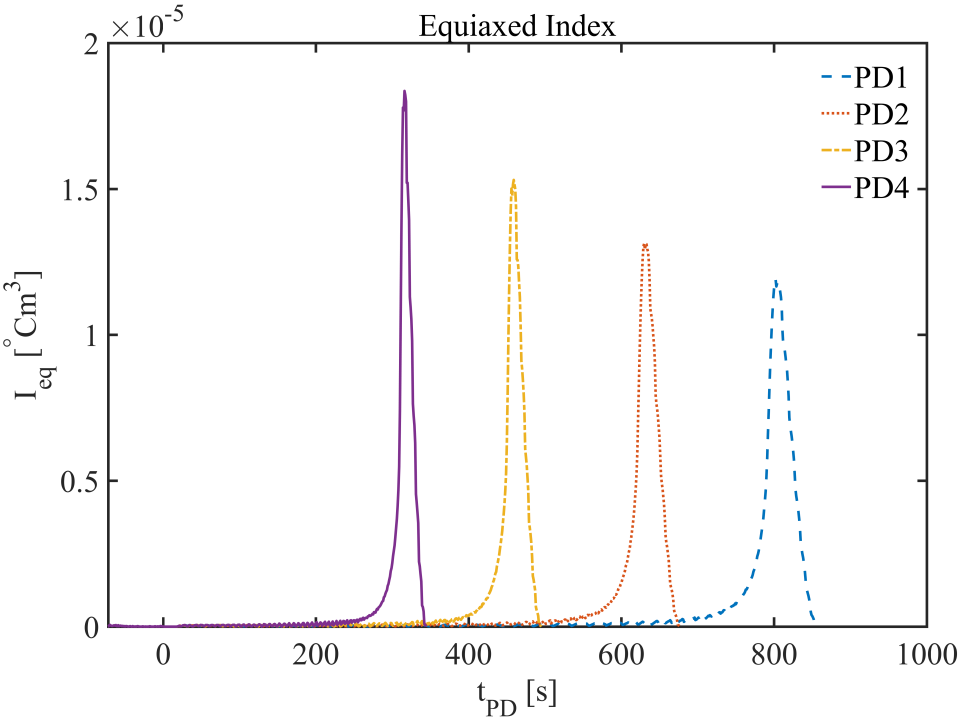

FIGURE 3.13: Equiaxed index for PD1, PD2, PD3 and PD4.

By comparing the times in table 3.6 with the times in table 3.5, it can be noticed that the maximum of I_{eq} occurs after the radial heat flux reversal. Therefore it is probable that, if CET occurs, a region of mixed axial and radial columnar grains would be present before the equiaxed region. Interestingly, in all the simulations the maximum of I_{eq} precedes, just by a few seconds, the time at which a fully radial columnar growth was estimated. This can be explained by the fact that after radial grains start to grow along the entire length of the sample, they quickly consume all the undercooled liquid. With the decrease in the volume of undercooled liquid I_{eq} drops quickly, indicating that equiaxed growth is less probable.

TABLE 3.6: Time and axial marker position corresponding to the maximum of I_{eq}.

	Maximum of I_{eq}			
	PD1	PD2	PD3	PD4
t_{PD} / [s]	802	630	459	316
$x(m_{axis})$ / [m]	$81.7{\cdot}10^{-3}$	$78.4{\cdot}10^{-3}$	$73.5{\cdot}10^{-3}$	$66.7{\cdot}10^{-3}$

Observing the trend of I_{eq} for each of the simulations, it could seem that CET is more likely during PD4, since the peak of the index is higher than for the other simulations. This is due to the fact that at higher cooling rates all the liquid ahead of the front becomes undercooled earlier, *i.e.*, when the front is in a less advanced position. Hence, the volume of undercooled liquid is larger at higher cooling rates. Nevertheless, it must be noticed that at lower cooling rates, like in the case of PD1, the variation of I_{eq} is much slower, meaning that there would be a longer time for equiaxed grains to nucleate and grow.

The equiaxed index I_{eq} gives an indication of the time within which CET is most likely to develop during each of the simulations PD1, PD2, PD3 and PD4. However, it is not sufficient to establish whether and exactly when CET would actually occur in any of the four samples. For this reason an additional analysis was performed using Hunt's model [23]. The results of this study are shown in figures 3.15, 3.16 and in tables 3.7, 3.8.

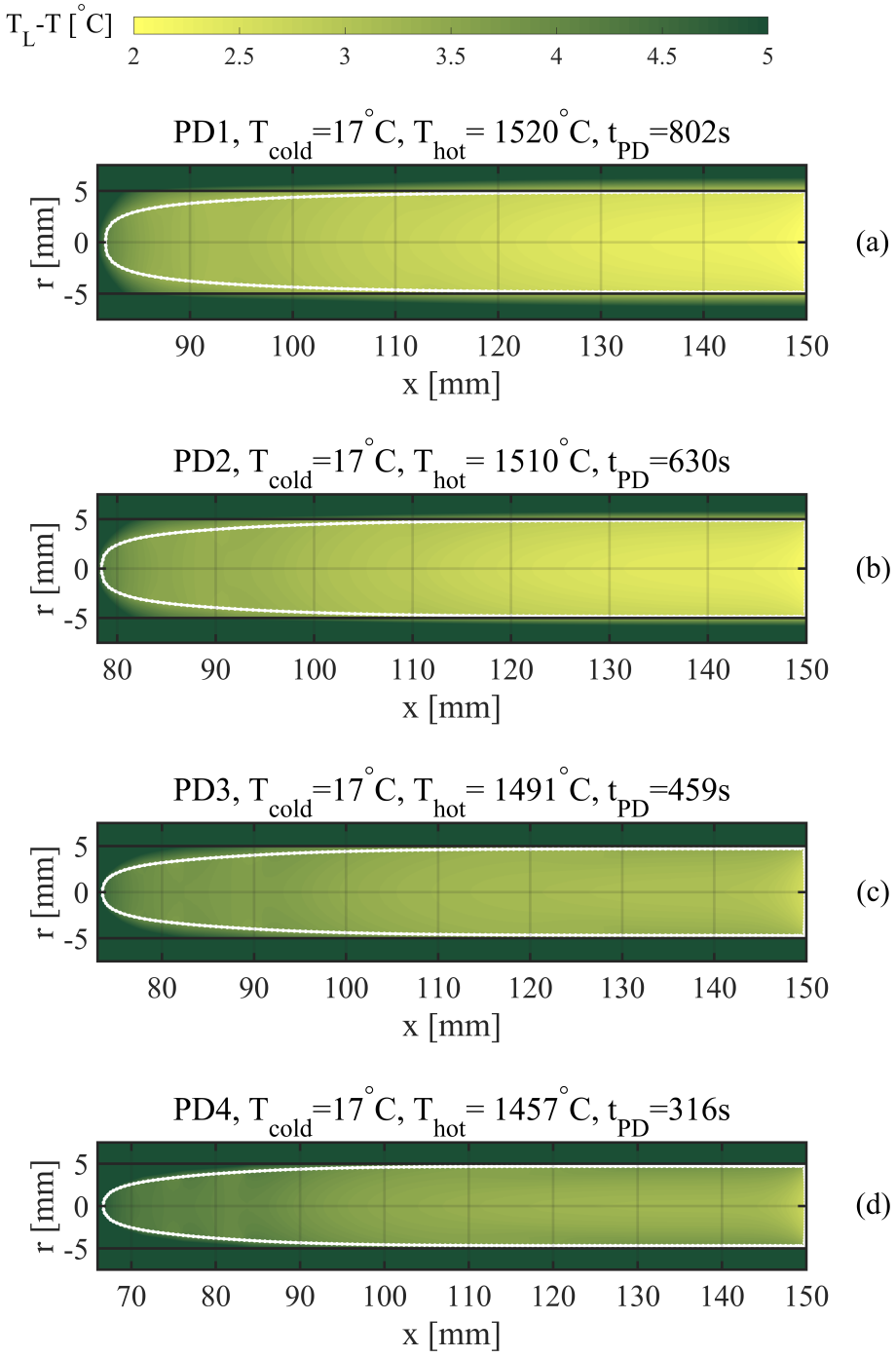

FIGURE 3.14: Level of undercooling at the time corresponding to the maximum of I_{eq}.

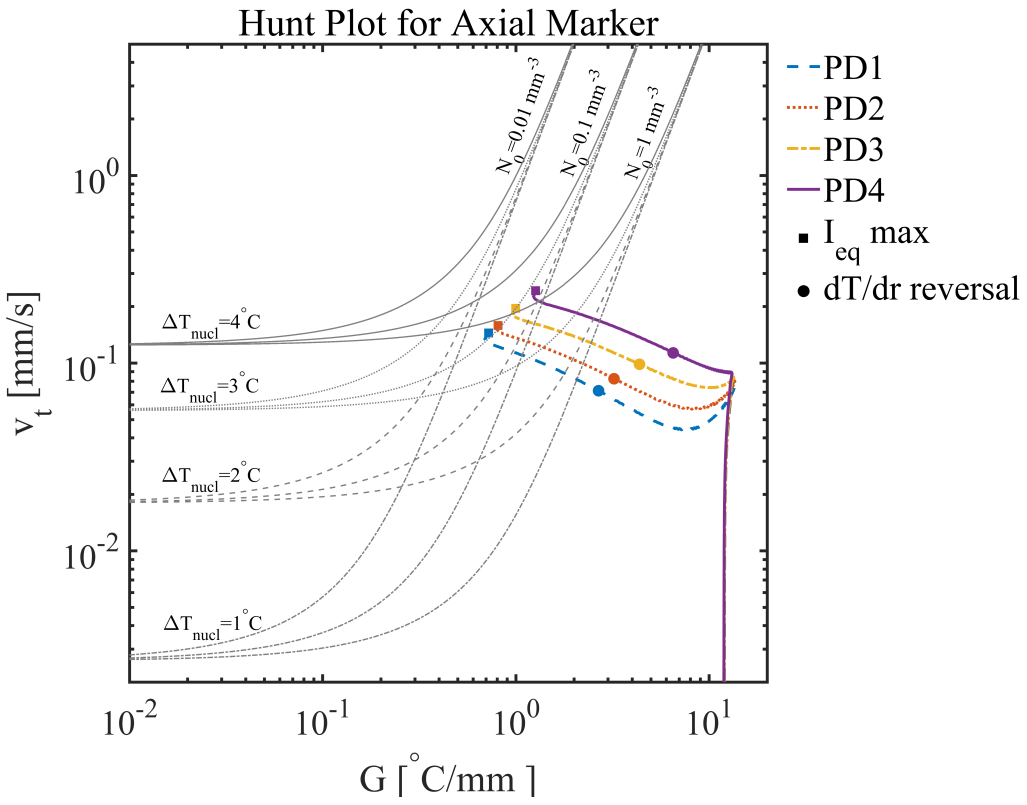

FIGURE 3.15: Hunt plot showing the advancement velocity of the axial marker versus the axial temperature gradient at its location.

Figure 3.15 is referred to as a Hunt plot and represents, on a logarithmic scale, the tip velocity of the columnar front versus the local temperature gradient. The gray curves were calculated with equation 3.8, where the tip velocity and tip undercooling were related by the equation $|\boldsymbol{v}_t| = C\Delta T_t^b$. These lines divide the plot into two regions. In particular, Hunt's model predicts fully equiaxed growth above these curves. On the other hand, the coloured curves in figure 3.15 represent the velocity of the axial marker versus the local axial temperature gradient at every time step during the simulations. CET in the samples is predicted when each of these lines crosses the ones given by Hunt's model.

Several possible values for the nuclei density N_0 and equiaxed grain nucleation undercooling ΔT_{nucl} were investigated. In particular, the maximum undercooling measured in the samples was of the order of 4°C (see figure 3.14). For this reason, nucleation undercooling levels up to this value were considered. Also, it is assumed that the undercooling required for equiaxed nucleation is at least equal to the one required for columnar grains, *i.e.*, 1°C.

TABLE 3.7: Time and position of the axial marker corresponding to CET as predicted by Hunt model for different nuclei densities and equiaxed nucleation undercooling values.

		ΔT_{nucl}=1°C		ΔT_{nucl}=2°C		ΔT_{nucl}=3°C		ΔT_{nucl}=4°C
N_0 / [mm^{-3}]		0.1	1	0.1	1	0.1	1	1
t_{PD} / [s]	PD1	752	692	761	713	793	748	/
	PD2	593	543	598	556	624	581	/
	PD3	432	395	436	402	462	418	456
	PD4	305	275	308	279	/	287	306
$x(m_{axis})$ / [mm]	PD1	75.4	69.1	76.5	71.5	80.5	75.0	/
	PD2	72.9	67.1	73.6	68.5	77.4	71.4	/
	PD3	68.7	63.1	69.3	64.1	74.1	66.4	72.9
	PD4	64.2	58.2	64.8	58.9	/	60.4	64.4

Since non-inoculated samples are considered, only nuclei densities up to 1 mm^{-3} were investigated. Clearly, for combinations with lower nucleation undercoolings and higher nuclei densities, CET in the samples would occur earlier. Also, figure 3.15 shows that at low tip velocity and temperature gradients the nucleation undercooling is the main factor that should be considered for the determination of CET. On the contrary, at higher tip velocities and temperature gradients, the nuclei density is more important.

Table 3.7 reports, for all the simulations, the time and position of the axial marker corresponding to CET according to Hunt's model for all the different combinations of N_0 and ΔT_{nucl}. When N_0=0.01 mm^{-3} the experimental curves in figure 3.15 never cross the ones calculated with Hunt's model, therefore it is assumed that higher values of nuclei densities are required in order to achieve CET. Similarly, except for PD3 and PD4, a nucleation undercooling lower than 4°C is required. Interestingly, in all PD1, PD2, PD3 and PD4 the earliest CET, predicted when N_0=1 mm^{-3} and ΔT_{nucl}=1°C, occurs after the radial heat flux reversal, hence when some radial nucleation and growth is already present. Moreover, when the same values of N_0 and ΔT_{nucl} are considered, the length of the axial columnar region up to CET diminishes with the increase of cooling rate, from PD1 to PD4.

Given the 1 dimensional nature of Hunt's model, the previous analysis is valid for the region of the sample immediately ahead the axial marker, where the temperature gradient is mostly axial. However, in the rightmost part of the sample columnar growth is radial as well as the temperature gradient. Also, undercooling is lower than in the immediate region in

front of the axial columnar grains. These different conditions could lead to different situations than the classical CET from axial columnar grains to a fully equiaxed region. For example, radial columnar grains could continue to grow after CET in front of the axial columnar grains has occurred, resulting in a sample with an equiaxed region between an axial columnar zone and a radial columnar one.

Therefore, the conditions in the region of radial growth were investigated in an analogous way to the one presented for the axial marker. In particular, the growth velocity of a marker located at x =120 mm versus the radial temperature gradient at this location was compared to Hunt's conditions for CET. Results are reported in figure 3.16 and table 3.8.

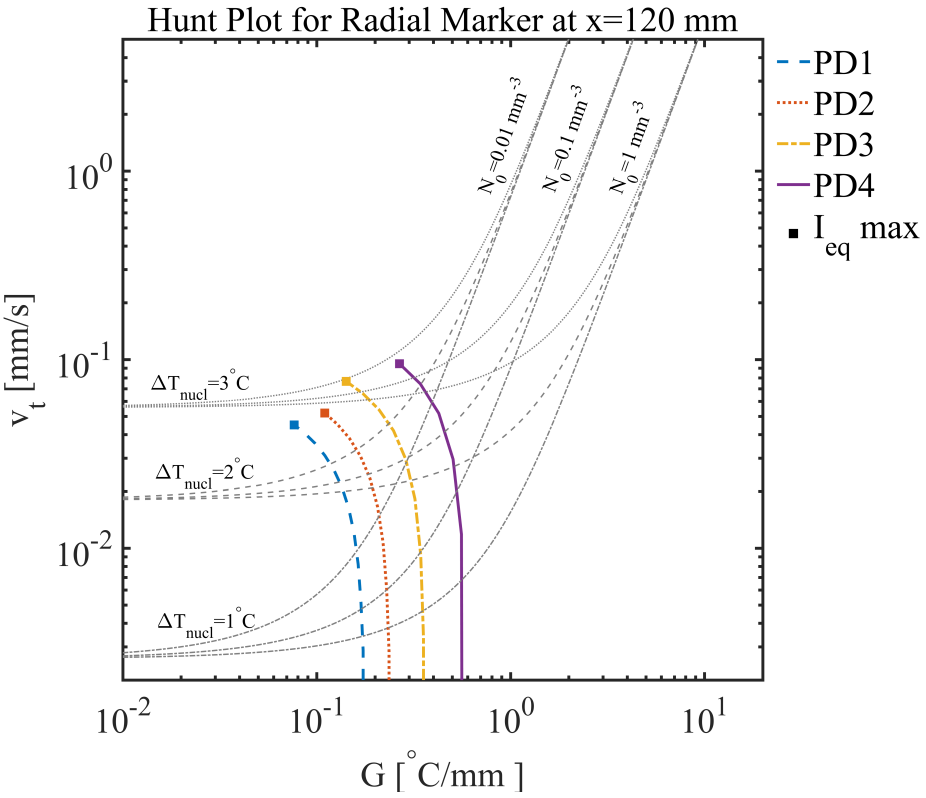

FIGURE 3.16: Hunt plot showing the advancement velocity of the radial marker at x=120 mm versus the radial temperature gradient at its location.

TABLE 3.8: Time corresponding to CET in the radial columnar zone (x=120 mm) as predicted by Hunt model for different nuclei densities and equiaxed nucleation undercooling values.

		ΔT_{nucl}=1°C			ΔT_{nucl}=2°C			ΔT_{nucl}=3°C	
N_0 / [mm^{-3}]		0.01	0.1	1	0.01	0.1	1	0.1	1
t_{PD} / [s]	PD1	794.5	793	792	798.4	797.3	796.8	/	/
	PD2	624.6	623	622	627.3	626.1	625.5	/	/
	PD3	453.5	452	451.2	455.3	454	453.5	457.1	456.6
	PD4	313.4	311.4	310.5	314	312.5	311.8	314.4	313.7

From the comparison between table 3.7 and table 3.8, it emerges that, in most of the cases, CET in the rightmost part of the sample occurs after the one in front of the axial columnar region. This means that some amount of radial grains could still be present in the samples at the end of the process. Interestingly, in some cases (*e.g.*, PD1 and PD2 with ΔT_{nucl}=3°C), CET is predicted only in front of the axial columnar region, meaning that a fully radial columnar zone could be present at the right of the equiaxed region. On the contrary, for different values (*e.g.*, when N_0=0.01 mm^{-3}), CET is predicted only in the region of radial heat flux, meaning that the final structure of the sample could show a transition from axial columnar to radial columnar to equiaxed grains.

In conclusion, the results give an approximate indication of the grain structures that could develop in the samples, showing that it highly depends on the combination of several factors. In particular, radial growth depends on the cooling rate applied to the furnace. In order to avoid it, much lower cooling rates should be used to maintain a positive radial temperature gradient in the samples. On the other hand, CET strictly depends on the equiaxed nuclei density and their nucleation undercooling. In general, in front of the columnar zone axial temperature gradients were quite high in all the simulations, hence in this region CET depended mainly on the nuclei density. On the contrary, in the zone of radial growth, radial temperature gradients and growth velocities were lower, so CET depended more on the undercooling required for equiaxed nucleation.

Comparison with experiments

Experimental results for case studies PD1, PD2, PD3 and PD4 can be found in the literature [16], and are shown in figure 3.17. In particular, for PD2 and PD4 only axial columnar and radial columnar grains were observed in the samples. The region of mixed axial and radial columnar grains went from x=65 mm to x=68 mm for PD2, and from x=57 mm to

x=65 mm for PD4. The length of this mixed region was slightly overestimated by the model (see table 3.5), however its position in the sample was close to the one measured in the experiments. According to Hunt's model, it would seem that the nuclei density in these samples was lower than 0.01 mm^{-3} or that the undercooling required for equiaxed grain nucleation was higher than 4 °C.

Different situations were observed in PD1 and PD3. In the first case, a zone with mixed columnar, equiaxed and radial grains was found between a fully axial columnar and a fully radial columnar region, in particular from x=70 mm to x=115 mm. From the simulation results, this situation is close to the one obtained with values of nuclei density around 1 mm^{-3} with nucleation undercooling between 1 and 2 °C. In this case the numerical model predicts that CET in the radial zone would occur after the one in front of the axial marker. This could explain the formation of a region where all the three structures are present simultaneously. In fact, equiaxed grains would grow and block the axial marker, but some radial growth could still occur.

On the other hand, in PD3 a region of fully equiaxed grains was observed from x=76 mm to x=100 mm, followed by a fully radial region. In this case, the best agreement with the model is found when ΔT_{nucl}=3°C and N_0=0.1 mm^{-3}. Interestingly, with these values, the model predicts an earlier CET in the radial region. Hence the growth of radial grains is immediately blocked, unlike in the previous case. This could explain the different grain structure observed in the experiments.

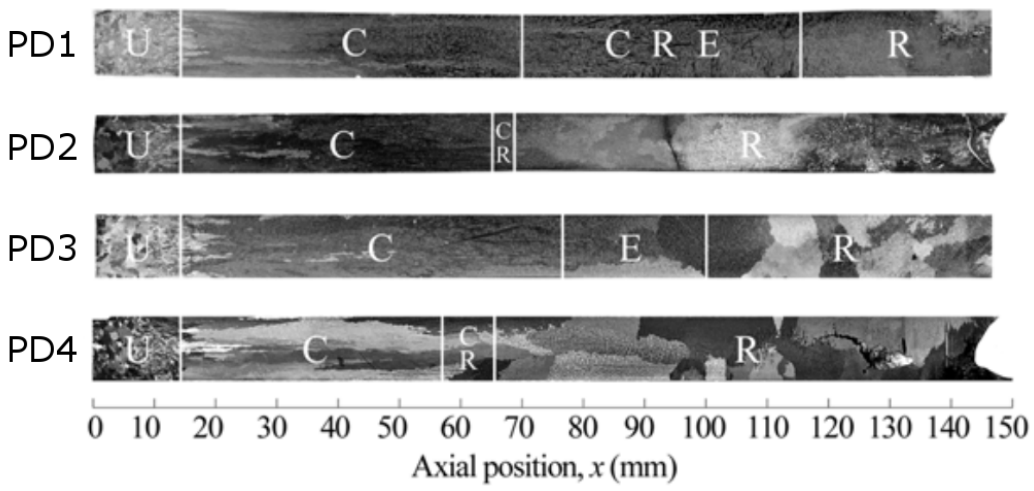

FIGURE 3.17: Images of samples showing different grain regions: U = unmelted, C = axial columnar, R = radial columnar, E = equiaxed [16].

From this comparison, it is evident that the conditions in the samples where not consistent during the different experiments PD1, PD2, PD3 and PD4. The numerical model is

able to predict, at least qualitatively, the different grain structures that could develop in the samples, showing that also small variations in the number and quality of nucleation seeds in the material could lead to different situations.

3.4 Conclusions

A 2D axisymmetric transient model for Bridgman and power down solidification was presented. The model included a front tracking algorithm to simulate the nucleation and growth of axial columnar and radial columnar grains in cylindrical samples. Equiaxed grain growth was not directly simulated, but the likelihood of CET in different scenarios was investigated indirectly by the means of Browne equiaxed index [22] and Hunt model for CET [23]. The numerical model was applied to investigate the grain structure development in γ-TiAl samples subjected to cooling rates of 15, 20, 30 and 50 °C/min. In all the cases, the cooling rate was sufficiently high to induce a negative radial temperature gradient in the undercooled liquid region, leading to the nucleation and growth of radial columnar grains. In the absence of equiaxed growth in the samples, the model predicted the transition from a zone with mixed axial and radial columnar grains to a fully radial grain region. The position of this transition in the samples was less advanced when higher cooling rates were applied. The likelihood of CET was investigated both in the region in front of the axial marker, characterized by an axial temperature gradient, and in the rightmost part of the sample, characterized by a radial temperature gradient. The results suggest that the occurrence of CET highly depends on the values of equiaxed nuclei density and the level of undercooling required for their nucleation. Comparison with experiments [15, 16] showed good qualitative agreement, even though the limited availability and significant variability of experimental data did not allow for a thorough validation of the model. Plans for future work include further investigation of different case studies, and the inclusion of a direct model for simulating equiaxed grains growth.

3.5 Addendum

3.5.1 Indirect evaluation of CET position

In this section, further considerations of CET occurring during the case studies PD1 to PD4 (table 3.4) are discussed, and the adaptation of Hunt's model for CET to the 2D front tracking model is refined.

As mentioned in section 3.2.3, Hunt's model is formulated for 1D steady state directional solidification, as it defines a critical temperature gradient G_{CET} in the growth direction below which fully equiaxed growth is predicted. In section 3.3.2, Hunt's CET predictor is adapted to the 2D axisymmetric front tracking model by investigating the conditions for CET at two

locations where columnar growth and temperature gradient in the sample are approximated as either 1D axial or 1D radial. This analysis predicts that, in general, CET in the axial columnar and radial columnar regions occurs at different times, due to the different thermal conditions across the sample. This result suggests the possible formation of different combinations of axial columnar, radial columnar, and equiaxed regions.

In order to ease the visualization of the different grain regions which might develop during the solidification process, here Hunt's condition for CET (equation 3.8) is evaluated for each front marker, by considering the component of the temperature gradient in the direction of the marker's advance as follows:

$$\nabla T_t \cdot \hat{e}_t < G_{CET} \tag{3.14}$$

where ∇T_t is the temperature gradient calculated at each marker's position, and $\hat{e}_t$ is the unit vector in the direction of each marker's displacement, *i.e.*, $\hat{e}_t = \boldsymbol{v}_t/|\boldsymbol{v}_t|$. Again, G_{CET} is a function of the temperature undercooling at the marker's position ΔT_t, and of the values of nucleation undercooling ΔT_{nucl} and nuclei density N_0.

Hence, condition 3.14 is evaluated and stored for each front marker at every time step during the simulations. The results of this analysis are then superimposed to the plots of the markers positions in time (figure 3.12), by deleting from the figures all the traces of markers that satisfy condition 3.14. In this way, regions of equiaxed growth are identified in the samples. It should be remembered that this is a qualitative evaluation of CET, since the one proposed here is a post-process graphic operation, and no blocking criterion is applied to the front markers during the simulations, nor equiaxed growth is directly modelled. Results of this operation, repeated for different values of ΔT_{nucl} and N_0, are shown in figures 3.18 and 3.19.

Figure 3.18 reports the graphical evaluation of CET for different values of the nucleation undercooling, when a nuclei density of 0.1 mm^{-3} is considered. The left column in figure 3.18 shows results for PD1 (low cooling rate), while the right column shows results for PD4 (high cooling rate). As one would expect, CET occurs earlier in the samples when the assumed nucleation undercooling for equiaxed growth is lower. Also, CET occurs earlier when the applied cooling rate is higher (PD4), since the undercooling in the liquid region is larger (see figure 3.14). Nonetheless, the position of CET in PD4 occurs at a more advanced position with respect to the radial heat flux reversal (red lines), hence more extended radial columnar regions are predicted in the samples along with axial columnar and equiaxed ones. Interestingly, in the case of high nucleation undercooling (ΔT_{nucl}=4°C), the equiaxed grain

region in PD4 is found after the transition to a fully radial columnar region. On the other hand, for PD1 no CET is registered in the sample when ΔT_{nucl}=4°C, since the sufficient level of undercooling in the liquid is not reached. Therefore, for a given value of the nuclei density, CET at lower cooling rates might not occur if the nucleation undercooling of equiaxed grains is not sufficiently low.

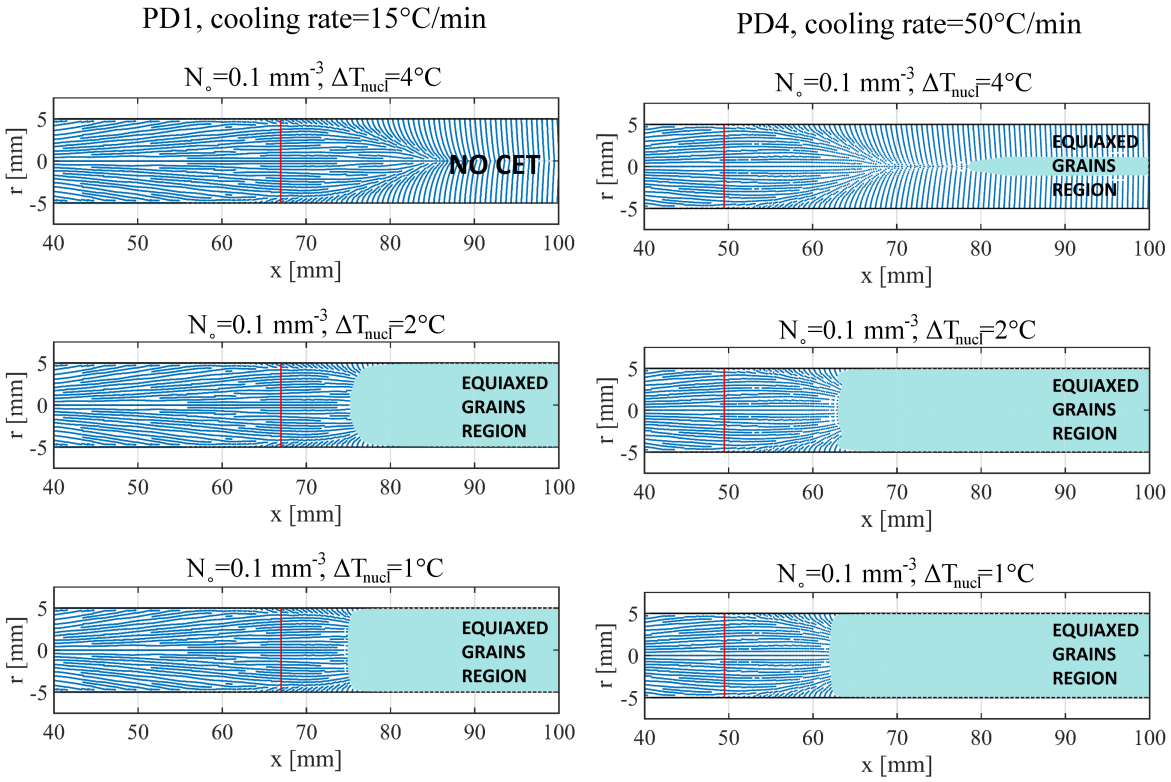

FIGURE 3.18: Qualitative evaluation of CET position for different values of nucleation undercooling ΔT_{nucl}

Figure 3.19 shows the qualitative evaluation of CET for different values of the nuclei density N_0, assuming that the undercooling required for equiaxed nucleation is ΔT_{nucl}=2°C. As for the previous figure, the left column in figure 3.19 shows results for PD1 (low cooling rate), while the right column shows results for PD4 (high cooling rate). As expected, CET occurs earlier when the equiaxed nuclei density is higher. As for the previous case, at lower cooling rates (PD1) CET occurs at a more advanced position in the sample, but at an earlier stage with respect to the radial heat flux reversal. Noticeably, for a low value of the nuclei density (N_0=0.01 mm^{-3}), CET is predicted only for PD1. This is due to the fact that for higher growth rates of the columnar front, which occur in PD4, a much lower temperature gradient is required for CET to occur, since $G_{CET} \propto N_0^{1/3}$. Therefore, at higher cooling rates, CET might not occur if the nuclei density is not sufficiently high.

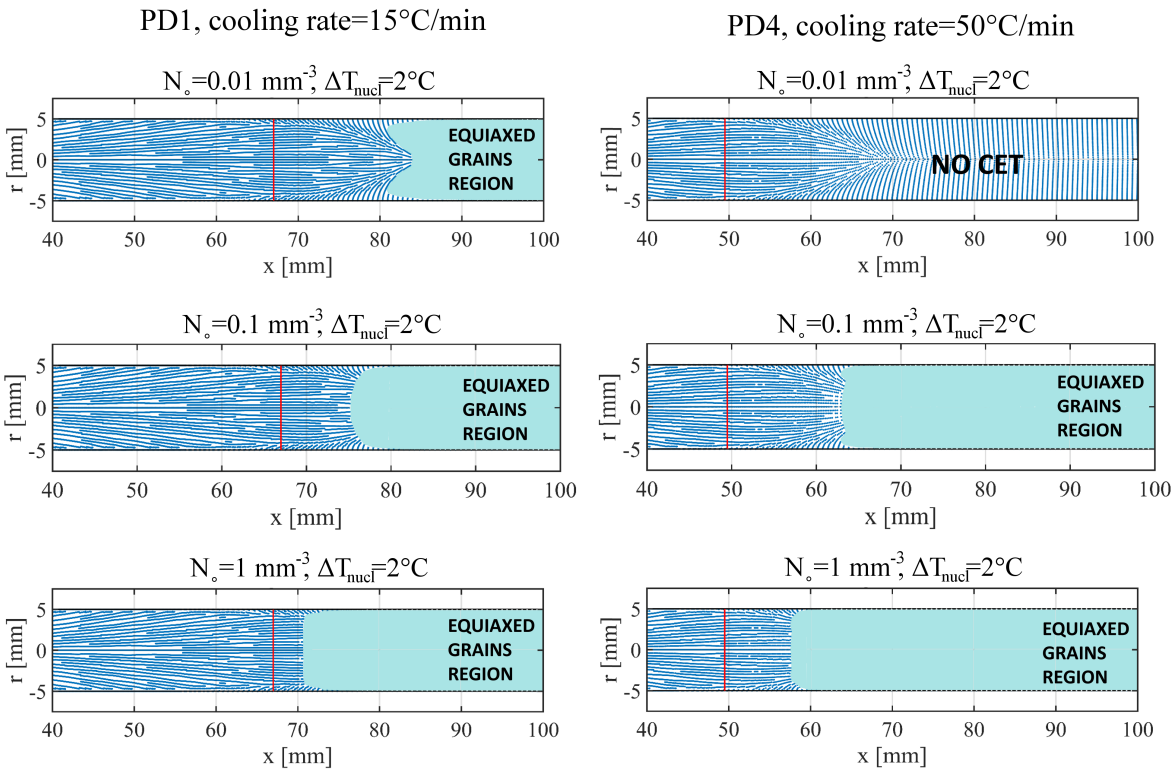

FIGURE 3.19: Qualitative evaluation of CET position for different values of nuclei density N_0

Acknowledgements

The author would like to thank Dr. Jurai Lapin and Dr. Robin P. Mooney for providing experimental data for comparisons.

References

[1] P. W. Bridgman, "Certain Physical Properties of Single Crystals of Tungsten, Antimony, Bismuth, Tellurium, Cadmium, Zinc, and Tin," *Proceedings of the American Academy of Arts and Sciences*, vol. 60, 1925.

[2] G. Reinhart, N. Mangelinck-Noël, H. Nguyen-Thi, T. Schenk, J. Gastaldi, B. Billia, P. Pino, J. Härtwig, and J. Baruchel, "Investigation of columnar-equiaxed transition and equiaxed growth of aluminium based alloys by X-ray radiography," *Mater. Sci. Eng. A*, vol. 413, pp. 384–388, 2005.

[3] M. Gündüz and E. Çadırlı, "Directional solidification of aluminium-copper alloys," *Mater. Sci. Eng. A*, vol. 327, no. 2, pp. 167–185, 2002.

[4] W. U. Mirihanage, D. J. Browne, G. Zimmermann, and L. Sturz, "Simulation of international space station microgravity directional solidification experiments on columnar-to-equiaxed transition," *Acta Mater.*, vol. 60, no. 18, pp. 6362–6371, 2012.

[5] E. Çadırlı, "Effect of solidification parameters on mechanical properties of directionally solidified al-rich al-cu alloys," *Metals and Materials International*, vol. 19, no. 3, pp. 411–422, 2013.

[6] D. Liu, N. Mangelinck-Noël, C.-A. Gandin, G. Zimmermann, L. Sturz, H. Nguyen Thi, and B. Billia, "Structures in directionally solidified Al-7wt.% Si alloys: Benchmark experiments under microgravity," *Acta Mater.*, vol. 64, pp. 253–265, 2014.

[7] J. Fan, J. Liu, S. Tian, S. Wu, S. Wang, H. Gao, J. Guo, X. Wang, Y. Su, and H. Fu, "Effect of solidification parameters on microstructural characteristics and mechanical properties of directionally solidified binary TiAl alloy," *J. Alloys Compd.*, vol. 650, pp. 8–14, 2015.

[8] D. Dimiduk, "Gamma titanium aluminide alloys - an assessment within the competition of aerospace structural materials," *Mater. Sci. Eng. A*, vol. 263, no. 2, pp. 281–288, 1999.

[9] H. Clemens and S. Mayer, "Design, processing, microstructure, properties, and applications of advanced intermetallic TiAl alloys," *Adv. Eng. Mater.*, vol. 15, no. 4, pp. 191–215, 2013.

[10] F. Appel, H. Clemens, and F. Fischer, "Modeling concepts for intermetallic titanium aluminides," *Prog. Mater. Sci.*, vol. 81, pp. 55–124, 2016.

[11] H. Saari, J. Beddoes, D. Seo, and L. Zhao, "Development of directionally solidified γ-TiAl structures," *Intermetallics*, vol. 13, no. 9, pp. 937–943, 2005.

[12] H. Zhong, S. Li, H. Kou, and J. Li, "The solidification path related columnar-to-equiaxed transition in Ti–Al alloys," *Intermetallics*, vol. 59, pp. 81–86, 2015.

[13] J. Lapin and Z. Gabalcová, "Solidification behaviour of TiAl-based alloys studied by directional solidification technique," *Intermetallics*, vol. 19, no. 6, pp. 797–804, 2011.

[14] J. Lapin, Z. Gabalcová, U. Hecht, R. P. Mooney, and S. Mcfadden, "Columnar to Equiaxed Transition in Peritectic TiAl Based Alloy Studied by a Power-Down Technique," *Material Science Foum*, vol. 790-791, pp. 193–198, 2014.

[15] R. P. Mooney, S. McFadden, Z. Gabalcová, and J. Lapin, "An experimental-numerical method for estimating heat transfer in a Bridgman furnace," *Appl. Therm. Eng.*, vol. 67, no. 1-2, pp. 61–71, 2014.

[16] R. P. Mooney, U. Hecht, Z. Gabalcová, J. Lapin, and S. McFadden, "Directional solidification of a TiAl alloy by combined Bridgman and power-down technique," *Kov. Mater. - Met. Mater.*, vol. 53, pp. 187–197, 2015.

[17] R. P. Mooney, J. Lapin, A. Klimová, and S. McFadden, "Conditions for CET in a gamma TiAl alloy," *IOP Conf. Ser. Mater. Sci. Eng.*, vol. 84, no. 1, 2015.

[18] S. McFadden, D. J. Browne, and C. A. Gandin, "A Comparison of Columnar-to-Equiaxed Transition Prediction Methods Using Simulation of the Growing Columnar Front," *Metall. Mater. Trans. A*, vol. 40, no. 3, pp. 662–672, 2009.

[19] M. Seredyński, S. Battaglioli, R. Mooney, A. Robinson, J. Banaszek, and S. McFadden, "Code-to-code verification of an axisymmetric model of the Bridgman solidification process for alloys.," *Int. J. Numer. Methods Heat Fluid Flow*, vol. 27, no. 5, pp. 1142–1157, 2017.

[20] S. Battaglioli, S. McFadden, and A. Robinson, "Numerical simulation of Bridgman solidification of binary alloys," *Int. J. Heat Mass Transf.*, vol. 104, pp. 199–211, 2017.

[21] D. J. Browne and J. D. Hunt, "A Fixed Grid Front-Tracking Model of the Growth of a Columnar Front and an Equiaxed Grain During Solidification of an Alloy," *Numer. Heat Transf. Part B Fundam.*, vol. 45, no. 5, pp. 395–419, 2004.

[22] D. J. Browne, "A New Equiaxed Solidification Predictor from a Model of Columnar Growth," *ISIJ Int.*, vol. 45, no. 1, pp. 37–44, 2005.

[23] J. D. Hunt, "Steady state columnar and equiaxed growth of dendrites and eutectic," *Mater. Sci. Eng.*, vol. 65, no. 1, pp. 75–83, 1984.

[24] W. Bennon and F. Incropera, "A continuum model for momentum, heat and species transport in binary solid-liquid phase change systems I. Model formulation," *Int. J. Heat Mass Transf.*, vol. 30, no. 10, pp. 2161–2170, 1987.

[25] J. Ni and F. P. Incropera, "Extension of the continuum model for transport phenomena occurring during metal alloy solidification-I. The conservation equations," *Int. J. Heat Mass Transf.*, vol. 38, no. 7, pp. 1271–1284, 1995.

[26] M. Rebow, D. J. Browne, and Y. Fautrelle, "Combined Analytical and Numerical Front Tracking Approach to Modeling Directional Solidification of a TiAl-Based Intermetallic Alloy for Design of Microgravity Experiments," *Mater. Sci. Forum*, vol. 649, pp. 243–248, 2010.

[27] F. P. Incropera, D. P. Dewitt, T. L. Bergman, and A. S. Lavine, *Fundamentals of Heat and Mass Transfer*. John Wiley & Sons, 6th ed., 2007.

[28] Y. S. Touloukian, R. W. Powell, C. Y. Ho, and P. G. Klemens, *Thermophysical Properties of Matter, Vol 2, Thermal Conductivities of Nonmetallic Solids.* IFI/Plenum Data, New York, 1970.

[29] I. Egry, R. Brooks, D. Holland-Moritz, R. Novakovic, T. Matsushita, E. Ricci, S. Seetharaman, R. Wunderlich, and D. Jarvis, "Thermophysical properties of γ-titanium aluminide: The european IMPRESS project," *Int. J. Thermophys.*, vol. 28, pp. 1026–1036, 2007.

[30] W. Rosch, W. Jesser, W. Debnam, A. Fripp, G. Woodell, and T. K. Pendergrass, "A technique for measuring the heat transfer coefficient inside a Bridgman furnace," *J. Cryst. Growth*, vol. 128, pp. 1187–1192, 1993.

[31] W. Rosch, A. Fripp, W. Debnam, and T. Pendergrass, "Heat transfer measurements in the Bridgman configuration," *J. Cryst. Growth*, vol. 137, no. 1-2, pp. 54–58, 1994.

Chapter 4

Influence of Natural and Forced Gravity Conditions during Directional Columnar Solidification

Abstract

The previous chapter reports an analysis of a transient process which combines Bridgman and power down directional solidification of TiAl alloys in the absence of convection. The adopted front tracking model, also coupled with indirect methods for CET prediction, shows how the development of different grain regions, namely axial columnar, radial columnar and equiaxed, depends on process parameters such as temperature distribution and applied cooling rates, as well as on properties such as the degree of inoculation of the melt and nucleation undercooling required for equiaxed growth. In this chapter, the previous front tracking model is significantly developed, by including the solution of momentum equations in order to predict thermal convection in the liquid region as well as in the columnar mush (treated as an isotropic porous medium). This improvement is introduced with the aim to fulfill the overarching objective of ESA's GRADECET project to investigate TiAl alloys solidification under different gravity conditions. Accordingly, the simulation setup employed in the study reproduces the one used in experimental campaigns carried out on the MAXUS 9 rocket (microgravity) and on ESA's Large Diameter Centrifuge (hypergravity). The ability of the model in predicting thermal convection is demonstrated by considering several case studies. Results show that the evolution of fluid flow patterns in the samples depends on the external forces considered, combined to the transient change of axial and radial temperature gradients that occur during the solidification process. A parametric study of the directional solidification process on a centrifuge is performed by changing the value of the centrifuge arm and rotation rate and results are compared to predictions derived from non-dimensional considerations.

4.1 Introduction

Metallic alloy components for advanced engineering applications, such as aerospace, automotive, and medical industries, are often manufactured by casting processes like investment casting or directional solidification. One of the main advantages of these technologies is the possibility to produce near-net shape components. Nonetheless, in order to produce a component that is free of defects and satisfies given requirements, it is necessary to identify and control important process parameters. In particular, to ensure the attainment of required mechanical properties, it is essential to be able to control the final grain structure of the casting. The development of columnar grains, equiaxed grains, or columnar to equiaxed transition (CET), depends on the transient thermal and fluid flow conditions in the molten alloy. These, in turn, are functions of several interdependent variables, such as imposed temperature gradients, cooling rates, geometric factors and the presence of external forces. For this reason, the choice of process parameters is not straightforward and requires a thorough analysis of the process under consideration. For instance, in the case of directional solidification, specifically defined axial temperature gradients, combined with precise cooling rates (power down mode) or pulling rates (Bridgman mode) are required to ensure the development of the desired grain structure. For example, fully axial columnar grains, desired in industrial applications such as the production of turbine blades, are achieved by using high temperature gradients and low pulling rates [1–3]. On the other hand, several studies show that low temperature gradients combined with high pulling or cooling rates promote the formation of a more extended undercooled region, and hence equiaxed growth [4, 5]. Nonetheless, high pulling and cooling rates might induce radial temperature gradients and the development of unwanted radial columnar grains [6–8].

In addition to thermal conditions, it is imperative to consider also the effect of external forces which might be present during the solidification process. First of all, unless in the case of microgravity experiments in space, any solidifying alloy is subject to terrestrial gravitational acceleration. This, combined with temperature, density, and composition gradients, induces several phenomena such as convection in the melt, segregation, and buoyancy or sedimentation. For this reason, the influence of terrestrial gravitational field on solidification has been extensively investigated in the literature. Narrowing down to studies that consider directional solidification, different conditions can be investigated, such as thermal stabilizing situations, *i.e.*, upward solidification, or unstabilizing conditions such as in the case of downward solidification. Nonetheless, in both cases predicting the final outcome is not trivial. For example, it has been shown that even in stabilizing conditions, convection may arise due to radial temperature gradients, inducing significant segregation [9–12]. On the other hand strong unsteady convection might lead to a high degree of mixing and reduce segregation [9]. Considering the effect on the development of the grain structure, natural convection modifies the heat fluxes in the melt, affecting temperature gradients and the extent of the

undercooled liquid zone. In general, previous studies showed that melt convection has a tendency to promote the occurrence of CET, due both to the reduction of temperature gradients, and to the mechanism of dendrite fragmentation that improves equiaxed nucleation [4,13,14].

Besides terrestrial gravity, additional forces could be related to external accelerations imposed to the mould. One important example is centrifugal casting. This process is often employed since centrifugal forces help mould feeding and filling processes, especially when dealing with lightweight or highly reactive alloys. At the same time, however, centrifugal acceleration influences melt convection. Furthermore, in the case of rotation, the effect of Coriolis acceleration cannot be neglected. For what concerns directional solidification under the influence of centrifugal and Coriolis forces, most studies in the literature focus on crystal growth of semiconductors rather than alloy solidification. A remarkable result was found by Rodot et al. [15, 16] when studying the effect of increased gravity obtained by centrifugal force on crystal growth of PbTe and Pb1-xSnxTe. They observed that, for a well defined value of the centrifugal force, the crystal quality and homogeneity were improved, and the segregation profiles were similar to the ones expected in the absence of convection under microgravity. The authors hypothesized that this particular condition was a combined effect of the centrifugal force and the action of Coriolis acceleration. Müller and Weber [17,18] carried out an extensive study, both experimental and numerical, for better understanding the stabilizing effect of centrifugal motion on the convective flow during solidification. From the experiments, the authors observed that for particular acceleration levels, the crystal started to grow without striations, due to a transition from an unsteady to a steady flow. Accordingly, the numerical simulations predicted a transition from an unsteady flow state called I, to a steady flow state II. The authors concluded that the flow pattern in the sample, and hence the enhanced quality of the crystals grown at higher rotation speed, was an effect of Coriolis force, rather than centrifugal force. Lan et al. [19] performed a self-consistent simulation of gradient-freeze crystal growth in a centrifuge and observed that for a horizontal configuration (decreasing temperature with distance form centrifuge axis), the flow speed decreased monotonically with the rotation speed, and as result the unstable flow was suppressed; for a free-swing configuration a condition for a minimum convection was found, where Coriolis force balanced the gravitational ones. Several possible reasons for the minimum in convection were proposed by Wilcox et al [20], for example due to a balance between buoyancy forces and Coriolis forces, or the occurrence of thermal stability conditions (density gradients parallel to net acceleration vectors). However, predictions based on these criteria did not find a clear correlation with experimental results. It is worth noting that all the previous investigations are focused on crystal growth. On the other hand, to the author's knowledge, studies on directional solidification of metal alloys in centrifuges are not present in the published literature.

For the reasons highlighted above, it is evident that a full understanding of the effects of both thermal variables and external forces is required in order to predict the grain structure

development during a given solidification process and produce high quality castings. With this intent, a recent European project, called GRADECET (GRAvity Dependence of Columnar to Equiaxed Transition in TiAl alloys) has been dedicated to the investigation of the influence of gravity conditions on grain structure evolution in γ titanium aluminides. Titanium aluminides feature outstanding properties like low density and high specific strength, expecially at high temperatures. This makes them ideal candidates for the production of components such as low pressure turbine blades or turbocharger wheels [21, 22]. Yet, these alloys lack ductility at room temperature, hence processing routes such near-net shape investment casting are often employed [23, 24]. Furthermore, amongst casting techniques, centrifugal casting is particularly fitting for manufacturing γ-TiAl based parts, since these alloys have low density, high melting points, and components such as turbine blades show thin sections, hence would benefit from an assistant force to help the filling process.

In the framework of GRADECET, various directional solidification experiments were performed, also supported by several numerical studies. So far, most of the published works focused on directional solidification under microgravity [25] or terrestrial conditions [6]. On one hand, microgravity conditions are suitable for understanding the effect of process parameters such as imposed temperature gradients or cooling rates, since convection in the melt is suppressed. On the other hand, comparing results achieved in terrestrial conditions with microgravity ones allows one to discern the effect of natural convection. In addition to microgravity and 1g experiments, a series of hyper-gravity experiments have been recently performed in ESA's large diameter centrifuge, in order to extend the understanding of the influence of forced convection on titanium aluminide solidification.

In this context, the aim of the present paper is to perform a series of numerical simulations which reproduce experimental scenarios carried out within the GRADECET project, and to parametrically investigate the influence of gravity variations on fluid flow, temperature and grain structure during the process. In order to do so, a novel numerical model is proposed. A 2D axisymmetric front tracking algorithm has been recently developed by the author for the solution of directional solidification of cylindrical titanium aluminide samples [8]. In the original model convection in the melt was not treated. In the present work, a significan t improvement to the model is introduced. Alongside the heat equation, the solution of momentum equations is included, in order to capture the thermal convection induced by the presence of either terrestrial gravity or centrifugal and Coriolis accelerations. In the existing literature, the front tracking algorithm has been widely used for modelling binary or multicomponent alloys solidification [26–31]. The main feature of this method is the ability to capture the development of a columnar grain region and an undercooled liquid region, which can then be analysed for an indirect prediction of CET. The original front tracking model by Browne and Hunt [26] only considered diffusive heat transfer. The effect of buoyant

natural convection was included in the model by Banaszek et al. [28, 32], who simulated Al-Cu binary alloy solidification in a 2D square mould, equally cooled from all the four sides. Further contribution was given by Seredyński et al. [30, 33] with the inclusion of solutal convection for the study of macrosegregation. Also in this case, solidification of binary alloys in rectangular moulds was considered. So far, the front tracking model has not been applied to investigate the effect of buoyant natural convection during directional solidification, nor the effect of forced convection such as the one arising during centrifugal casting.
Therefore, the main objectives of the current work are:

- to describe the features of a new front tracking model able to capture transient directional solidification of multicomponent alloys in the presence of thermal convection induced by either terrestrial gravity or centrifugal and Coriolis accelerations during centrifugal casting;
- to reproduce microgravity directional solidification experiments, in order to tune boundary conditions and provide benchmark solutions for the comparison with solutions in the presence of convection;
- to investigate the influence of terrestrial gravity during vertical directional solidification when thermally stable (top heated) or thermally unstable (bottom heated) conditions are considered;
- to simulate the directional solidification process carried out on a centrifuge and perform a parametric investigation of the influence of centrifugal and Coriolis acceleration.

4.2 General methodology

4.2.1 Governing equations

In order to solve the heat and mass transfer problem in the sample material, continuity, momentum, and heat equations must be solved. The general derivation of these equations for a mixture of solid and liquid may be found in refs. [34, 35].

In this chapter, the following simplifying assumptions are considered:

- constant thermophysical properties;
- stationary solid phase;
- Boussinesq approximation for buoyancy induced thermal convection;
- no inclusion of solutal convection;
- laminar flow.

With these assumptions, the heat equation takes the form:

$$\frac{\partial T}{\partial t} + \boldsymbol{u}\nabla \cdot T = \alpha \nabla^2 T + \frac{L}{c_p}\frac{\partial G_s}{\partial t} \tag{4.1}$$

where all the quantities without subscript refer to the mixture of solid and liquid phase. Since the front tracking algorithm is employed to model solidification, it is possible to have control volumes where both a mushy zone and a fully liquid zone are present [8]. In such control volumes, G_s represents the overall solid fraction, and can be expressed as $G_s = g_s V_m / V_{CV}$, where $g_s = V_s/V_m$ is the volumetric solid fraction of the volume of mush, V_m, contained in the control volume (CV). In an analogous way, the overall liquid fraction in these CVs is defined as $G_l = (g_l V_m + 1 \cdot (V_{CV} - V_m))/V_{CV}$. Note that $g_s + g_l = 1$, hence also $G_l + G_s = 1$. In the CVs of mush not containing the front $G_s = g_s$ and $G_l = g_l$.

The second term on the left hand side of equation 4.1 represents advection of heat in the sample. Due to the assumption of stationary sample and stationary solid phase, this term is non-zero only in the mushy and liquid regions of the sample. Furthermore, the mixture velocity vector $\boldsymbol{u}$ is equal to $\boldsymbol{u} = G_l \boldsymbol{u}_l + G_s \boldsymbol{u}_s = G_l \boldsymbol{u}_l$.

With the assumption of constant thermophysical properties, the densities of the solid and liquid phases are the same, and constant in time. Therefore, continuity equation is defined as:

$$\nabla \cdot (\rho \boldsymbol{u}) = \rho \nabla \cdot (G_l \boldsymbol{u}_l) = 0 \tag{4.2}$$

In order to calculate the velocity field in the sample, the following Navier-Stokes equations must be solved in the mushy and liquid regions:

$$\frac{\partial \boldsymbol{u}}{\partial t} + \nabla \cdot (\boldsymbol{u}_l \boldsymbol{u}) = \nu_l \nabla^2 \boldsymbol{u} - \frac{G_l}{\rho_{ref}} \nabla p_l + G_l \boldsymbol{B} - \nu_l K_0 \frac{G_s^2}{G_l^3} \boldsymbol{u} \tag{4.3}$$

The last term of equation 4.3 corresponds to a damping term used to model the flow in the columnar mush as a Darcy flow in a porous medium [36]. K_0 is a morphological constant, defined as $K_0 = 180/\lambda_2^2$, where λ_2 is the secondary arm spacing.

The term $\boldsymbol{B}$ represents the body forces. With Boussinesq approximation, and in the presence of terrestrial, centrifugal, and Coriolis accelerations, this term is defined as:

$$\boldsymbol{B} = -\beta \left(T - T_{ref}\right) \left(\boldsymbol{g} - \boldsymbol{\omega} \times (\boldsymbol{\omega} \times \boldsymbol{R})\right) - 2 \left(\boldsymbol{\omega} \times \boldsymbol{u}\right) \tag{4.4}$$

where $\boldsymbol{R}$ is the distance from the axis of rotation, $\boldsymbol{\omega}$ is the angular velocity vector, and $\boldsymbol{g}$ is gravitational acceleration (see figure 4.10). Clearly, centrifugal acceleration, $-\boldsymbol{\omega}\times(\boldsymbol{\omega}\times\boldsymbol{R})$, and Coriolis acceleration, $-2\boldsymbol{\omega}\times\boldsymbol{u}$, are present only in the centrifugal casting scenarios.

4.2.2 Solidification model

Columnar growth during the solidification process is modelled by the means of a front tracking model (FTM), derived from the one originally proposed by Browne [26]. According to this method, the envelope of columnar grain tips is represented by a series of markers connected by linear segments. During solidification, the markers advance in a direction orthogonal to the front, at a rate which is a function of the level of undercooling ΔT_t at the marker location, calculated according to the dendrite tip kinetic law $|v_t| = C\Delta T_t^b$. A more detailed description of the model can be found in chapter 3. The front tracking model allows for the calculation of the volume of columnar mush V_m in the control volumes. In order to evaluate the overall solid fraction $G_s = g_s V_m / V_{CV}$, a closure relation is needed for the calculation of the mush solid fraction g_s. For this purpose, an appropriate solid fraction-temperature relationship, based on Scheil assumptions, was calculated for the alloys of interest and is shown in figure 4.1.

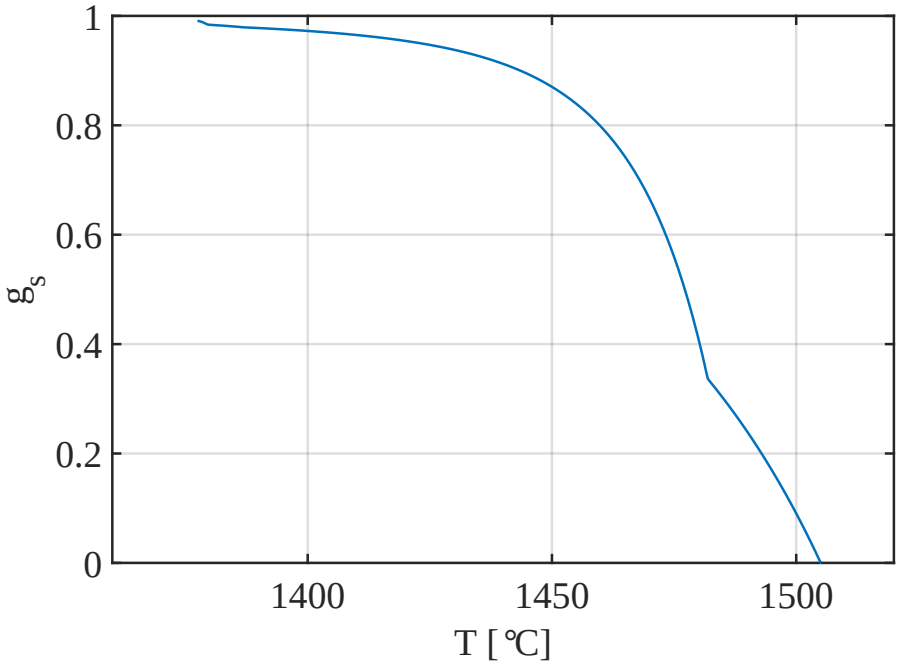

FIGURE 4.1: Solid fraction to temperature relationship for Ti-48Al-2Cr-2Nb estimated using Thermocalc via the "Modified Scheil Module".

4.2.3 Solution algorithm

A general flowchart of the solution algorithm employed is shown in figure 4.2. At the beginning of each timestep, the previous temperature field is used to update the position of the columnar front (time explicit FTM), and the new captured volumes V_m in the cells containing the front are calculated. Afterwards, an iterative loop for the time implicit calculation of velocity, pressure and temperature is performed. At the beginning of each iteration the SIMPLER algorithm is employed for the solution of velocity and pressure fields [37]. The obtained velocities are then employed for solving heat equation 4.1.

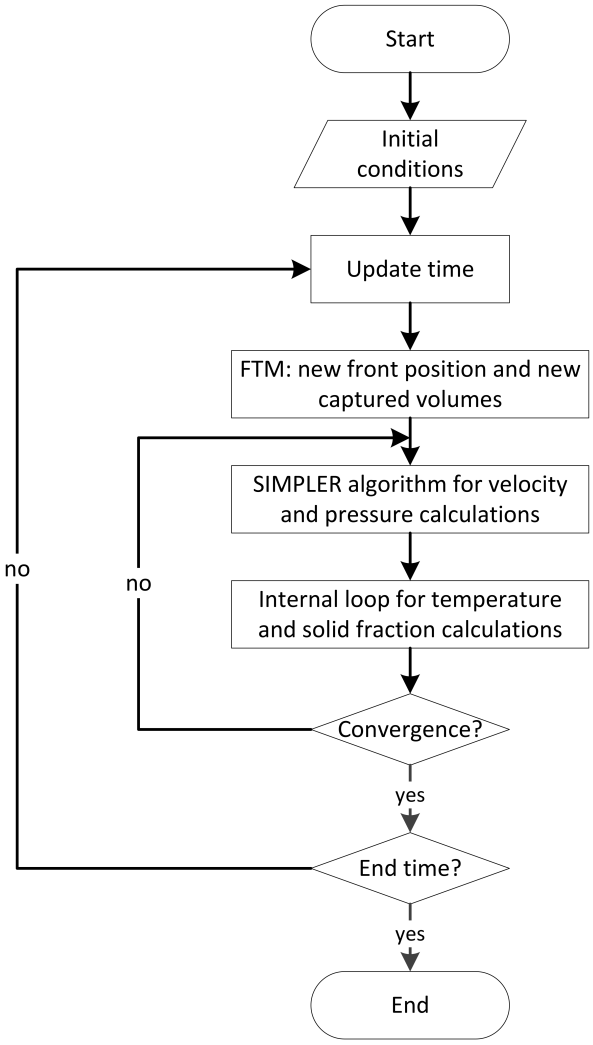

FIGURE 4.2: Flowchart of general solution algorithm.

Navier-Stokes and heat equations are solved by a fully implicit finite volume method [37, 38]. A staggered grid (see figure 4.3) is considered in order to avoid decoupling between pressure and velocity. Each equation is discretized on the appropriate grid for the variable ϕ

under consideration (u,p,T), taking the general form:

$$a_p\phi_p = \sum a_{nb}\phi_{nb} + a_p^o\phi_p^o + b_p \tag{4.5}$$

where the subscript p refers to the location where the variable is calculated and nb refers to the neighbouring nodes. a_i are coefficients deriving from the equation discretization. Diffusive terms are discretized by central differencing, while the hybrid scheme is used for convective terms. In the case of flow velocities and temperature, the system of equations deriving from the discretization is solved using a two dimensional line by line tridiagonal matrix algorithm [38]. For the solution of the system of equations for calculating pressure, a preconditioned biconjugate gradient algorithm is used to improve convergence [39, 40].

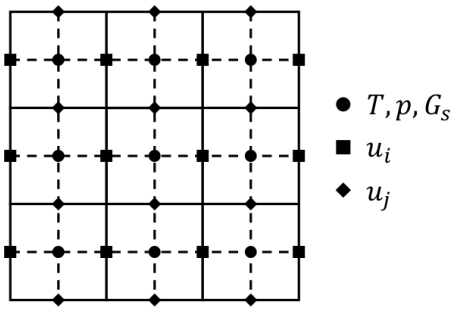

FIGURE 4.3: Staggered grid.

As figure 4.2 shows, an internal iterative loop is required for the solution of the heat equation. This is due to the presence of the last term of equation 4.1, which discretized becomes:

$$\frac{L}{c_p}\frac{\partial G_s}{\partial t} \approx \frac{L}{c_p V_{cv}}\left(V_m^o\frac{g_s - g_s^o}{\Delta t} + g_s^o\frac{V_m - V_m^o}{\Delta t}\right) \tag{4.6}$$

While the value of the volume of mush in the control volume V_m at the current time is calculated explicitly with the front tracking method, the current value of the fraction of solid g_s is a non-linear function of the current temperature. For solving the problem, an iterative method based on a Taylor series expansion is used [40], so that

$$g_s(T_n) \approx g_s(T_{n-1}) + \left(\frac{\partial g_s}{\partial T}\right)_{n-1}(T_n - T_{n-1}) \tag{4.7}$$

where the subscripts $n-1$ and n are the indices of the previous and current iteration respectively. Once the convergence of the internal loop is reached, a new iteration of the external loop is repeated and so on until convergence.

Finally, a further comment, related to the coupling of the time implicit model for the equations solution with the time explicit front tracking is needed. In fact, one of the main advantages in employing a time implicit method is the possibility to use an increased time step Δt without affecting the stability of the solution. However, using a large time step could induce numerical oscillations in the advancement velocity of the front markers, especially in the presence of high temperature gradients, as shown in figure 4.4. Relative to figure 4.4, numerical oscillations occur when the distance travelled by the marker advancing at a velocity v_{t_1} over a Δt is greater than the distance Δs_{max} between point 1 and the interception of the normal to the front and the liquidus isotherm. For a general marker, this condition can be written as follows:

$$v_t \Delta t < \Delta s_{max} \approx \frac{(T_L - T_t)}{G_n} \tag{4.8}$$

having considered, between the marker location and the liquidus isotherm, an average temperature gradient G_n normal to the front. Hence, a CFL condition for the front tracking model can be defined as:

$$C_{FTM} = \frac{v_t \Delta t G_n}{\Delta T_t} < C_{max} \tag{4.9}$$

where $C_{max} \leq 1$. Therefore, in order to avoid oscillations, a Δt that satisfies this condition during the whole simulation is necessary.

In order to preserve the advantage brought by the use of an implicit method, that allows to assume bigger Δt, avoiding at the same time oscillations, the total displacement of the markers during a time step Δt can be calculated as the sum of displacements calculated over N smaller time steps $\Delta t_{small} = \Delta t / N$ that satisfy the CFL condition. In this way, the velocity of the markers decreases according to the decreasing undercooling faced during the advance, and oscillations are prevented (see figure 4.4).

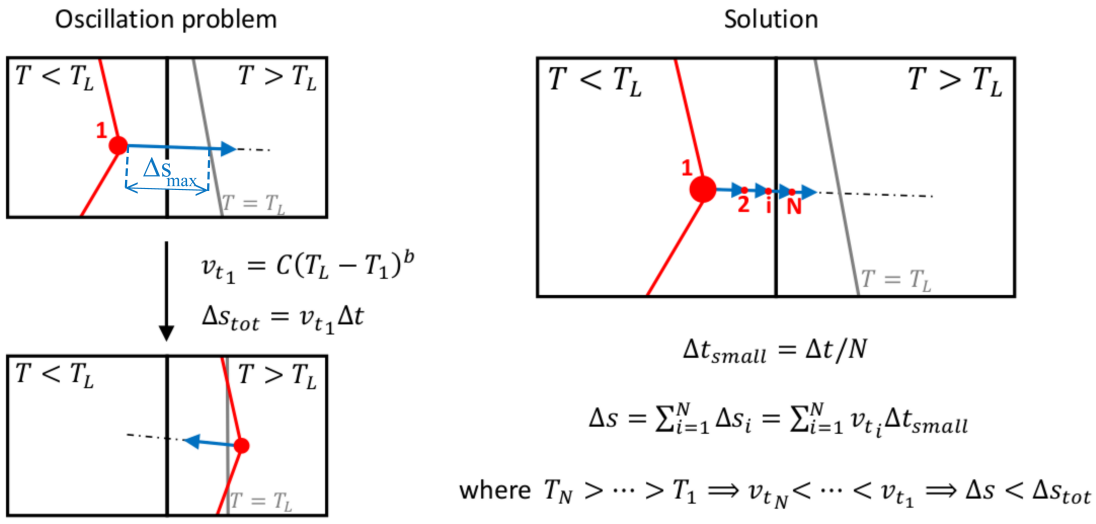

FIGURE 4.4: Solution for front tracking marker velocity oscillations arising from the use of large time steps in the presence of high temperature gradients.

4.3 Solidification in microgravity

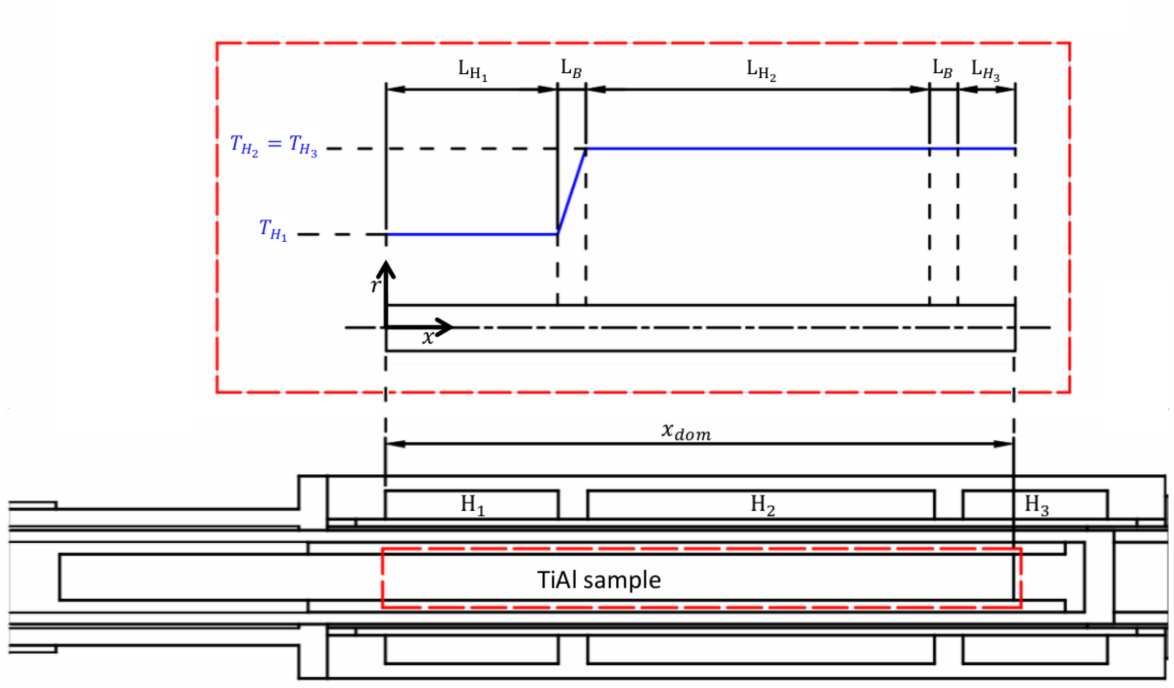

FIGURE 4.5: Computational domain.

In this case, the numerical model is employed for the simulation of directional solidification experiments carried out in microgravity conditions on board the MAXUS 9 rocket. The experimental apparatus and the related computational domain are shown in figure 4.5. For the simulations, a 2D axisymmetric domain is considered, corresponding to the portion of the

cylindrical sample in contact with the heaters. The main objective of these simulations is to tune the boundary conditions, based on available experimental data, and to give a benchmark solution for the comparison with results obtained in the presence of melt convection.
The geometrical data used in the simulations are listed in table 4.1.

TABLE 4.1: Geometrical data used in the simulations.

x_{dom} / [m]	r_{samp} / [m]	L_{H1} / [m]	L_{H2} / [m]	L_{H3} / [m]	L_B / [m]
$110{\cdot}10^{-3}$	$4{\cdot}10^{-3}$	$30{\cdot}10^{-3}$	$60{\cdot}10^{-3}$	$5{\cdot}10^{-3}$	$5{\cdot}10^{-3}$

The experiments and related simulations consist in three different phases:

- equalization: all three heaters H1, H2 and H3 are kept at a constant temperature in order to allow the realization of steady state conditions in the sample (duration of 184 s);
- first cooling: the temperatures of the hotter heaters H2 and H3 are kept constant, while the colder heater H1 is cooled at a constant rate (duration of 120 s);
- second cooling: constant cooling rates are imposed to all three heaters (duration of 380 s).

A final quenching was then performed during the experiments, but is not considered in the simulations. Temperature values and cooling rates applied to the sample are reported in table 4.2.

TABLE 4.2: Input data for the heaters during different stages of the process.

	Simulation stage		
	Equalization	First cooling	Second cooling
Duration	184 s	120 s	380 s
Heater 1	T_{H_1}=1543 °C	C_{H_1}=0.3 °C/s	C_{H_1}=0.1 °C/s
Heater 2	T_{H_2}=1623 °C	C_{H_2}=0.0 °C/s	C_{H_2}=0.4 °C/s
Heater 3	T_{H_3}=1623 °C	C_{H_3}=0.0 °C/s	C_{H_3}=0.4 °C/s

Due to the axisymmetry of the problem, the computations are carried out in half of the sample section, and an adiabatic condition is applied along the axis x. At the circumference of the sample (r=r_{samp}) convective conditions of the kind $-k\partial T/\partial r = h(T - T_{H_i})$ are applied.

At the left and right ends of the sample Neumann boundary conditions are imposed.

The sample material used in the experiments and simulations is Ti-48Al-2Cr-2Nb. The relative thermophysical properties used in the simulations are given in table 4.3. For the front tracking model, the marker velocity is calculated as $v_t = 2.63 \cdot 10^{-6} \Delta T_t^{2.79}$ m/s [41].

TABLE 4.3: Thermophysical properties of Ti-48Al-2Cr-2Nb used in the simulations.

	Ti-48Al-2Cr-2Nb
T_L=T_{ref} / [°C]	1505
T_S / [°C]	1377
ρ=ρ_{ref} / [kg/m^3]	3660
β / [°C^{-1}]	1.43·10^{-4}
ρL / [J/m^3]	1042.37·10^6
α / [m^2/s]	6·10^{-6}
c_p / [J/(kg°C)]	1000
ν / [m^2/s]	1·10^{-6}
K_0 / [m^{-2}]	1.8·10^{12}

4.3.1 Results and discussion

As stated above, the first objective of this analysis is to define appropriate boundary conditions in order to reproduce realistic results. Firstly, steady state temperature profiles measured by thermocouples at the end of the equalization stage were used to extrapolate the axial temperature gradients for Neumann conditions at the ends of the sample. In particular, values of circa 17·10^3 °C/m at the colder side (x=0), and 0 °C/m at the warmer side (x=x_{dom}) were measured and are applied in the simulations. In addition, the same steady state temperature profiles were used to solve an inverse heat transfer problem to calculate the value of the heat transfer coefficient for the convective boundary condition at the circumference of the sample. From this analysis, a mean value of h =120 W/(m^2°C) was estimated and therefore employed in the simulations.

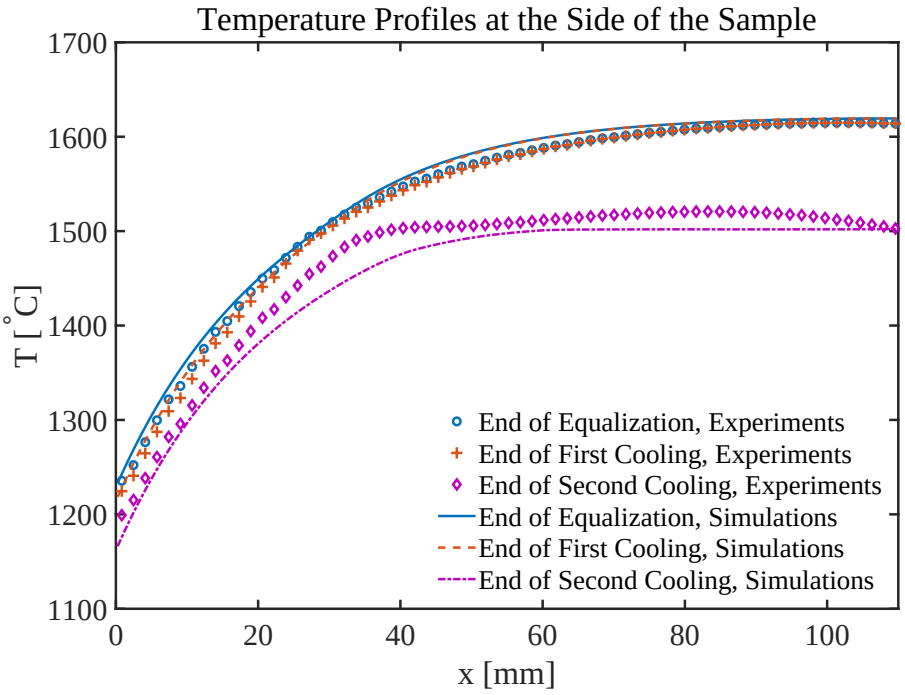

FIGURE 4.6: Temperature at the circumference of the sample (r=r_{samp}) at different times during the solidification process: comparison of experimental and simulated results.

Figure 4.6 shows a comparison of temperature profiles measured during the experiments at the side of the sample, and temperature profiles at r=r_{samp} obtained from the transient simulations using the aforementioned boundary conditions. It is evident that during the first part of the solidification process, excellent agreement between experimental and numerical results is achieved (mean percentage error=0.5%, max percentage error=1.4%). At the end of the second cooling stage differences are more pronounced (mean percentage error=1.2%, max percentage error=2.5%). This could be due to several reasons, such as the application of simplified boundary conditions in the model, the assumption of constant thermophysical properties for the alloy, or differences between the nominal and actual values of the heaters temperatures and cooling rates during the experiments.

Nonetheless, the agreement is deemed acceptable in order to give a good qualitative description of the process under consideration, and to serve as benchmark case for comparison with results in the presence of convection.

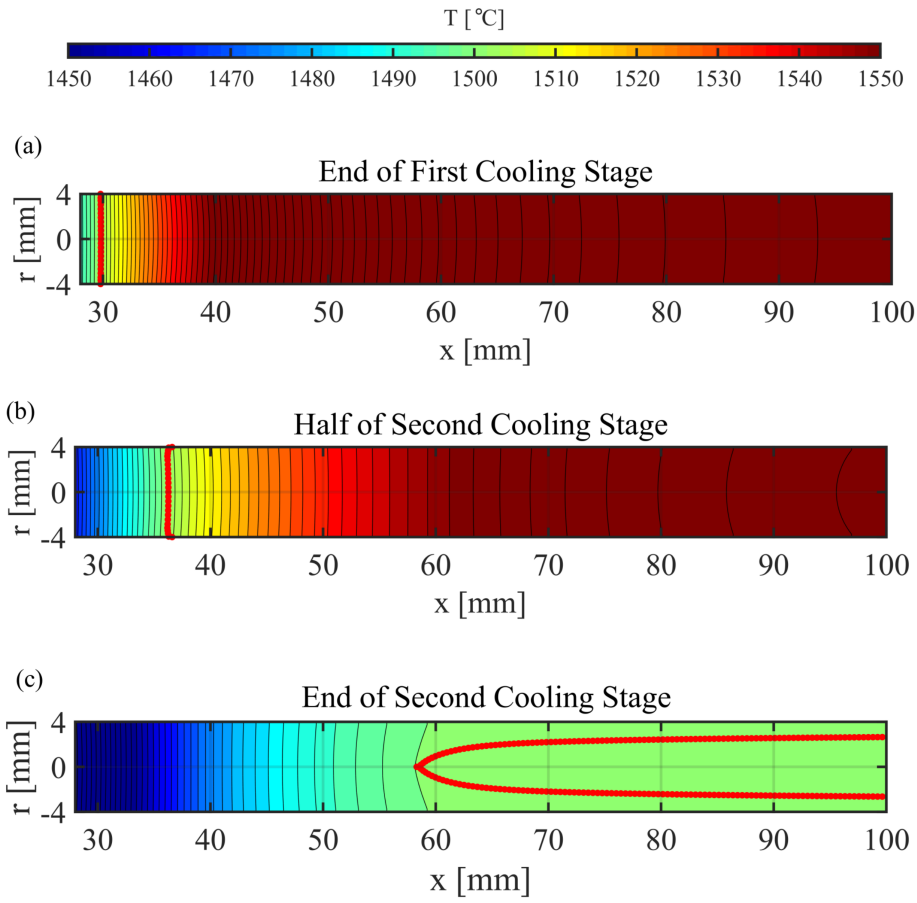

FIGURE 4.7: Columnar front position and temperature distribution in the sample at different times during the solidification process. Isotherms are drawn at intervals of 2°C.

Figure 4.7 shows the position of the columnar front (red) and temperature distribution in the sample at different stages of the solidification process. Initially (figure 4.7(a)), the isotherms in the entire liquid zone are flat or slightly convex, indicating that the temperature gradient is almost one dimensional in the axial direction, with small positive radial temperature gradient. The shape of the front is mostly flat, which predicts axial columnar growth. After some time (figure 4.7(b)), due to the cooling rate applied to the heaters, the radial temperature gradient towards the right end of the sample becomes negative. Also, the axial temperature gradient at the columnar front location decreases during the cooling process, which could promote the development of a columnar to equiaxed transition (CET). On the other hand, when an undercooling of 1°C is reached at the circumference of the sample, inactive front markers are activated and start moving towards the axis, indicating the possible growth of radial columnar grains. This is evident in the last stage of the process (figure 4.7(d)), where the columnar front advances in the radial direction from the circumference towards the axis. In this case, however it must be noticed that the radial temperature gradient is not significant and that the entire liquid region has an undercooling of about 3°C, therefore the occurrence of a CET which could prevent radial growth is likely.

4.4 Solidification under terrestrial gravity conditions

The scope of this investigation is to understand the influence of terrestrial gravity, hence buoyant natural thermal convection, on the solidification process. Two different cases of vertical directional solidification are investigated:

- thermally stable configuration with top heated furnace;
- thermally unstable configuration with bottom heated furnace.

For this analysis, the same set up and experimental scenario of the microgravity case is assumed. Since for vertical solidification the terrestrial gravity vector is aligned with the axis of the sample, a 2D axisymmetric domain is considered for the calculations. Note that for coherency with the notation adopted in the microgravity case, x is the coordinate in the direction of the axis of the sample, positive from the colder to the warmer heater, and r is the coordinate in the direction of the radius of the sample. Therefore, with this notation, terrestrial gravitational acceleration vector is directed in the negative x direction for the stable configuration, and positive x direction for the unstable configuration.

4.4.1 Results and discussion

Figure 4.8 shows the front position (red) and streamlines in the samples for the stable and unstable configurations at different times during the solidification process. Streamlines in figure 4.8 are drawn at intervals of 0.15 mm^2/s of the stream function. Also, in figure 4.8, green streamlines correspond to counter-clockwise rotating flow, while blue streamlines represent clockwise rotating flow.

At first glance, the images in figure 4.8 show that the columnar front position at different times is almost identical in the stable and unstable configurations, as well as in the microgravity case (see figure 4.7 for comparison). This is a direct consequence of the fact that the temperature distribution calculated in the samples during the simulations is almost the same in all cases, with maximum differences between the stable and unstable configurations of the order of 1°C. In order to explain this result, the nature of the heat transport problem under consideration is investigated by the means of Péclet number $Pe = l_{ref}u/\alpha$, which expresses the ratio of convective and diffusive heat transfer. Figure 4.9 shows the value of Péclet number derived from the simulations. In particular, a reference length $l_{ref} = r_{samp}/2$ is used in the calculations (usual choice for cylindrical systems), while at each timestep the values corresponding to the maximum and the mean magnitude of the fluid velocity are considered. As expected, in all cases the value of Péclet number is significantly below unity, demonstrating

that heat transfer in the sample is determined by diffusion rather than convection, which explains the small differences in the temperature distribution and front position in the different scenarios.

When observing the flow pattern in the sample, figure 4.8(a) shows that initially one rotating cell develops in the sample. As expected, buoyant convection, driven by the high axial temperature gradient, is stronger in the thermally unstable case. In particular, the maximum flow velocities, predicted at the end of the first cooling stage, are 0.24 mm/s in the stable case and 1.11 mm/s in the unstable configuration. It should be noted that according to these results, the maximum Reynolds number (unstable case) is $Re = u_{max} \cdot 2r_{samp}/\nu = 8.88$, justifying the assumption of laminar flow. In the stable case, the Reynolds number is of the order of 10^{-1}, which is in accordance to the one obtained in similar case studies from the literature [12].
The radial temperature gradient is positive for all the length of the region, hence temperatures on the axis are lower than the temperatures on the circumference. Accordingly, in the thermally stable case, fluid velocity is negative in the central part of the sample and positive in the external regions. The contrary is observed in the unstable case. After some time, as figure 4.8(b) shows, two counter-rotating cells are observed in the sample. In particular, the development of the second cell is due to the change in the radial temperature gradient arising from the applied cooling rate. In fact, observing the temperature distribution in figure 4.7(b), which as explained is analogous to the one obtained for the stable and unstable configurations, it can be seen that the isotherms in the first part of the liquid region are convex, corresponding to a positive radial temperature gradient, while they are concave towards the right end of the sample where the radial temperature gradient is negative. In case b, close to the front position, axial temperature gradient is still significant, therefore in the unstable configuration the cell on the left side of the sample is stronger than the one in the stable configuration. Nonetheless, the second cell on the right hand side of the sample is driven mainly by the radial temperature gradient, hence the magnitude of velocity is equivalent in the stable and unstable cases. Eventually, as figures 4.7(d) and 4.8(d) show, the radial temperature gradient becomes negative in all the liquid and mushy region, therefore there is another transition in the fluid flow from two to one rotating cell. Again, at this instant convection is driven by radial temperature gradient rather than axial ones, therefore its magnitude is the same in the stable and unstable configurations.

In summary, for the experimental scenario under consideration (tables 4.1 and 4.2), this investigation shows that, both in stable and unstable configurations, buoyant natural convection does not influence in a significant way the temperature field and columnar front evolution developing in the Ti-48Al-2Cr-2Nb samples. On one hand, this result suggests that for similar experimental scenarios and similar alloys, simpler numerical models that do not include

convection are still able to give sufficiently accurate information on the evolution of temperature and columnar growth. Nonetheless, the flow cells arising in the two configurations during the process show different intensity and rotate in opposite directions. This might induce different results in terms of aspects that are not captured by the current model, such as macrosegregation, dendrite fragmentation, or equiaxed grains floatation and sedimentation. Therefore, if such phenomena are to be investigated, the importance of considering the fluid flow appears evident.

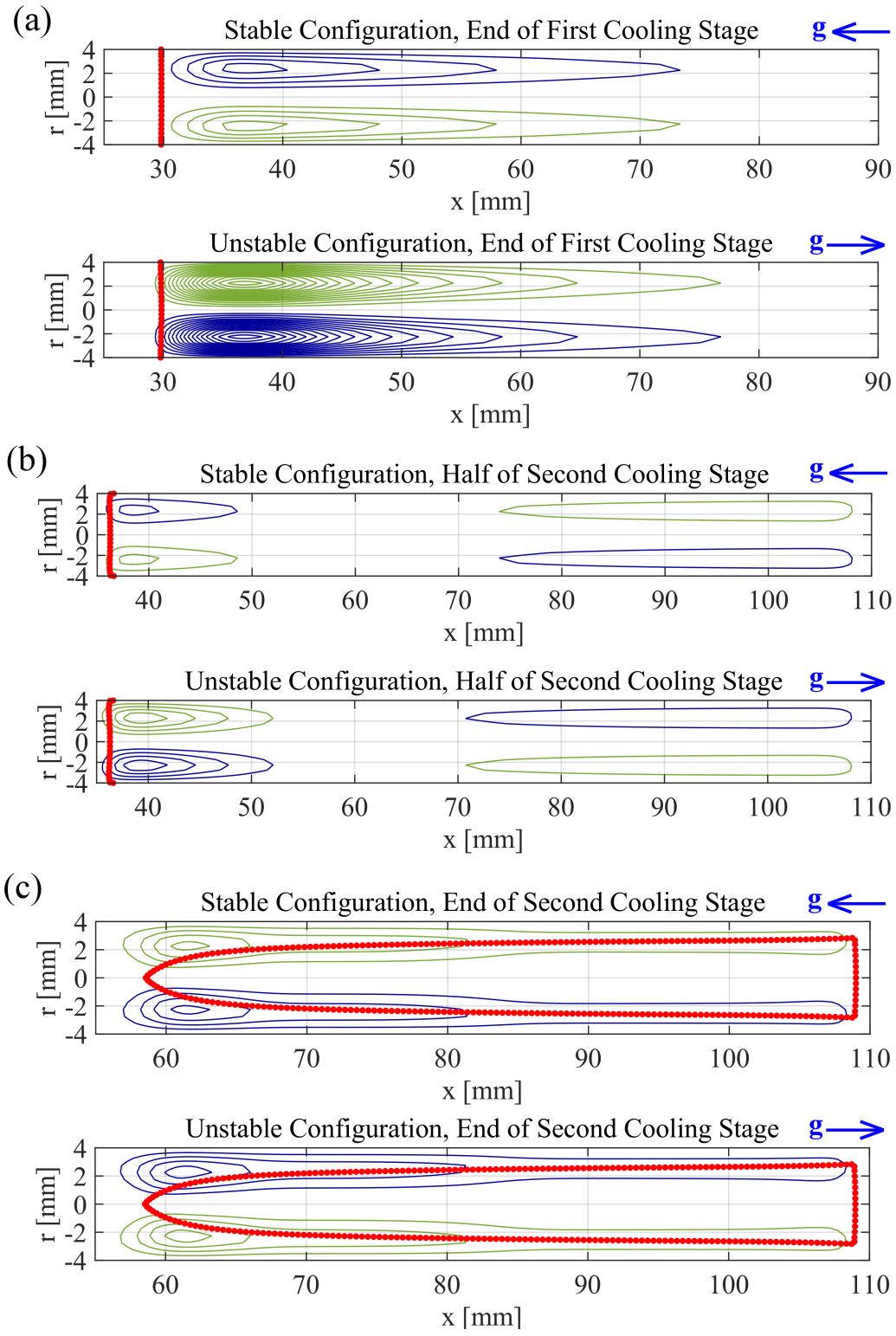

FIGURE 4.8: Streamlines in the sample at different times during the solidification process. Green streamlines correspond to counter-clockwise rotating flow, while blue stramlines correspond to clockwise rotating flow. Streamlines are drawn at intervals of 0.15 mm^2/s.

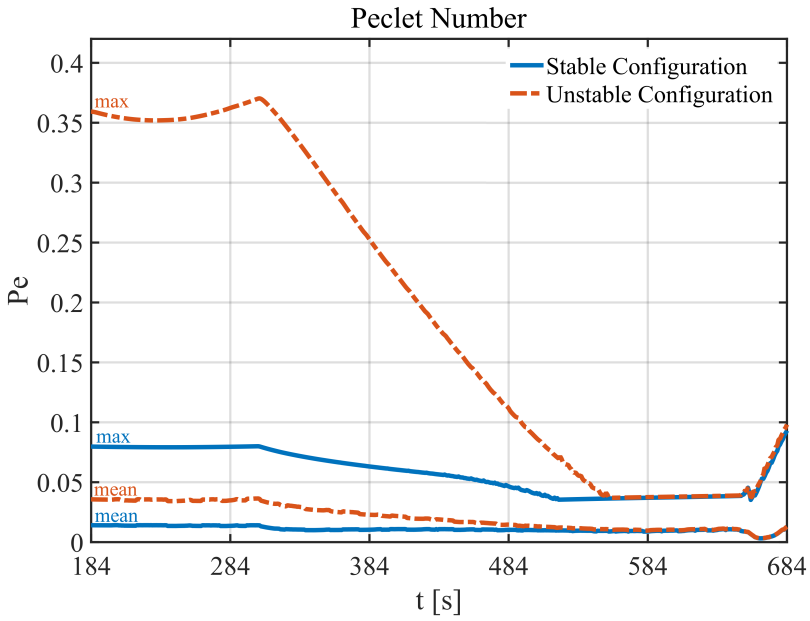

FIGURE 4.9: Maximum and mean value of the Peclét number registered in the sample during the solidification process.

4.5 Solidification on centrifuge

In this section, the front tracking model is used to investigate directional solidification on a centrifuge. In particular, the setup used for the simulations aims to reproduce a series of experiments carried out on ESA's Large Diameter Centrifuge (LDC) in the framework of the GRADECET project. During these experiments, centrifugal acceleration levels from 5 to 20 times terrestrial gravity are imposed by changing the angular velocity of the centrifuge. In addition, besides considering the influence of different rotation speed ω , the effect of an hypothetical variation of the length of the centrifuge arm R_C is investigated.

Figure 4.10 shows a schematic of the centrifugal solidification problem under consideration. A stable configuration (analogous to a top heated furnace) is adopted, *i.e.*, the colder heater is located externally with respect to the centrifuge axis. Unlike in the scenarios considered in the previous sections, in this case the real heat and fluid flow problem in the sample is purely three-dimensional, due to the presence of terrestrial gravity acting in the vertical direction, centrifugal acceleration acting radially with respect to the centrifuge axis, and Coriolis acceleration acting in the horizontal planes. However, the front tracking model employed in the present work is strictly 2D, its extension to a 3D geometry being very challenging and highly computationally expensive [42]. For this reason, the simulations are carried out considering a 2D planar domain in the horizontal plane which has the same dimensions of the cylindrical sample section. In this plane, the effects of both centrifugal and Coriolis accelerations are present, while the action of terrestrial gravity is not considered. Unlike the previous

cases, due to the presence of Coriolis acceleration, axisymmetry is not expected, therefore the computational domain includes the whole section of the sample. A new reference system (x', r') is introduced in order to make the analytical considerations reported in section 4.5.1 clearer. Nonetheless, all the results in section 4.5.2 are shown in the reference system (x, r) for consistency with the previous case studies.

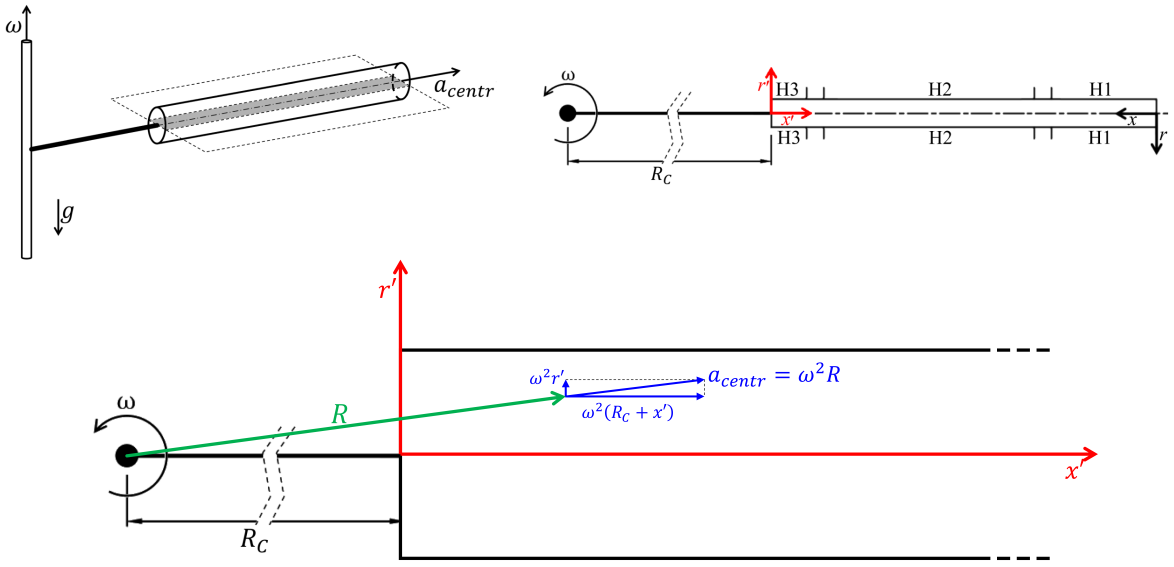

FIGURE 4.10: Schematic of the directional solidification process on a centrifuge and 2D planar computational domain used in the simulations.

The thermal conditions and material used in the simulations are the same as in the former cases. For the parametric investigation, several values of ω and R_C are considered, as reported in table 4.4.

TABLE 4.4: Input values of the angular velocity and centrifuge arm used in the parametric analysis. The bottom line shows the corresponding magnitude of centrifugal acceleration with respect to terrestrial gravity: $N_g \approx \omega^2 R_c/g$.

	Simulation run								
	S0	S1	S2	S3	S4	S5	S6	S7	S8
ω / [rad/s]	/	2.2	3.5	5	7	5	10	22	44
R_C / [m]	/	4	4	4	4	2	2	0.1	0.1
$\approx N_g$	1	2	5	10	20	5	20	5	20

Some considerations regarding the applicability of this model to real case studies are discussed. As stated above, due to the 2D nature of the front tracking model, a 2D planar domain, orthogonal to the rotation axis of the centrifuge, is considered, corresponding to a rectangular domain that extends indefinitely in the vertical direction. The real case scenario for GRADECET experiments in ESA's LDC is far more complex. Firstly, cylindrical samples are employed. Secondly, the samples are mounted on a gondola with a free swing configuration, so that the plane of rotation of the sample is not horizontal, but parallel to the resultant of terrestrial gravity and centrifugal acceleration acting in the centre of gravity of the gondola. For these reasons, forecasting the outcome for a real case study including all these aspects is not trivial, since complex flow patterns, such as helicoidal ones [43], might develop in the samples. Therefore, the necessity of a further development of a 3D model is undeniable. Still, it is believed that the prediction obtained for higher level of gravity (*e.g.*, simulation S4) could be qualitatively close to the experimental one, since for higher rotation rates the resultant of terrestrial gravity and centrifugal acceleration is almost horizontal (for S4 the inclination is about 2.68 degrees). Nonetheless, comparison with experimental results will be needed to validate this hypothesis.

4.5.1 Non-dimensional analysis

In order to ease the parametric investigation of the influence of centrifugation on melt convection, the dimensionless form of momentum equation 4.3 is considered. Hence, the following dimensionless quantities are defined:

$$\begin{gathered} \boldsymbol{x'}^* = \frac{\boldsymbol{x'}}{l_{ref}}; \quad \boldsymbol{r'}^* = \frac{\boldsymbol{r'}}{l_{ref}}; \quad T^* = \frac{T}{\Delta T_{ref}}; \quad \boldsymbol{u}^* = \frac{\boldsymbol{u}}{u_{ref}} \\ p^* = \frac{p}{\rho_{ref} u_{ref}^2}; \quad t^* = \frac{t}{l_{ref}/u_{ref}}; \quad K_0^* = \frac{K_0}{l_{ref}^{-2}} \end{gathered} \tag{4.10}$$

In addition, the following dimensionless numbers are introduced:

$$Re = \frac{u_{ref} l_{ref}}{\nu}; \quad Gr = \omega^2 R_C \frac{\beta \Delta T_{ref} l_{ref}^3}{\nu^2}; \quad Ro = \frac{u_{ref}}{2\omega l_{ref}} \tag{4.11}$$

In particular, the Reynolds number Re represents the ratio of inertial forces to viscous forces. The Grashof number Gr indicates the ratio of buoyancy forces to viscous forces. Finally, the Rossby number Ro expresses the ratio of inertial forces to Coriolis forces.

By substituting these scalings in eq. 4.3, it results:

$$\frac{\partial \boldsymbol{u}^*}{\partial t^*} + \nabla \cdot (\boldsymbol{u}_l^* \boldsymbol{u}^*) = \frac{1}{Re}\nabla^2 \boldsymbol{u}^* - G_l \nabla p_l^* + G_l \boldsymbol{B}^* - \frac{1}{Re} K_0^* \frac{G_s^2}{G_l^3} \boldsymbol{u}^* \tag{4.12}$$

The non dimensional expression of the term of body forces $\boldsymbol{B}$, defined in equation 4.4, is:

$$\boldsymbol{B}^* = -\frac{Gr}{Re^2}\left(T^* - T_{ref}^*\right)\left(\hat{e}_{\boldsymbol{R}_C} + \frac{\boldsymbol{x'}}{R_C} + \frac{\boldsymbol{r'}}{R_C}\right) - \frac{1}{Ro}\left(\hat{e}_{\boldsymbol{\omega}} \times \boldsymbol{u}^*\right) \tag{4.13}$$

where $\hat{e}_{\boldsymbol{R}_C}$ and $\hat{e}_{\boldsymbol{\omega}}$ are unity vectors. The terms within the second set of brackets derive from the decomposition of the centrifugal acceleration vector in the reference system (x',r'), as shown in figure 4.10. In particular, the first term in the bracket corresponds to the effect of an homogeneous acceleration $\omega^2 R_C$ in the $\boldsymbol{x'}$ direction. This acceleration increases proportionally to the distance $\boldsymbol{x'}$ according to the second term in the brackets. Finally the third term in the brackets represents an acceleration field in the radial direction $\boldsymbol{r'}$ of the computational domain, which is symmetrical with respect to the axis $\boldsymbol{x'}$. In the case of a large centrifuge arm and small sample, these acceleration gradients are not significant, however their effect might become important for small values of R_C, or in the case of large samples.

In order to evaluate the respective importance of Coriolis forces with respect to buoyancy, the quantities $1/Ro$ and Gr/Re^2 are compared. In particular, their ratio is equal to $Re^2/(GrRo) = u_{ref}/(\omega R_C \beta \Delta T_{ref})$. In general, the value of the reference velocity u_{ref} is unknown a priori, however further considerations can be derived by defining it as $u_{ref} = \sqrt{\omega^2 R_C \beta \Delta T_{ref} l_{ref}}$, after [19,43,44]. In this way, Reynolds number $Re = \sqrt{Gr}$, and equation 4.13 becomes:

$$\boldsymbol{B}^* = -\left(T^* - T_r^*\right)\left(\hat{e}_{\boldsymbol{R}_C} + \frac{\boldsymbol{x'}}{R_C} + \frac{\boldsymbol{r'}}{R_C}\right) - \sqrt{\frac{Ta}{Gr}}\left(\hat{e}_{\boldsymbol{\omega}} \times \boldsymbol{u}^*\right) \tag{4.14}$$

with the Taylor number $Ta = 4\omega^2 l_{ref}^4/\nu^2$ representing the ratio of Coriolis forces to viscous forces. Consequently, the ratio between Taylor number and Grashof number may be regarded as the ratio of Coriolis forces to the buoyancy forces induced by the overall gravitational field. It is to be noticed that this ratio does not depend on the value of the angular velocity ω, but is inversely proportional to the value of R_C. Therefore, the influence of Coriolis acceleration is expected to increase for smaller values of the centrifuge arm and vice versa.

On the other hand, it is expected that variations of the rotation speed would not induce critical variations in the effect of Coriolis forces with respect to buoyancy ones.

4.5.2 Results and discussion

In this section, the results from the simulations indicated in table 4.4 are reported and discussed. Firstly, the results from simulation S0 are considered. This case is analogous to the stable configuration discussed in section 4.4. However, since a different geometry is assumed, *i.e.*, 2D planar instead of axisymmetric, some changes in heat transfer and fluid flow are expected. Therefore, the scope of this simulation is to give a baseline solution in order to discern the effects of the different geometry from the actual influence of centrifugation. Temperature profile, front position and streamlines for this simulation are shown in figure 4.11. By comparing these results with the ones obtained for the axisymmetric geometry (see figure 4.8), it can be noticed that the front position in the sample at corresponding times is more advanced, demonstrating the presence of geometry related differences in the heat transfer process. Nonetheless, the qualitative conditions in the samples are analogous, hence initially only two counter rotating vortices develop, followed by the formation of two additional vortices due to the radial temperature gradient reversal at the right end of the sample. Quantitatively, the different temperature distribution in the sample induces a slightly increased convection than in the axisymmetric case, with maximum flow velocities of the order of 0.38 mm/s instead of 0.24 mm/s.

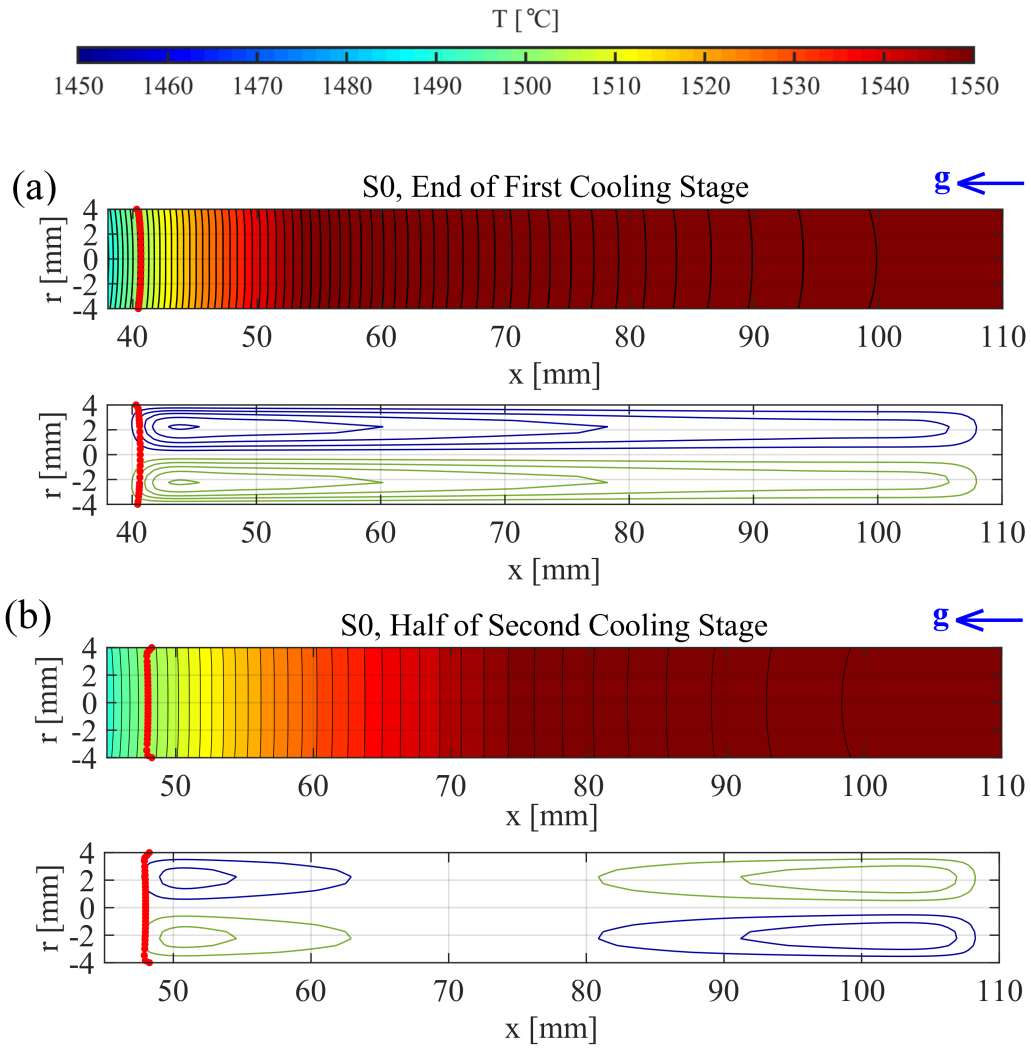

FIGURE 4.11: Columnar front position, temperature distribution, and streamlines in the sample at different times during the solidification process. Isotherms are drawn at intervals of 2°C, while streamlines are drawn at intervals of 0.15 mm^2/s.

Secondly, results from simulations S1, S2, S3, S4 are compared. For these simulations, different angular velocities are imposed, while the length of the centrifuge arm is kept constant and equal to 4 m (length of ESA's large diameter centrifuge arm). This investigation aims to show the influence on the fluid flow of different gravity levels (N_g=$\omega^2 R_C/g$). According to the non-dimensional analysis reported in the previous section, it is expected that an increase of the gravity level would induce the development of stronger buoyancy driven convection, since Grashof number is directly proportional to $\omega^2 R_C$. On the other hand, since the value of the centrifuge arm is much greater than the dimensions of the sample, the acceleration gradients in the domain are not significant with respect to the uniform acceleration component $\omega^2 R_C$. Also, according to the scaling shown in equation 4.14, the effect of Coriolis force with respect to buoyancy should not change significantly when only the angular velocity is changed.

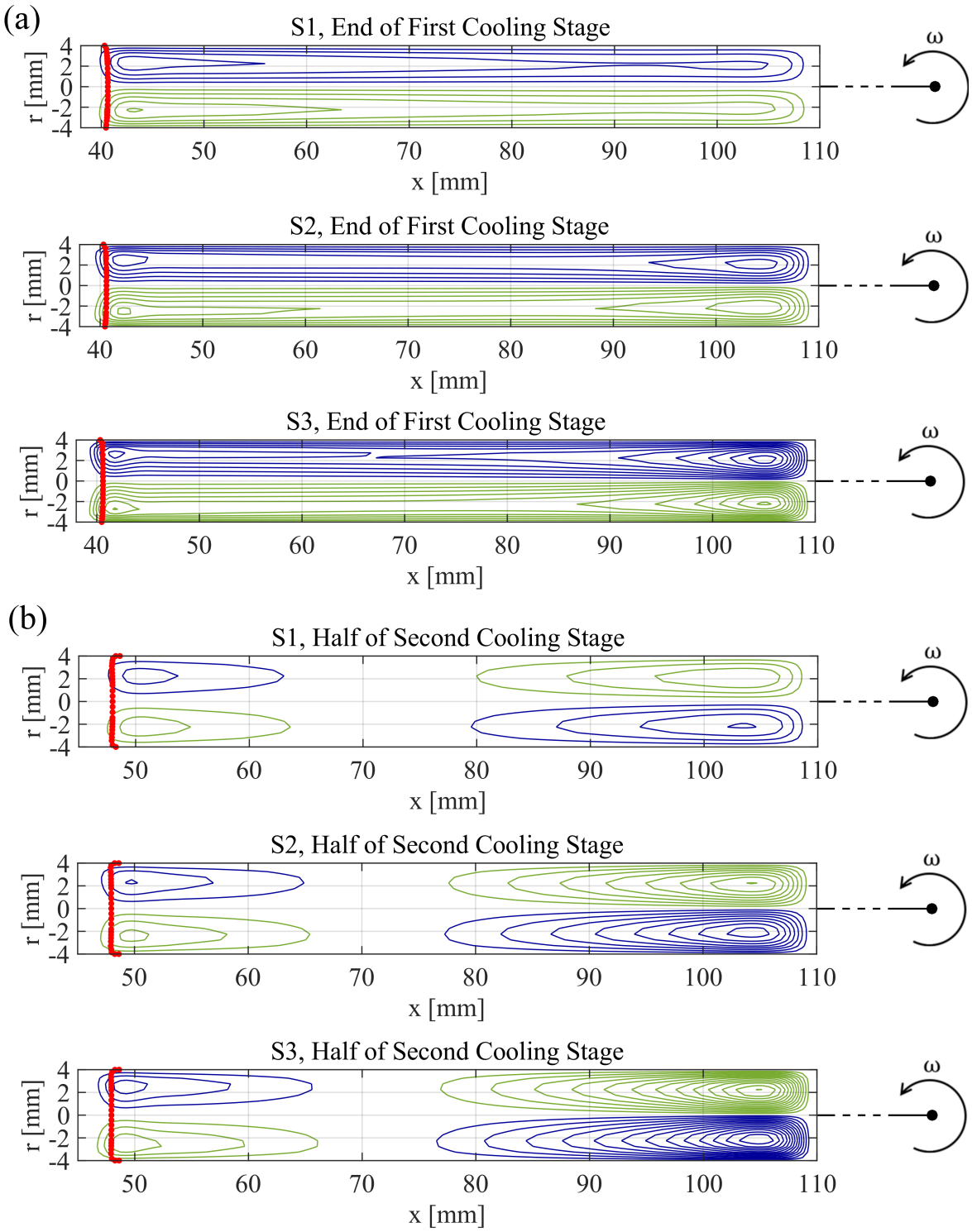

FIGURE 4.12: Effect of gravity level changes on the flow. Green streamlines correspond to counter-clockwise rotating flow, while blue stramlines correspond to clockwise rotating flow. Streamlines are drawn at intervals of 0.2 mm^2/s.

Figure 4.12 shows the streamlines obtained in the samples from simulations S1, S2, and

S3 (S4 is shown in figure 4.13). Noticeably, the fluid flow in all the samples is almost symmetrical with respect to the axial direction, which suggests a small impact of Coriolis force with respect to buoyancy induced convection. In order to quantify the ratio of Coriolis forces to buoyancy ones (CB_{ratio}), the quantity $Re^2/(GrRo)$ is calculated using the actual flow velocities and temperatures registered during the simulations. Results, reported in table 4.5, show that the effect of Coriolis force with respect to buoyancy due to the centrifugal force is negligible for the solidification process under consideration. Furthermore, it is possible to observe that the ratio of the two forces does not change significantly when ω is varied, as predicted from the non-dimensional investigation.

The qualitative nature of the flow is similar to the one obtained in the terrestrial gravity case (S0). As expected, an increase of the gravity level induces stronger convection. In particular, in the scaling analysis in section 4.5.1, the reference velocity of the flow is defined as directly proportional to $\sqrt{\omega^2 R_C}$. In fact, the actual rate of increase of velocity registered during the simulations is close to this proportion, as shown in table 4.5. Despite the relative stronger convection registered at higher values of the gravity level, the magnitude of velocity is still low ($Pe < 1$), hence heat transfer in the sample is driven by diffusion rather than convection. Also, the highest Reynolds number is obtained for simulation S8, with a mean value of 2.32 and a maximum of 32.14, confirming the laminar nature of the flow.

TABLE 4.5: Simulation results compared to predictions from the non-dimensional analysis.

	Simulation run							
	S1	S2	S3	S4	S5	S6	S7	S8
u_{mean} / [mm/s]	0.09	0.15	0.21	0.27	0.20	0.27	0.16	0.29
u_{mean}/u_{mean}^{S1}	1	1.67	2.33	3.00	2.22	3.00	1.78	3.2
$\sqrt{\omega^2 R_C}/\sqrt{\omega_{S1}^2 R_C^{S1}}$	1	1.6	2.3	3.2	1.6	3.2	1.6	3.2
$CB_{ratio} = Re^2/(GrRo)$	0.015	0.017	0.016	0.016	0.032	0.023	0.100	0.101
$CB_{ratio}/CB_{ratio}^{S1}$	1	1.13	1.07	1.07	2.13	1.53	6.67	6.73
$\sqrt{1/R_C}/\sqrt{1/R_C^{S1}}$	1	1	1	1	1.41	1.41	6.32	6.32

Finally, simulations S2, S5, S7, and S4, S6, S8 are considered, in order to investigate the influence of centrifuge arm variations, while keeping the quantity $\omega^2 R_C$ constant. Recalling

that the ratio of Coriolis forces to buoyancy ones can be evaluated by considering the ratio $\sqrt{Ta/Gr} \propto \sqrt{1/R_C}$, a stronger influence of Coriolis force with respect to buoyancy is expected for smaller radii of the centrifuge arm. Furthermore, even though $\omega^2 R_C$ is the same in all cases, for smaller values of R_C the acceleration components $\boldsymbol{x'}/R_C$ and $\boldsymbol{r'}/R_C$ become more significant, hence some influence on the fluid flow is expected.

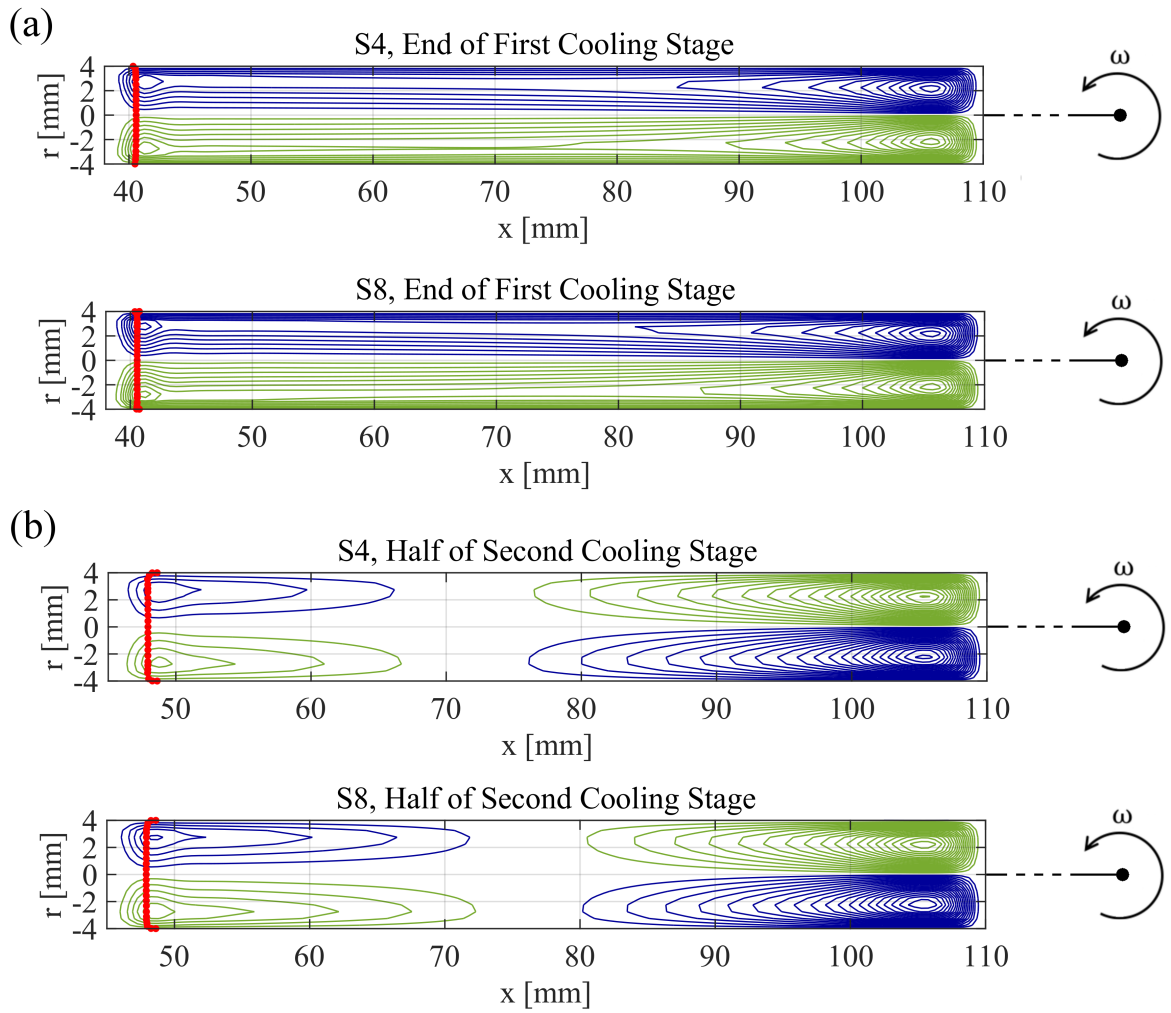

FIGURE 4.13: Effect of R_C changes on the flow. Green streamlines correspond to counter-clockwise rotating flow, while blue stramlines correspond to clockwise rotating flow. Streamlines are drawn at intervals of 0.2 mm^2/s.

Figure 4.13 shows the streamlines obtained in the samples from simulations S4 and S8. In particular, the fluid flow in S8 is very similar to the one in S4, still showing a substantial symmetry with respect to the axis of the domain. In fact, as reported in table 4.5, the ratio of Coriolis forces to buoyancy ones is still very low. Nonetheless, it is worth noting that, as predicted from the non-dimensional analysis in section 4.5.1, the relative magnitude of these two forces increases when the radius of the centrifuge is reduced, at a rate close to $1/\sqrt{R_C}$ (see table 4.5). Moreover, the effect of the acceleration gradient is observed. In particular

when the centrifuge arm is reduced to 0.1 m, due to the term $\boldsymbol{x'}/R_C$, the axial acceleration increases from the right to the left of the sample, reaching values of circa $1.7 \cdot \omega^2 R_C$ close to the front position. This induces a slight increase in the flow velocity, principally close to the front position. In addition, the effect of the radial acceleration $\boldsymbol{r'}/R_C$ cannot be neglected. Indeed, this component is stabilizing in the presence of negative radial temperature gradients and vice versa. This effect can be easily observed by comparing the two samples in figure 4.13(b). In fact, in S8, where the value of $\boldsymbol{r'}/R_C$ is much greater than in S4, the vortices on the left of the sample, where radial temperature gradients are positive, are stronger. On the contrary, convection is weaker on the left hand side of the sample where radial temperature gradients are negative.

In summary, results from this parametric study confirm the fact that increased levels of gravity induced by centrifugation lead to the development of stronger buoyancy convection in the samples. Moreover, the effects of Coriolis forces and of variations of the centrifugal acceleration field in the sample increase when the arm of the centrifuge is reduced. Remarkably, in all the examined cases, Coriolis forces are negligible with respect to buoyancy ones, hence the predicted flow patterns in the samples are mostly symmetrical with respect to the axial direction, *i.e.*, to the centrifuge arm direction. As in the terrestrial gravity scenario, the predicted convection is not sufficiently strong to modify significantly temperature evolution and columnar grain growth in the samples, but its influence on other phenomena (segregation etc...) should be further investigated.

4.6 Conclusions

In the present work, the following points were addressed, according to the objectives stated in section 4.1:

- an existing front tracking model for directional solidification of metal alloys [8] was significantly improved by the inclusion of a solver for Navier-Stokes equations, with the final goal to model buoyancy induced convection either in terrestrial gravity conditions or in hyper-gravity conditions arising during centrifugal casting;
- firstly, a case study corresponding to directional solidification carried out in microgravity conditions, and hence in absence of convection, was simulated. Results from this case study were used as a benchmark for comparison with solutions in the presence of convection;
- secondly, the novel numerical model was employed for the investigation of vertical solidification under terrestrial gravity conditions. In particular, two configurations were considered, *i.e.*, thermally stable configuration (top heated furnace) and thermally unstable configuration (bottom heated furnace). As main finding, this study showed that

in both cases convection was relatively weak (Pe <<1), hence temperature distribution and columnar front position were remarkably close to the ones calculated in the microgravity case. Therefore, for similar experimental scenarios, simpler models not including convection might be used for predicting temperature distribution and columnar front evolution. Nonetheless, since different flow patterns are predicted in the two cases, knowing the flow field appears necessary if other phenomena (*e.g.*, macrosegregation) were to be investigated;

- finally, the model was employed for the parametric investigation of directional solidification on a centrifuge. In particular, several case studies were analysed, where different values of the centrifuge rotation rate ω and centrifuge arm length R_C were considered. Simulation results showed that convection in the melt increased proportionally to the acceleration level. The rate of increase of convection was closely related to the quantity $\sqrt{\omega^2 R_C}$, in accordance to what was predicted from non-dimensional considerations. Also, in accordance to the non-dimensional analysis, the ratio of Coriolis forces to buoyancy ones increased proportionally to $\sqrt{1/R_C}$. Nonetheless, Coriolis forces did not influence significantly the fluid flow in any of the case studies, since their magnitude was negligible with respect to buoyancy induced by centrifugal acceleration. Therefore, fairly symmetrical flow patterns were predicted. In addition, as in the terrestrial gravity case, flow velocities were low and heat transfer in the sample was driven by diffusion rather than convection. Therefore, temperature distribution and columnar front position did not change significantly. Since the model employed for this investigation is 2D planar, the validity of the results with respect to real, fully 3D problems is not clear. Hence, further investigations, including comparison with experimental results and extension to 3D numerical models are planned for the future.

4.7 Addendum

4.7.1 Effect of sample misalignment during centrifugal casting

As stated in section 4.5, the setup assumed for simulations S1 to S8 (tables 4.1, 4.2, 4.3, and 4.4) aims to reproduce and investigate a series of experiments carried out on ESA's Large Diameter Centrifuge in the framework of the GRADECET project. Results from such experiments, part of the GRADECET LDC campaign II, are not yet accessible at the time of submission, therefore comparison is intended for future work. Nonetheless, qualitative results from previous experiments carried out during GRADECET LDC campaign I, are available and are the object of this section discussion. In this campaign a similar alloy to the one assumed for the simulations was used, *i.e.* Ti-46Al-8Nb. Due to the different alloy, the temperatures in the furnace were slightly lower than for the case study detailed in table 4.2, but the procedure to investigate the influence of gravity on the solidification process was the same. In fact, directional solidification experiments were performed by varying the centrifuge

rotation rate, reaching gravity levels of about 18 g. Besides the material, the main difference between campaign I and II experiments was the positioning of the sample with respect to the centrifuge arm, since in the first campaign these were not aligned, as shown in figure 4.15 and further discussed below.

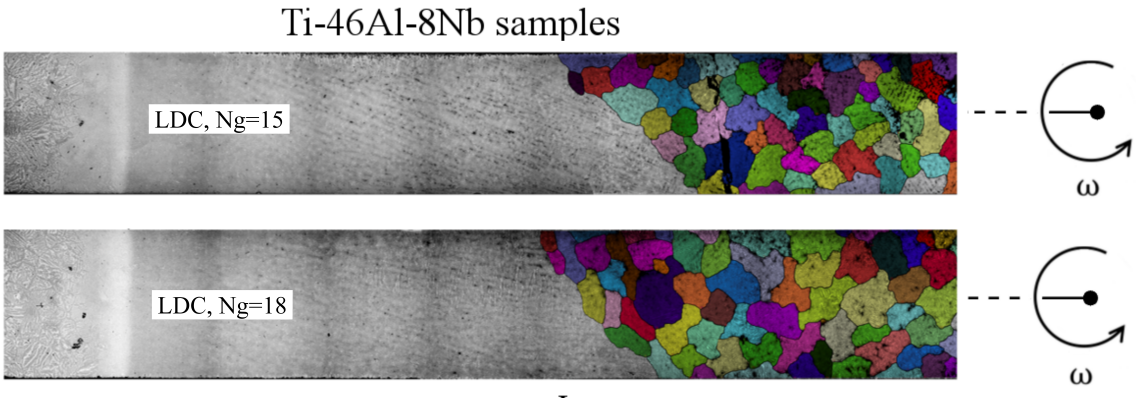

FIGURE 4.14: Horizontal sections of Ti-46Al-8Nb samples obtained by directional solidification on ESA's Large Diameter Centrifuge during GRADECET LDC campaign I.

Figure 4.14 shows horizontal sections of Ti-46Al-8Nb samples obtained during said directional solidification experiments on ESA's LDC. Interestingly, a remarkable lack of symmetry in the grain structure can be observed, *i.e.*, both columnar grains and CET show a negative inclination with respect to axis of the sample. This effect was initially ascribed to the presence of Coriolis force. Apparently, this outcome contrasts with the predictions of the simulations reported in section 4.5.2, where Coriolis force was not sufficiently strong to induce significant asymmetry in the fluid flow. To some extent, this qualitative discrepancy could be due to the intrinsic limitations of the front tracking model employed. Firstly, the model considers a 2D planar geometry, therefore it is impossible to capture any 3D effect due to the presence of terrestrial gravity acting in the vertical direction, and to the cylindrical shape of the sample. Secondly, solutal convection is not included in the model, which might induce further modifications in the fluid flow.

Nonetheless, by analysing the actual setup used during the experiments, a further explanation is proposed and tested with the numerical model. In particular, as figure 4.15 shows, the sample was located in the LDC gondola with a misalignment of approximately 115 mm with respect to the arm of the centrifuge.

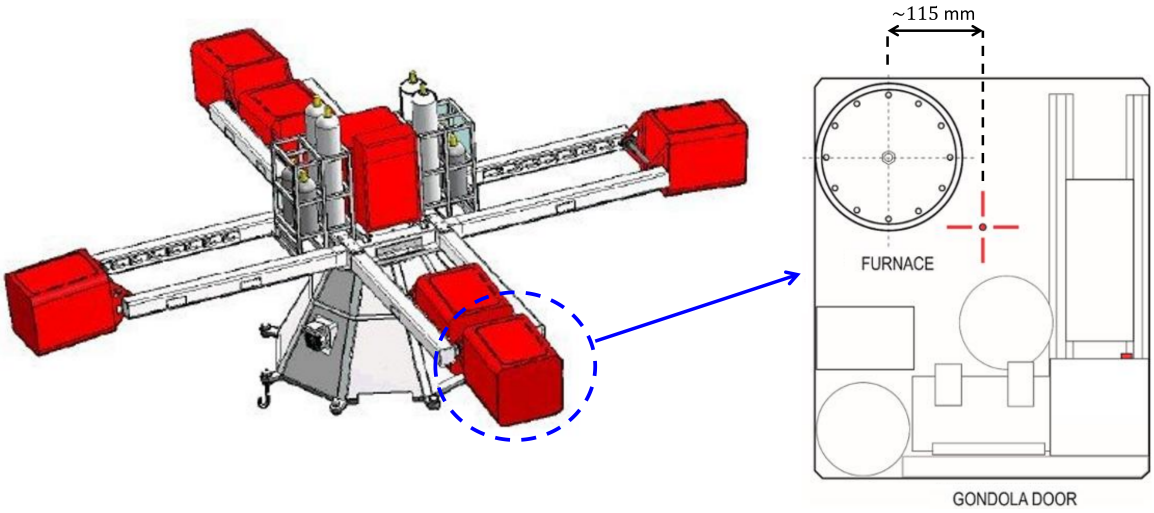

FIGURE 4.15: Experimental setup used during GRADECET LDC campaign I, showing the furnace misalignment with respect to the centrifuge arm.

As discussed in section 4.5, the centrifugal acceleration vector is not constant, and varies in the horizontal plane (x', r') according to the components $\omega^2 x'$ and $\omega^2 r'$ (see figure 4.10). It must be noted that the latter component induces an acceleration field which is symmetric with respect to the centrifuge arm. Therefore, even a slightly misaligned sample is subject to an asymmetric acceleration field, which might be sufficient to induce the development of tilted columnar grains and CET as the ones observed in figure 4.14. In order to test qualitatively this hypothesis, simulation S4 (table 4.4) is repeated by including the sample misplacement. Results are shown in figure 4.16.

In this case, it is evident that the fluid flow in the sample is not symmetric with respect to the x axis. As for the model prediction, the fluid flow asymmetry influences only marginally the temperature distribution and front position in the sample. The markers trajectories show a slight negative inclination, though not as marked as the one observed in figure 4.14. Also, when the likelihood of CET is investigated with Hunt's approach (section 3.5.1), the predicted transition is not as tilted as the one in the experiments. Nonetheless, it must be considered that the model does not capture several phenomena such as nuclei and equiaxed grains flotation or sedimentation, which combined to the asymmetric fluid flow might accentuate the angle of CET. Also, it can be observed that the earliest CET position in figure 4.14 is located on the top half of the samples sections, which corresponds to the region where the strongest convection is predicted by the simulations. It could be possible, for example, that the nuclei density in this area is higher due to dendrites fragmentation induced by the fluid flow.

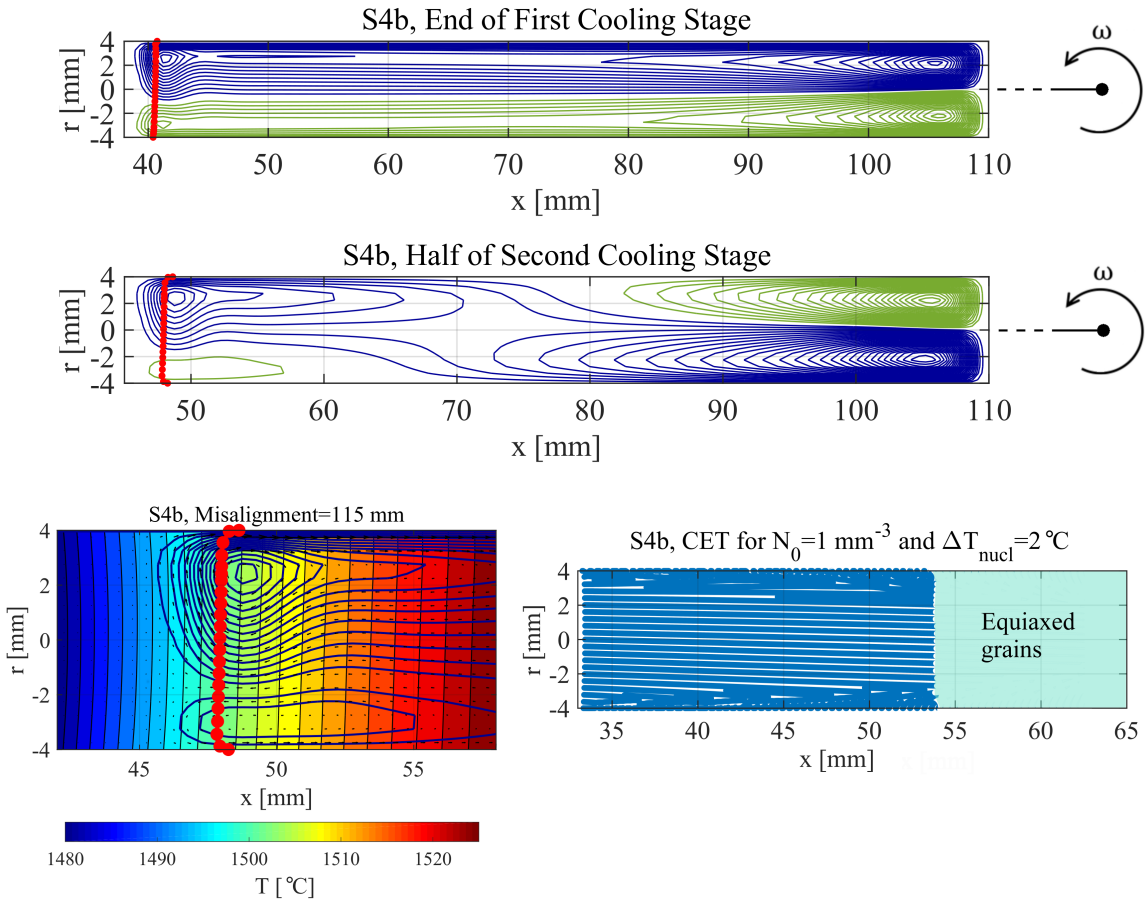

FIGURE 4.16: Simulation results for a sample positioned with 115 mm misalignment with respect to the centrifuge arm.

In conclusion, even though a proper correspondence is not found in terms of CET inclination, the numerical model does predict a significant asymmetry in the fluid flow, hence demonstrating that a correct positioning of the sample with respect to the centrifuge arm is crucial in order to at least reduce the development of asymmetric grain structures.

Acknowledgements

The author would like to thank Dr. Ulrike Hecht for providing data relative to MAXUS 9 and LDC experiments.

References

[1] L. Liu, T. Huang, M. Qu, G. Liu, J. Zhang, and H. Fu, "High thermal gradient directional solidification and its application in the processing of nickel-based superalloys," *J. Mater. Process. Technol.*, vol. 210, no. 1, pp. 159–165, 2010.

[2] A. J. Elliott, T. M. Pollock, S. Tin, W. T. King, S.-C. Huang, and M. F. X. Gigliotti, "Directional solidification of large superalloy castings with radiation and liquid-metal cooling: A comparative assessment," *Metall. Mater. Trans. A*, vol. 35, no. 10, pp. 3221–3231, 2004.

[3] H. Saari, J. Beddoes, D. Seo, and L. Zhao, "Development of directionally solidified γ-TiAl structures," *Intermetallics*, vol. 13, no. 9, pp. 937–943, 2005.

[4] C. A. Siqueira, N. Cheung, and A. Garcia, "Solidification thermal parameters affecting the columnar-to-equiaxed transition," *Metall. Mater. Trans. A*, vol. 33, no. 7, pp. 2107–2118, 2002.

[5] A. E. Ares, S. F. Gueijman, and C. E. Schvezov, "An experimental investigation of the columnar-to-equiaxed grain transition in aluminumcopper hypoeutectic and eutectic alloys," *J. Cryst. Growth*, vol. 312, no. 14, pp. 2154–2170, 2010.

[6] J. Lapin, Z. Gabalcová, U. Hecht, R. P. Mooney, and S. Mcfadden, "Columnar to Equiaxed Transition in Peritectic TiAl Based Alloy Studied by a Power-Down Technique,"

[7] R. P. Mooney, U. Hecht, Z. Gabalcová, J. Lapin, and S. McFadden, "Directional solidification of a TiAl alloy by combined Bridgman and power-down technique," *Kov. Mater. - Met. Mater.*, vol. 53, pp. 187–197, 2015.

[8] S. Battaglioli, A. Robinson, and S. McFadden, "Axisymmetric front tracking model for the investigation of grain structure evolution during directional solidification," *Int. J. Heat Mass Transf.*, vol. 115, pp. 592–605, 2017.

[9] P. Mazumder and R. Trivedi, "Integrated simulation of thermo-solutal convection and pattern formation in directional solidification," *Appl. Math. Model.*, vol. 28, no. 1, pp. 109–125, 2004.

[10] B. H. Zhou, H. Jung, N. Mangelinck-Noël, H. Nguyen-Thi, B. Billia, Q. S. Liu, and C. W. Lan, "Comparative study of the influence of natural convection on directional

solidification of Al-3.5 wt% Ni and Al-7 wt% Si alloys," *Adv. Sp. Res.*, vol. 41, no. 12, pp. 2112–2117, 2008.

[11] "On the interest of microgravity experimentation for studying convective effects during the directional solidification of metal alloys," *Comptes Rendus Mécanique*, vol. 345, no. 1, pp. 66–77, 2017.

[12] A. Kartavykh, V. Ginkin, S. Ganina, S. Rex, U. Hecht, B. Schmitz, and D. Voss, "Convection-induced peritectic macro-segregation proceeding at the directional solidification of Ti–46Al–8Nb intermetallic alloy," *Mater. Chem. Phys.*, vol. 126, no. 1, pp. 200–206, 2011.

[13] J. Spinelli, I. Ferreira, and A. Garcia, "Influence of melt convection on the columnar to equiaxed transition and microstructure of downward unsteady-state directionally solidified Sn–Pb alloys," *J. Alloys Compd.*, vol. 384, no. 1-2, pp. 217–226, 2004.

[14] J. N. Silva, D. J. Moutinho, A. L. Moreira, I. L. Ferreira, and O. L. Rocha, "The columnar to equiaxed transition during the horizontal directional solidification of Sn-Pb alloys," *J. Alloys Compd.*, vol. 478, no. 1-2, pp. 358–366, 2009.

[15] H. Rodot, L. Regel, G. Sarafanov, M. Hamidi, I. Videskii, and A. Turtchaninov, "Cristaux de rellurure de plomb élaborés en centrifugeuse," *J. Cryst. Growth*, vol. 79, no. 1-3, pp. 77–83, 1986.

[16] H. Rodot, L. L. Regel, and A. M. Turtchaninov, "Crystal growth of IV-VI semiconductors in a centrifuge," *J. Cryst. Growth*, vol. 104, no. 2, pp. 280–284, 1990.

[17] G. Müller, G. Neumann, and W. Weber, "The growth of homogeneous semiconductor crystals in a centrifuge by the stabilizing influence of the Coriolis force," *J. Cryst. Growth*, vol. 119, no. 1-2, pp. 8–23, 1992.

[18] W. Weber and U. Neumann, "Stabilizing influence of the coriolis force during melt growth on a centrifuge," *Journal of Crystal Growth*, vol. 100, no. 1, pp. 145 – 158, 1990.

[19] C. Lan, "Effects of centrifugal acceleration on the flows and segregation in vertical Bridgman crystal growth with steady ampoule rotation," *J. Cryst. Growth*, vol. 229, no. 1-4, pp. 595–600, 2001.

[20] W. Wilcox, L. Regel, and W. Arnold, "Convection and segregation during vertical Bridgman growth with centrifugation," *J. Cryst. Growth*, vol. 187, pp. 543–558, may 1998.

[21] D. Dimiduk, "Gamma titanium aluminide alloys—an assessment within the competition of aerospace structural materials," *Mater. Sci. Eng. A*, vol. 263, no. 2, pp. 281–288, 1999.

[22] K. Kothari, R. Radhakrishnan, and N. M. Wereley, "Advances in gamma titanium aluminides and their manufacturing techniques," *Prog. Aerosp. Sci.*, vol. 55, pp. 1–16, 2012.

[23] E. A. Loria, "Gamma titanium aluminides as prospective structural materials," *Intermetallics*, vol. 8, no. 9-11, pp. 1339–1345, 2000.

[24] E. A. Loria, "Quo vadis gamma titanium aluminide," *Intermetallics*, vol. 9, no. 12, pp. 997–1001, 2001.

[25] R. Mooney, S. Rex, L. Froyen, S. McFadden, O. Budenkova, D. Voss, B. Schmitz, Y. Fautrelle, A. Kartavykh, and D. Browne, "Review of the maxus 8 sounding rocket experiment to investigate solidification in a ti-al-nb alloy," *European Space Agency, (Special Publication) ESA SP*, vol. 700, pp. 453–458, 2011.

[26] D. J. Browne and J. D. Hunt, "A Fixed Grid Front-Tracking Model of the Growth of a Columnar Front and an Equiaxed Grain During Solidification of an Alloy," *Numer. Heat Transf. Part B Fundam.*, vol. 45, no. 5, pp. 395–419, 2004.

[27] S. McFadden and D. J. Browne, "A front-tracking model to predict solidification macrostructures and columnar to equiaxed transitions in alloy castings," *Appl. Math. Model.*, vol. 33, no. 3, pp. 1397–1416, 2009.

[28] J. Banaszek, S. McFadden, D. J. Browne, L. Sturz, and G. Zimmermann, "Natural Convection and Columnar-to-Equiaxed Transition Prediction in a Front-Tracking Model of Alloy Solidification," *Metall. Mater. Trans. A*, vol. 38, no. 7, pp. 1476–1484, 2007.

[29] W. U. Mirihanage, D. J. Browne, G. Zimmermann, and L. Sturz, "Simulation of international space station microgravity directional solidification experiments on columnar-to-equiaxed transition," *Acta Mater.*, vol. 60, no. 18, pp. 6362–6371, 2012.

[30] M. Seredyński and J. Banaszek, "Front Tracking Based Macroscopic Calculations of Columnar and Equiaxed Solidification of a Binary Alloy," *J. Heat Transfer*, vol. 132, no. 10, pp. 102301–1 – 102301–10, 2010.

[31] R. P. Mooney, S. McFadden, Z. Gabalcová, and J. Lapin, "An experimental-numerical method for estimating heat transfer in a Bridgman furnace," *Appl. Therm. Eng.*, vol. 67, no. 1-2, pp. 61–71, 2014.

[32] J. Banaszek and D. J. Browne, "Modelling Columnar Dendritic Growth into an Undercooled Metallic Melt in the Presence of Convection," *Mater. Trans.*, vol. 46, no. 6, pp. 1378–1387, 2005.

[33] M. Seredyński, P. Łapka, J. Banaszek, and P. Furmański, "Front tracking method in modeling transport phenomena accompanying liquid–solid phase transition in binary alloys and semitransparent media," *Int. J. Heat Mass Transf.*, vol. 90, pp. 790–799, 2015.

[34] W. Bennon and F. Incropera, "A continuum model for momentum, heat and species transport in binary solid-liquid phase change systems I. Model formulation," *Int. J. Heat Mass Transf.*, vol. 30, no. 10, pp. 2161–2170, 1987.

[35] J. Ni and F. P. Incropera, "Extension of the continuum model for transport phenomena occurring during metal alloy solidification-I. The conservation equations," *Int. J. Heat Mass Transf.*, vol. 38, no. 7, pp. 1271–1284, 1995.

[36] V. Voller, a.D. Brent, and C. Prakash, "The modelling of heat, mass and solute transport in solidification systems," *Int. J. Heat Mass Transf.*, vol. 32, no. 9, pp. 1719–1731, 1989.

[37] S. Patankar, *Numerical heat transfer and fluid flow.* 1980.

[38] H. Versteeg and W. Malalasekera, *An Introduction to Computational Fluid Dynamics - The Finite Volume Method.* 1995.

[39] W. Ames and C. Brezinski, *Numerical recipes in Fortran (The art of scientific computing).* 1993.

[40] F. Moukalled, L. Mangani, and M. Darwish, *The Finite Volume Method in Computational Fluid Dynamics.* 2016.

[41] M. Rebow, D. J. Browne, and Y. Fautrelle, "Combined Analytical and Numerical Front Tracking Approach to Modeling Directional Solidification of a TiAl-Based Intermetallic Alloy for Design of Microgravity Experiments," *Mater. Sci. Forum*, vol. 649, pp. 243–248, 2010.

[42] M. Seredynski and J. Banaszek, "Front tracking approach to modeling binary alloy solidification," *Int. J. Numer. Methods Heat Fluid Flow*, vol. 24, no. 4, pp. 920–931, 2014.

[43] W. a. Arnold, W. R. Wilcox, F. Carlson, A. Chait, and L. L. Regel, "Transport modes during crystal growth in a centrifuge," *J. Cryst. Growth*, vol. 119, pp. 24–40, apr 1992.

[44] N. Ramachandran, J. P. Downey, P. a. Curreri, and J. C. Jones, "Numerical modeling of crystal growth on a centrifuge for unstable natural convection configurations," vol. 126, pp. 655–674, 1993.

Chapter 5

Conclusions

The work presented in this thesis was completed as part of ESA's GRADECET project. This project was established in order to investigate gravity dependence of microstructure formation and CET in TiAl alloys. With this purpose in mind, various directional solidification experiments were performed in different environments, *i.e.*, on board MAXUS rockets, on Earth, and in ESA's Large Diameter Centrifuge. Alongside, numerical modelling activities were planned with a twofold scope; to help design the experiments, and to shed light on hard to observe phenomena.

In this context, the final aim of this thesis was to propose a methodology for the numerical investigation of directional solidification of TiAl alloys at the scale of the sample, and apply it to study the solidification process under different gravity conditions. According to what was stated in section 1.3, the main tasks to be addressed in order to achieve this goal were: to model directional solidification in absence of convection (*e.g.*, microgravity conditions) for investigating the effect of process parameters on temperature and grain structure evolution, and to model directional solidification in the presence of thermal convection for investigating the influence of different gravity conditions (terrestrial and hypergravity) on flow patterns and grain structure evolution. These tasks were fulfilled throughout the thesis by the development of three ever more advanced models, and by the simulation of several experimental scenarios and parametric studies. Presented here is a summary of the main findings of this thesis:

- in the case of Bridgman solidification of alloys (see chapter 2) the development of axial and radial temperature gradients in cylindrical samples is due to the interaction of several phenomena such as heat transfer at the boundaries, conduction and advection of sensible heat, and conduction and advection of latent heat (due to the translation of the mushy zone). In particular, it was illustrated how the ratios of dimensionless numbers Pe/Ste, Bi/Pe, and $Bi/(Pe/Ste)$ could give valuable information regarding the prediction of the final shape and position in the sample of the mushy zone. On one hand, this conclusion is deemed important for practitioners, since it gives an indication of the choice of process parameters in order to achieve the realization of desired conditions in the mushy zone, such as magnitude and sign of radial temperature gradients.

Moreover, when studying Bridgman solidification of alloys, the identified dimensionless groups could be used by modellers in order to assess the validity of particular simplifications, such as the assumption of 1D axial heat flow.

- In the case of Bridgman/power down directional solidification (see chapter 3) the development of different columnar grain regions, *i.e.*, axial or radial columnar, strictly depends on process parameters such as applied cooling rates. Specifically, it was demonstrated that the application of high cooling rates promotes the development of negative radial temperature gradients, which lead to the formation of unwanted radial columnar grain regions in the samples. Moreover, the extension of such regions becomes larger with the increase of the applied cooling rate. For this reason, the employment of low cooling rates (below 15°C/min for the specific case considered in chapter 3) is recommended in order to avoid radial columnar growth.

- The occurrence of columnar to equiaxed transition in the samples depends both on process parameters such as applied cooling rates and on characteristics of the alloy such as inoculation conditions. CET evaluation by means of the equiaxed index (see chapter 3) showed that the potential for equiaxed growth increases as cooling rates increase. However, the presence of radial growth reduces the opportunity for an equiaxed zone to develop at higher cooling rates. Further investigation, carried out with Hunt's model, showed that at higher cooling rates CET does not occur if the nuclei density is not sufficiently high. On the other hand, at low cooling rates CET does not occur if the undercooling required for equiaxed grains nucleation is too high. These observations are valuable when experiments for the observation of CET must be designed. In particular, in order to ensure a clear transition from axial columnar to equiaxed grains, avoiding at the same time the problem of radial growth, relatively low cooling rates with sufficient inoculation conditions are recommended (*e.g.*, $N_0 \geq 0.1$ mm^{-3} and $\Delta T_{nucl} \leq 2$°C for the case study considered in chapter 3).

- In the case of TiAl vertical solidification by power down under terrestrial gravity conditions (see chapter 4), it was shown that buoyant natural convection does not influence in a significant way the temperature field and columnar front evolution. From a modelling point of view, this is a valuable result, since it suggests that sufficiently accurate information on the evolution of temperature and columnar growth occurring during similar experiments could be obtained by using numerical models without the inclusion of convection, requiring much lower computational costs.

- In the case of directional solidification in a centrifuge (see chapter 4), a parametric study showed that the intensity of buoyant-driven convection in the samples increases with the increase of the gravity level. In addition, the effects of Coriolis forces and of variations of the centrifugal acceleration field increase when the arm of the centrifuge is reduced. Moreover, it was demonstrated how the variations of the centrifugal acceleration field promote the development of asymmetric flows and tilted grain structures

when the samples are mounted in a misaligned position with respect to the centrifuge arm. Therefore, as a first conclusion, it seems reasonable to suggest the employment of centrifuges with large arms (such as ESA's LDC) in order to reduce the possibility of asymmetric flows induced by Coriolis forces. Secondly, a careful positioning of the samples is recommended in order to avoid the development of skewed grain structures.

In conclusion, the conducted studies contribute to a better understanding of the solidification process in relation to process parameters and environment characteristics, while at the same time providing valuable recommendations for the potential design of further experiments. Moreover, the front tracking model presented in this thesis was proven to be a suitable tool for the investigation of the directional solidification process of alloys at the scale of the samples, being able to capture important phenomena while still retaining reasonable computational costs.

Finally, the main limitations of this thesis and consequent suggestions for future development are illustrated. First, none of the models presented here included a method for direct simulation of equiaxed grains nucleation and growth. While indirect methods such as equiaxed index and Hunt's analysis provided general indications on process parameters leading to CET, these are not able to capture several phenomena, such as latent heat release due to equiaxed grain growth, or grains buoyancy/sedimentation in the presence of convection etc. For this reason, the inclusion of a direct method for equiaxed nucleation and growth would be beneficial for future studies.

Second, in the front tracking model presented in chapter 4, solutal convection was not considered. This phenomenon, caused by the concentration gradients developing during solidification as a consequence of solute enrichment/depletion, is generally significant in the case of metal alloys. Along with thermal buoyancy, considering solutal convection is fundamental in order to investigate important aspects of the solidification process such as the formation of compositional heterogeneity (macrosegregation), which affect the quality of the cast. From a modelling point of view, including solutal convection in the case of multicomponent alloys implies the necessity to solve additional sets of transport equations for each solute, increasing the required computational effort. Nonetheless, such an improvement is deemed essential and highly encouraged in the future.

Last, the undeniable presence of three dimensional effects during the solidification process in the LDC centrifuge was discussed in chapter4, hence demonstrating the necessity to extend the front tracking model to 3D geometries.

Appendix A

FORTRAN Solver Description

This section reports a brief description of the main features of the FORTRAN code developed by the author for the solution of the numerical models presented. Here, the most general code relative to the model presented in chapter 4 is described. For reference, the general flowchart of the solution algorithm is reported here.

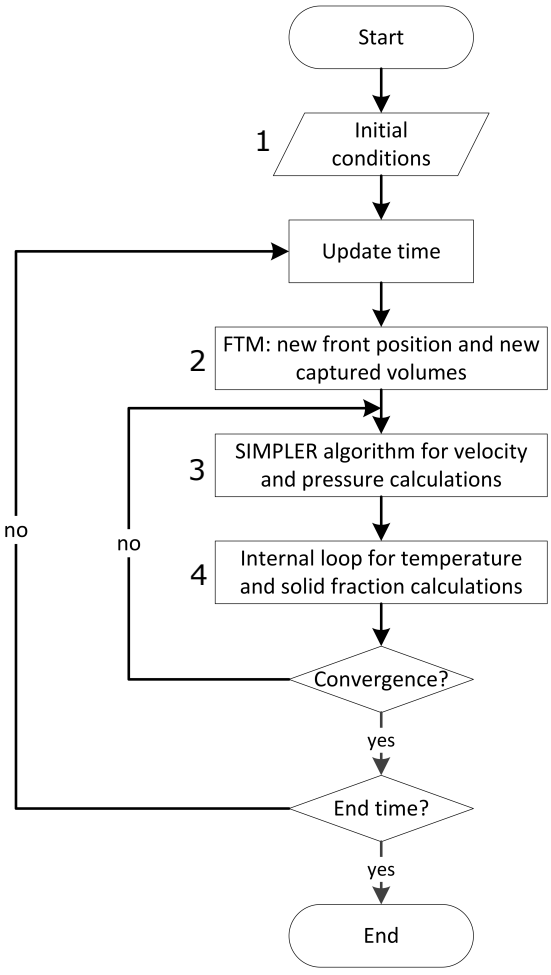

FIGURE A.1: Flowchart of general solution algorithm.

1. Initial conditions

After the declaration of the variables and the definition of several constants (*e.g.*, thermophysical properties and dimensions), the first initial condition to be assigned is the temperature field. This is followed by the creation of the initial front, which is positioned along an isotherm corresponding to a chosen level of undercooling (*e.g.*, 0.5°C). Inactive markers are also located along the liquid boundary of the sample to allow the simulation of radial columnar growth (see figure 3.3). The front is created using a doubly linked list, where each element of the list corresponds to a marker of the front. Specifically, each element contains important information for the evaluation of the front evolution, such as:

- a marker's flag, which allows to differentiate between active, inactive, and temporary markers;
- marker's coordinates;
- indices of the CV containing the marker;
- temperature at the marker's location, calculated by bilinear interpolation of the temperatures at the four closest CV centres;
- temperature gradient at the marker's location, useful for the evaluation of CET according to Hunt's method;
- vectors representing the direction of the marker's advance, corresponding to the normal to the front;
- components of the marker's velocity, calculated according to equation 3.5.

Defining the front as a doubly linked list is convenient for different reasons. For instance, it is possible to keep track of the order of the markers in the front without the need to define an actual index for each marker. This is essential since the front is designed in such a way that traversing it from the head marker to the tail the liquid phase is always on the right hand side, allowing to identify the correct direction of the front growth. Furthermore, the elimination/insertion of markers in case of accumulation/rarefaction is extremely easy.

Following the front creation, the captured volumes V_m of the CVs containing the front are evaluated. The subroutine developed for the calculation of the captured volumes allows to consider several configurations which might develop during the simulations as the front advances. Some examples are shown in figure A.2.

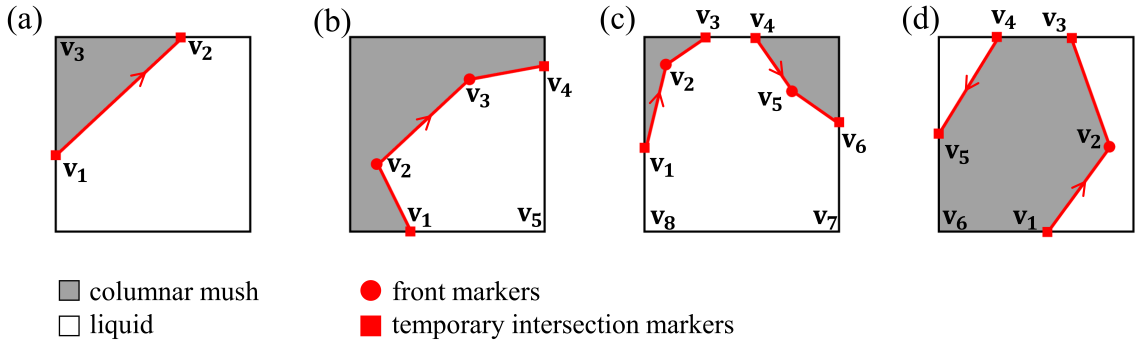

FIGURE A.2: Some examples of possible configurations of the captured volumes.

The vertices v_i of the polygons used for the calculation of the captured volumes may be front markers, corners of the CVs , or temporary markers that identify the intersections of the front with the grid lines. The areas of the polygons is calculated using Gauss's area formula:

$$A = \frac{1}{2}\sum_{i=1}^{n}(x_i r_{i+1} - x_{i+1} r_i) \tag{A.1}$$

considering n vertices of coordinates $(x_i; r_i)$ with $x_{n+1} = x_1$ and $r_{n+1} = r_1$. If the corners are numbered in a counter-clockwise order, such as in figure A.2(a)-(d), equation A.1 gives a positive result, hence the calculated area corresponds to the captured area of columnar mush in the CV. On the contrary, when the vertices are ordered in a clockwise way (*e.g.*, figure A.2(b)-(c)), the result of equation A.1 is negative and the captured area of mush is equal to $A_m = A_{CV} - |A|$. In the case of a 2D planar geometry, the captured volume corresponds to the captured area. In the case of a 2D axisymmetric geometry a further step is required. In particular, in this case the volume of the solid obtained by revolution of the polygon around the axis of the sample must be calculated. Considering an angle $d\theta$, the volume is given by Pappu's second theorem:

$$V = A \cdot d \cdot d\theta \tag{A.2}$$

where d is the distance between the axis of the sample and the geometric centroid of the polygon. Clearly, in cases such as the ones in figure A.2(b)-(c), the volume of mush will be equal to $V_m = V_{CV} - |V|$

Once the captured volumes are known, the initial solid fraction distribution can be evaluated. In particular, the value of mush solid fraction g_s in the CVs is obtained as a function

of temperature by interpolating tabulated values read from specific files. The overall solid fraction is then calculated based on the captured volume in the CV as $G_s = g_s \frac{V_m}{V_{CV}}$.

2. FTM: new front position and new captured volumes

At the beginning of each time step, the new position of the front and the new values of the captured volumes are calculated. As a first step, the temperature at each marker's position is evaluated. At this stage, if some of the inactive markers reach the undercooling required for nucleation, their flag is changed to the one corresponding to active markers.

Afterwards, the advance direction of each active marker is determined as the bisector of the angle between two segments formed by the previous, current and next marker. The correct direction of advance on the bisector line is easily determined, since it must lay on the right hand side of the front when proceeding from the previous to the next marker in the list.

The marker's velocity is then calculated as a function of the local undercooling and the new position of each marker is detemined with the procedure illustrated in figure 4.4.

Finally, the distances between successive markers of the new front are checked in order to avoid markers accumulation or rarefaction, which are prevented by deleting or adding markers to the list. Once the new front is identified, the new captured volumes are calculated according to the procedure explained above.

3. SIMPLER algorithm for velocity and pressure calculations

Pressure and velocity fields are calculated on a staggered grid using SIMPLER algorithm. Figure A.3 shows a flowchart of this algorithm. A detailed explanation on how to calculate pseudo-velocities and how to determine pressure correction equations may be found in the literature [1].

4. Internal loop for temperature and solid fraction calculations

After determining the new guess for the velocity field, the last step in the SIMPLER algorithm consists in the calculation of the remaining variables, *i.e.*, temperature and solid fraction. As explained in section 4.2.3, an iterative procedure is needed due to the non-linear dependence of g_s from T. The steps required at each iteration are illustrated in figure A.4.

At the end of this internal loop, the convergence of all the variables is verified, and, if reached, time is updated.

[1] H. Versteeg and W. Malalasekera, *An Introduction to Computational Fluid Dynamics - The Finite Volume Method.* 1995

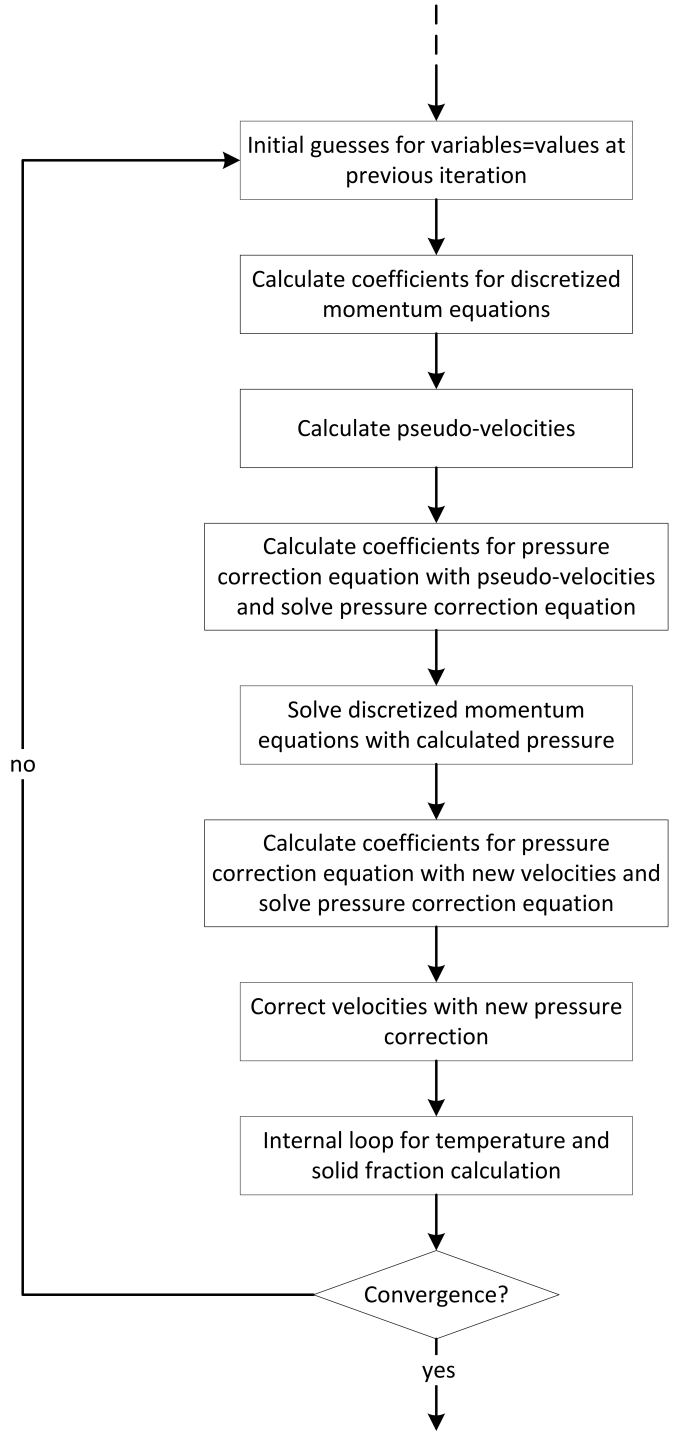

FIGURE A.3: Flowchart of SIMPLER algorithm for the calculation of pressure and velocity.

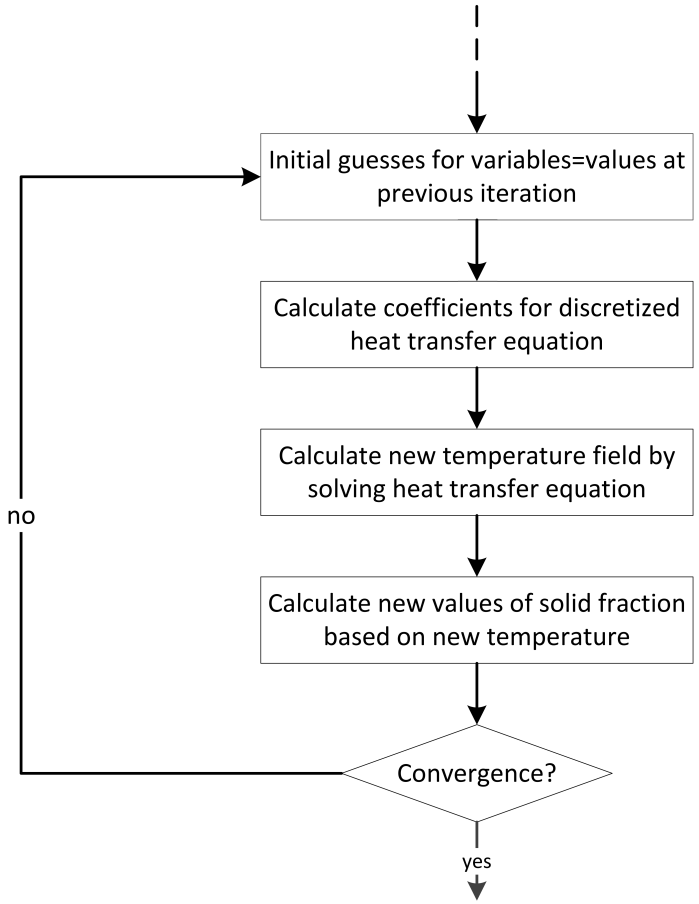

FIGURE A.4: Flowchart of internal loop for the calculation of temperature and solid fraction.